



Durham E-Theses

Classical and quantum chaos of dynamical systems: rotating billiards

Siegwart, David Kevin

How to cite:

Siegwart, David Kevin (1990) *Classical and quantum chaos of dynamical systems: rotating billiards*, Durham theses, Durham University. Available at Durham E-Theses Online: <http://etheses.dur.ac.uk/6228/>

Use policy

The full-text may be used and/or reproduced, and given to third parties in any format or medium, without prior permission or charge, for personal research or study, educational, or not-for-profit purposes provided that:

- a full bibliographic reference is made to the original source
- a link is made to the metadata record in Durham E-Theses
- the full-text is not changed in any way

The full-text must not be sold in any format or medium without the formal permission of the copyright holders.

Please consult the [full Durham E-Theses policy](#) for further details.

Classical and Quantum Chaos
of Dynamical Systems:
Rotating Billiards

by

DAVID KEVIN SIEGWART

A thesis presented for the degree of Doctor of
Philosophy at the University of Durham.

*University of Durham
Department of Mathematical Sciences
Durham DH1 3LE
England*

January 1990

The copyright of this thesis rests with the author.
No quotation from it should be published without
his prior written consent and information derived
from it should be acknowledged.



25 JUN 1991

"The next great era of awakening of human intellect may well produce a method of understanding the qualitative content of equations. Today we cannot. Today we cannot see that the water flow equations contain such things as the barbar pole structure of turbulence that one sees between rotating cylinders. Today we cannot see whether Schrödinger's equation contains frogs, musical composers, or morality—or whether it does not. We cannot say whether something beyond it like God is needed or not. And so we can all hold strong opinions either way."

Richard P. Feynman,

in *The Feynman Lectures in Physics Volume II*,

Chapter 41, Addison-Wesley (1964).

ABSTRACT

The theory of classical chaos is reviewed. From the definition of integrable systems using the Hamilton-Jacobi equation, the theory of perturbed systems is developed and the Kolmogorov-Arnold-Moser (KAM) theorem is explained. It is shown how chaotic motion in Hamiltonian systems is governed by the intricate connections of stable and unstable invariant manifolds, and how it can be categorised by algorithmic complexity and symbolic dynamics, giving chaotic measures such as Lyapunov exponents and Kolmogorov entropy. Also reviewed is Gutzwiller's semiclassical trace formula for strongly chaotic systems, torus quantisation for integrable systems, the asymptotic level density for stationary billiards, and random matrix theories for describing spectral fluctuation properties.

The classical theory is applied to rotating billiards, particularly the free motion of a particle in a circular billiard rotating uniformly in its own plane about a point on its edge. Numerically, it is shown that the system's classical behaviour ranges from fully chaotic at intermediate energies, to completely integrable at very low and very high energies. It is shown that the strong chaos is due to discontinuities in the Poincaré map, caused by trajectories which just glance the boundary—an effect of the curvature of trajectories. Weaker chaos exists due to the usual folding and stretching of the Hamiltonian flow. Approximate invariant curves for integrable motion are found, valid far from the presence of glancing trajectories. The major structures of phase space are investigated: a fixed point and its bifurcation into a two-cycle, and their stabilities. Lyapunov exponents for trajectories are calculated and the chaotic volume for a wide range of energies is measured.

Quantum mechanically, the energy spectrum of the system is found numerically. It is shown that at the energies where the classical system is completely integrable the levels do not repel, and at those energies where it is completely chaotic there is strong level repulsion. The nearest neighbour level spacing distributions for various ranges of energy and values of Planck's constant are found. In the semiclassical limit, it is shown that, for energies where the classical system is completely chaotic, the level spacing statistics are Wigner, and where

it is completely integrable, the level spacing statistics are Poisson. A model is described for the spacing distributions where the levels can be either Wigner or Poisson, which is useful for showing the transition from one to the other, and adequately describes the statistics. Theoretically, the asymptotic level density for rotating billiards is calculated, and this is compared with the numerical results with good agreement, after modification of the method to include all levels.

CONTENTS

List of Figures and Tables	vii
-----------------------------------	-----

Chapter 1: Introduction	1
--------------------------------	---

Chapter 2: Classical and Semiclassical Mechanics in Bound Systems

2.1 <i>Introduction</i>	7
2.2 <i>Integrable Systems</i>	8
2.3 <i>The KAM Theorem</i>	12
2.4 <i>Poincaré Surfaces of Section</i>	14
2.5 <i>Strongly Chaotic Motion</i>	18
2.6 <i>Stationary Billiards</i>	21
2.7 <i>Semiclassical Mechanics for Chaotic Systems</i>	23
2.8 <i>Torus Quantisation in Integrable Systems</i>	31
2.9 <i>The Asymptotic Level Density for Stationary Billiards</i>	34
2.10 <i>Spectral Fluctuation Properties</i>	38

Chapter 3: Classical Billiards in Rotating Boundaries

3.1 <i>Introduction</i>	49
3.2 <i>The Rotating Circular Billiard</i>	51
3.3 <i>Periodic Cycles of the Rotating Circle</i>	56
3.4 <i>Approximate Solutions for Adiabatic Skipping</i>	60
3.5 <i>The Poincaré Map</i>	72
3.6 <i>Influence of the Curvature of Trajectories</i>	81
3.7 <i>Lyapunov Exponents and Chaotic Volume</i>	95

Chapter 4: Quantum Billiards in Rotating Boundaries

4.1 General Rotating Billiards	100
4.2 Energy Levels of the Rotating Circular Billiard	106
4.3 Energy Level Spacing Statistics	109
4.4 Spacing Distributions of Mixed Systems	116
4.5 The Asymptotic Level Density for Rotating Billiards	119
Chapter 5: Discussion	125
Appendix A: The Tangent Map for the Rotating Circle	131
References	133

LIST OF FIGURES AND TABLES

<i>Figure 2.2.1.</i> An invariant torus of an integrable system	10
<i>Figure 2.2.2.</i> The elliptical billiard	11
<i>Figure 2.4.1.</i> Poincaré surface of section	15
<i>Figure 2.4.2.</i> The Poincaré-Birkhoff Theorem	16
<i>Figure 2.4.3.</i> Homoclinic connections	17
<i>Figure 2.6.1.</i> The circular billiard	22
<i>Figure 2.7.1.</i> A typical set of paths passing through a conjugate point	26
<i>Figure 2.8.1.</i> Quantum numbers in action space	33
<i>Figure 2.9.1.</i> Image of a point in the tangent plane to a surface	37
<i>Figure 2.10.1.</i> Diagram used when calculating $P(S)$	42
<i>Figure 3.1.1.</i> The energy surface $E = \text{const.}$ for a rotating billiard	52
<i>Figure 3.2.1.</i> The circular rotating billiard	53
<i>Figure 3.2.2.</i> Specular reflection in the circular rotating billiard	55
<i>Figure 3.3.1.</i> The fixed point of the circular rotating billiard	56
<i>Figure 3.3.2.</i> A two-cycle of the circular rotating billiard	58
<i>Figure 3.3.3.</i> Angle of projection for the fixed point and the two-cycle	61
versus the energy for the rotating circle.	
<i>Figure 3.4.1.</i> Approximate and exact invariant curves	64-71
for the rotating circle.	
<i>Figure 3.5.1.</i> Poincaré maps for 100 trajectories	73-76
initially on a 10 by 10 grid.	
<i>Figure 3.5.2.</i> Poincaré maps for one trajectory	77-78
for the rotating circle.	
<i>Figure 3.5.3.</i> Enlargement of one point of a three-cycle for a succession	79
of energies for the rotating circle.	

<i>Figure 3.5.4.</i> Joined Poincaré map for the rotating circle	80
<i>Figure 3.6.1.</i> Four types of trajectory possible for rotating billiards	81
<i>Figure 3.6.2.</i> Trajectory showing tangent and normal vectors	82
<i>Figure 3.6.3.</i> A set of trajectories in the rotating circle	83
<i>Figure 3.6.4.</i> First iteration of the Poincaré map for figure (3.6.3)	83
<i>Figure 3.6.5.</i> Pre-image of glancing trajectories for the rotating circle	85
<i>Figure 3.6.6.</i> Poincaré maps after one and two iterations	86-89 for the rotating circle.
<i>Figure 3.6.7.</i> Poincaré maps for one trajectory	91-93 for the rotating circle.
<i>Figure 3.6.8.</i> Sliding motion in the billiard plane and the Poincaré section for the rotating circle	94
<i>Figure 3.7.1.</i> Chaotic volume versus the energy for the rotating circle	98
<i>Figure 4.1.1.</i> The rotating sector billiard	104
<i>Figure 4.2.1.</i> The unfolded energy spectrum for the rotating circle	108
<i>Figure 4.3.1.</i> Level spacing distributions and cumulative	113-115 distributions for the rotating circle.
<i>Figure 4.4.1.</i> The fitting parameter μ of the cumulative distribution	118 for the rotating circle.
<i>Figure 4.5.1.</i> The classically allowed region of the rotating circle	122
<i>Figure 4.5.2.</i> The spectral staircase for the rotating circle at $\alpha = 6$	123
<i>Table 4.3.1.</i> The first, 50 th , 100 th and 150 th energy levels	111 of the rotating circle.
<i>Table 4.3.2.</i> The W^2 statistic for the level spacing distributions	112 for the rotating circle.

PREFACE

The work in this thesis was carried out between October 1986 and December 1989 in the Department of Mathematical Sciences at the University of Durham, under the supervision of Dr. D.B. Fairlie.

None of this work has previously been submitted for any degree in this or any other university. I claim no originality for chapter 2. The work of chapters 3 and 4 is published in [1,2] and was motivated and inspired by Michael V. Berry's Bakerian Lecture of 1987. Most of the work in chapter 3 was done in collaboration with David Fairlie, except for the calculation of the radius of curvature of trajectories due to H. Frisk and R. Arvieu, and section 3.7 which is my own work. The work of chapter 4 is solely my own, but credit for the spacing distribution model for mixed systems must go to M.V. Berry and M. Robnik. Other work by the author was carried out in the same period as this thesis, but is in a different field of study, and is not published here. The first, in collaboration with Euan J. Squires, was an investigation of a report that CP violation allows faster than light signals, violating causality [3]. The second is a toolkit giving generating functionals for the calculation of anomaly coefficients for SU(n) in collaboration with Harry W. Braden [4].

I would like to express my gratitude to David Fairlie for his helpful encouragement and guidance throughout the course of this work, and for the freedom he has given me to explore a field that is new to both of us. I would also like to thank Bob C. Johnson for many useful discussions on quantum chaos, and also Euan Squires, Ed F. Corrigan, Richard S. Ward, and Graeme D. Robertson. I thank Alan H. Seheult and Peter J. Green for discussions on the statistical analysis of eigenvalues. Support from the Science and Engineering Research Council is kindly acknowledged and thanked.

Copyright ©1990 by David K. Siegwart

The copyright of this thesis rests with the author. No quotation from it should be published without his prior written consent and information derived from it should be acknowledged.

1. Introduction

One of the great challenges of modern physics is to unite the two fundamentally different theories of classical mechanics and quantum mechanics in all their manifestations via the correspondence principle. It is interesting that such a wide body of physics is based on, and can be approximated by, classical mechanics when the underlying laws are not classical but quantum mechanical. What is even more remarkable is that quantum mechanics is conceptually, philosophically and mathematically unlike classical mechanics. It is because classical mechanics is such a good theory that we expect a correspondence principle: quantum mechanics must agree with classical mechanics when Planck's constant $\hbar = 2\pi\hbar$ is negligible compared to other physical parameters of the system.

At first sight, it may seem quite clear that, by adjusting the system's parameters and dimensions, we can reduce \hbar to negligible size and hence reproduce the classical behaviour. However, there now appear to be circumstances when this cannot be done. Suppose the classical system has infinitely fine structure in the Hamiltonian flow in phase space. This can never be modelled completely by quantum mechanics, because volume elements smaller than the size of \hbar^N (for an N freedoms system) are not meaningful. (The difference is due to that between the classical description in terms of ordinary differential equations, and the quantum description in terms of partial differential equations—the latter's smoothness never quite able to match the singularities of the former.) This may not matter if such small scale structure is not amplified, because the quantum differences would never become macroscopic. However, for classically chaotic systems such effects would be amplified, because classical chaos involves the folding of the Hamiltonian flow to and from small scale structures to large scale structures in an infinite hierarchy. In such cases there would always be aspects of classical phenomena which cannot be reproduced by a quantum system.

One such example is the infinite time behaviour of trajectories, which is important in determining whether a trajectory is chaotic. An infinite time is needed because over finite times a trajectory may appear chaotic, but the apparent sensitivity on initial conditions may be transient, and the orbit seen to

be regular over a longer interval. Quantum mechanically, a chaotic trajectory will eventually encounter regions where an error within a volume of phase space less than the size of \hbar^N would drastically affect its path. Then the description of the motion in terms of classical trajectories becomes meaningless, and this lack of classical meaning would be transported to all scales. This introduces a finite time scale at which quantum mechanics suppresses classical chaos, the best known example of this being the quantum kicked rotator [5] where the time scale is the break time beyond which diffusion due to classically chaotic motion is no longer mimicked by quantum mechanics.

Thus we envisage a regime where \hbar is sufficiently small that a classical description would seem naïvely reasonable, but quantum effects are significant at a macroscopic scale, due to the fact that quantum mechanics does not display chaos, but merely models the classically chaotic motion up to a certain finite scale, determined by the size of \hbar .

We then have the problem of interpreting phenomena which can be described by classical mechanics for much of the time, but are essentially quantum mechanical for the rest of the time. Does this mean that we should give up the description in terms of trajectories, or do we have the situation where trajectories interfere quantum mechanically and become mixed, such that we may still regard the motion as classical over short intervals, but over long intervals these classical segments must be spliced together, in regions where the notion of trajectories does not make sense, and purely quantum mechanical rules must be used? Is any of the motion classical, because until the wavefunction has collapsed none of the classical segments is chosen to be the true path?

These are some of the aims and aspirations of researchers in the study of quantum chaos, but we only touch some of these objectives in this thesis, as we seek to study specific systems, and address the problem in greater detail.

There are two requirements for chaos. Firstly, the system must be bound, so that phase space is finite, and orbits return. And then there must be stretching and folding of the Hamiltonian flow. Billiards in general satisfy both of these requirements, as well as offering the benefits of mathematical simplicity, making

them relatively easy to study numerically in detail, and to quantise. They are also generic:

“Any dynamical system with two degrees of freedom is isomorphic with the motion of a particle on a smooth surface rotating uniformly about a fixed axis and carrying a conservative field of force with it.” [6]

Because of the complexity of classical chaos, and the difficulty of quantising complex systems, we need as simple a model as possible without losing any of the interesting chaotic behaviour.

Historically, the study of chaos began with Poincaré’s study of the three body problem in celestial mechanics [7]. He showed that this problem is not solvable; the perturbation expansion does not converge near commensurable tori, due to the problem of small denominators, and Poincaré proved that an intricate web of invariant manifolds with structure on all scales made the analysis incomputable.

It was more than half a century later that Arnol’d and Moser in 1962 [8,9] discovered the celebrated KAM theorem, based on suggestions by Kolmogorov in 1954. The theorem proved that, under small perturbations of an integrable system, ‘most’ tori are preserved.

In the meantime, ergodic properties of chaotic systems were rigorously proved by Sinai [10], Arnol’d and Avez [11], and Pesin [12], based on Shannon’s information theory [13] as applied by Kolmogorov [14] to dynamical systems. The theory represents trajectories as infinite sequences of symbols, with chaotic sequences being indistinguishable from random sequences (so-called Bernoulli sequences). This led to the invention of various measures of chaos: Lyapunov exponents, Kolmogorov entropy, and chaotic volume (fraction of phase space which is chaotic). Many examples were proved to be chaotic: Sinai’s billiard [15], the stadium of Bunimovich [16], and more recently, a whole class of billiards with convex pieces of boundary [17].

Periodic orbits were seen by Birkhoff [6] to be of utmost importance. Although of zero measure, their influence extends across most of the phase space. In chaotic systems, there is a large proliferation of periodic orbits, growing exponentially with the orbits’ length. Bifurcations of periodic orbits are useful ways

of determining structural stability of systems, and period doubling cascades in one-dimensional systems are helpful in understanding the route to chaos.

In quantum mechanics, periodic orbits of classical strongly chaotic systems have been shown to be related to the eigenvalues of the quantum system by a semiclassical trace formula or sum rule. This has been greatly studied by mathematicians for geodesics on Riemannian surfaces of negative curvature (see review by Balazs and Voros [18]) giving the Selberg trace formula. For physical systems, Gutzwiller has discovered an equivalent trace formula from the viewpoint of the Feynman path integral formalism [19,20].

Percival [21] has emphasised that eigenstates of chaotic systems should behave ‘irregularly’, whilst those of integrable systems should be somehow regular. This has resulted in many studies of level statistics and morphology of wavefunctions. McDonald and Kaufman [22] have claimed that eigenfunctions for the stadium of Bunimovich have peaks and troughs randomly distributed, but more recently, with greater computing power, Heller [23] has shown that this is a simplification, and quantum scars of high probability density, due to unstable isolated periodic orbits, have been detected. Of the work on level statistics, Berry, Bohigas and Giannoni amongst others [24,25] have related this study to level statistics of atomic nuclei—complex systems of many freedoms—and random matrix theories [26] showing that generic integrable systems have Poisson statistics for level spacing, with level clustering, whilst chaotic systems have Wigner statistics, with level repulsion. A curious result of this is that levels of integrable systems are, in a sense, *more* random than those of chaotic systems, because the integrable levels are less evenly spaced. However, this is deceptive because integrable systems always have good quantum numbers to label eigenfunctions, chaotic systems do not, and this is likely to mean that physical properties are less predictable.

Various systems displaying these properties have been studied numerically: heart-shaped billiards [27] , elliptic billiards in magnetic fields [28] , Aharonov-Bohm Africa billiards [29] , neutrino billiards [30] and particles in polynomial nonlinear potentials. Some of the interesting variations above show quadratic level repulsion due to the time-irreversibility of the system. All the above systems

have been chosen to be strongly chaotic.

Seligman *et al* [31] have calculated level statistics for the generic case of a system which is classically mixed (*i.e.* part of phase space is regular, part is chaotic). For this system they show that level statistics show a transition from Poisson to Wigner distributions. Matsushita and Terasaka [32], and Scott [33] have also calculated level statistics for mixed systems.

The contents of this thesis are split into four parts. In chapter 2, I will review the underlying theory of classical chaos and semiclassical mechanics of nonintegrable systems. In chapter 3, I will discuss the classical motion of rotating billiards. These are systems which, although the boundary of the billiard may be perfectly smooth, display chaos due purely to the rotation of the billiard, giving curved paths in the frame rotating with the billiard. They are thus very interesting to study. Firstly, they are more generic than stationary billiards (recall Birkhoff's statement at the beginning of this chapter), but have all the useful attributes of stationary billiards (mathematical simplicity, ease of quantisation, simplified models in nuclear physics), as well as the possibility of new effects: time-reversal breaking, transition from integrability to chaos as speed of rotation is increased. To be discussed are the periodic orbits, their bifurcations and stability, the invariant tori—approximate adiabatic skipping curves, Lyapunov exponents and chaotic volume, and other structures in phase space.

In chapter 4, I will discuss the quantum mechanics of rotating billiards. By expressing the wavefunction in terms of the exact basis of unperturbed eigenfunctions, the sequence of lowest energy levels will be found using the Rayleigh-Ritz variational method, from which one can determine upper bounds on the levels. Matrices shall be diagonalised for various values of \hbar , and the level repulsion and level clustering compared with predictions from the classical mechanics and the chaotic volume. Level spacing statistics shall be calculated in more detail, and modelled using a distribution between Wigner and Poisson. The asymptotic level density shall be calculated theoretically and compared with the numerically determined spectral staircase.

In chapter 5, I will discuss the results of chapters 3 and 4, and mention further work that could be done on this system, such as quantising \hbar instead of

the energy (this just alters the curve in $E\hbar$ -space along which eigenvalues are found—keeping the energy constant is a much better method), and studying wavefunctions, as well as indicating the possible avenues to explore in a more general context. I will also relate this work to further work by others and mention their results and aspirations. A short conclusion shall summarise what I have learnt by studying this system.

2. Some Aspects of Classical and Semiclassical Mechanics of Bound Systems

2.1 *Introduction*

In this chapter I shall introduce and develop the classical theory of chaotic motion, based on several reviews and articles, and the semiclassical theory of non-integrable systems. The concepts covered will be used in subsequent chapters, and form the basis of the thesis. In the first half, I shall concentrate on the classical mechanics, introducing integrable systems through the Hamilton-Jacobi equations, then showing how perturbations of these systems give rise to the problem of small denominators, causing divergent series. I shall show how this deep problem was partially explained by the KAM theorem and its developments, how this leads to the realisation that unstable periodic orbits are important in regions where KAM does not apply, and how this gives some theoretical justification for the large computational evidence in favour of chaotic motion. I will also introduce Lyapunov exponents, chaotic volume and Kolmogorov entropy. I will end discussing some properties of stationary billiards.

In the second half, which is concerned with the relationship between quantum mechanics and classical chaos, I shall review semiclassical mechanics and derive the Gutzwiller trace formula, which relates energy eigenvalues to periodic orbits. I will use torus quantisation to find an equivalent formula for integrable systems. The asymptotic mean level density, which gives the smooth behaviour of the spectral staircase, is introduced and derived for stationary billiards. Statistical properties of the spectrum, such as the level spacing distribution and spectral rigidity, are reviewed in the last section.

2.2 Integrable Systems

I shall review here the meaning and definition of an integrable system using Goldstein [34] and Landau and Lifshitz [35] as main references.

Suppose we have a conservative system of N freedoms, with the action integral

$$R(q'q''t't'') = \int_{t'}^{t''} L dt. \quad (2.1)$$

where L is the Lagrangian $L(q_1, \dots, q_N, p_1, \dots, p_N, t)$ and the integral is along a path between the two positions $\mathbf{q}(t')$ and $\mathbf{q}(t'')$ (I shall in future drop the bold vector notation, and write just $q(t')$ or q' etc.). Now we consider a variational principle, making stationary the functional R with respect to varying the paths between $q(t')$ and $q(t'')$. So R is now a function called Hamiltonian principal function. We wish to consider how R varies as we vary an end point of the path. Suppose $q(t')$ is kept fixed, and $q(t'')$ is varied by a small amount $\delta q(t'')$. Then

$$\delta R = \left. \frac{\partial L}{\partial \dot{q}} \delta q \right|_{t'}^{t''} + \int_{t'}^{t''} \left(\frac{\partial L}{\partial q} - \frac{d}{dt} \frac{\partial L}{\partial \dot{q}} \right) \delta q dt + \left(L - \frac{\partial L}{\partial q} \dot{q} \right) \delta t. \quad (2.2)$$

The second term is zero due to Lagrange's equations. In the first term we put $\delta q(t') = 0$ and we replace $\partial L / \partial \dot{q}$ by p . Hence the partial derivatives of R are:

$$\frac{\partial R}{\partial t''} = L - p'' \cdot \dot{q}'' = -H(\frac{\partial R}{\partial q''}, q''), \quad (2.3)$$

$$\frac{\partial R}{\partial q''} = p'' \quad (2.4)$$

where $H(p, q)$ is the Hamiltonian. The first equation is the Hamilton-Jacobi equation using the time-dependent action integral. To remove the time dependence we integrate (2.3) giving

$$S = \text{const} = R + H(t'' - t') = \int_{t'}^{t''} p \cdot dq. \quad (2.5)$$

This is the time-independent action integral. The Hamilton-Jacobi equations are:

$$H(\partial S/\partial q, q) = E, \quad (2.6)$$

$$p = \partial S/\partial q, \quad (2.7)$$

where we now drop the double prime for convenience. The definition of an integrable system is one for which a solution S of (2.6) exists, depending only on its position co-ordinates, and parametrised by N independent constants of the motion, I_i . That is,

$$S = S(q_1, \dots, q_N; I_1, \dots, I_N). \quad (2.8)$$

The constants I_i are not unique; S is invariant under any canonical transformation of them. One particular choice is for them to be the new momenta of the system. For such a choice, S becomes the generating function of the transformation:

$$p = \partial S/\partial q, \quad (2.9)$$

$$\theta = \partial S/\partial I = \omega t + \text{const.} \quad (2.10)$$

The new co-ordinates are (I, θ) . The angular velocity $\dot{\theta} = \partial H/\partial I = \text{const.} = \omega$, because H is quadratic in I and $\dot{I} = \partial H(I)/\partial \theta = 0$. The (I, θ) co-ordinates are called action-angle variables, for reasons to be given later.

The momenta I_i satisfy certain Poisson bracket relations:

$$[H, I_i] = 0 \quad (2.11)$$

which shows that they are conserved, and

$$[I_i, I_j] = 0 \quad (2.12)$$

which means that they are in involution with each other. $H = H(I)$ is the $(N + 1)^{\text{th}}$ constant of motion, but is dependent on the I_i . In practice, $N - 1$ constants of motion and the energy define the motion on an N -dimensional manifold in phase space. The ergodic hypothesis, that one trajectory can explore

the whole $(2N - 1)$ -dimensional energy surface (so that time averages are equal to space averages) is thus incorrect for integrable systems (except for the trivial case $N = 1$). If the motion is bounded, there exists a theorem in topology [36] which states that the N -manifold must be an N -torus (relying on how to ‘comb a hairy manifold’ with no bunching). The momentum I_i is then the ‘angular momentum’ around the i^{th} circuit \mathcal{C}_i of the torus (figure (2.2.1)), where \mathcal{C}_i is defined along a parallelised direction of the torus.

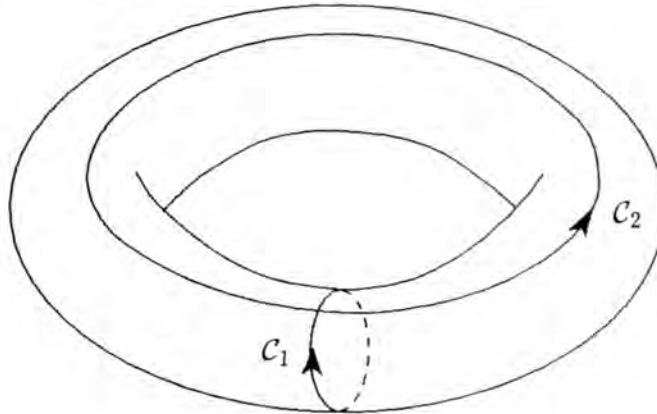


Figure 2.2.1. An invariant torus of an integrable system.

The circuits \mathcal{C}_i cannot be reduced, and this means that the action $S(q, I)$ around \mathcal{C}_i is multivalued, changing by an amount

$$\Delta S = \int_{\mathcal{C}_i} p.dq = \sum_i \text{area of projection of } \mathcal{C}_i \text{ onto the } (p_i, q_i)\text{plane.} \quad (2.13)$$

The momentum is thus

$$I_i = \frac{1}{2\pi} \int_{\mathcal{C}_i} p.dq. \quad (2.14)$$

For each time around the circuit \mathcal{C}_i , θ changes by

$$\Delta\theta_i = \Delta\partial_{I_i} S(q, I) = 2\pi. \quad (2.15)$$

Hence we have justified the name angle.

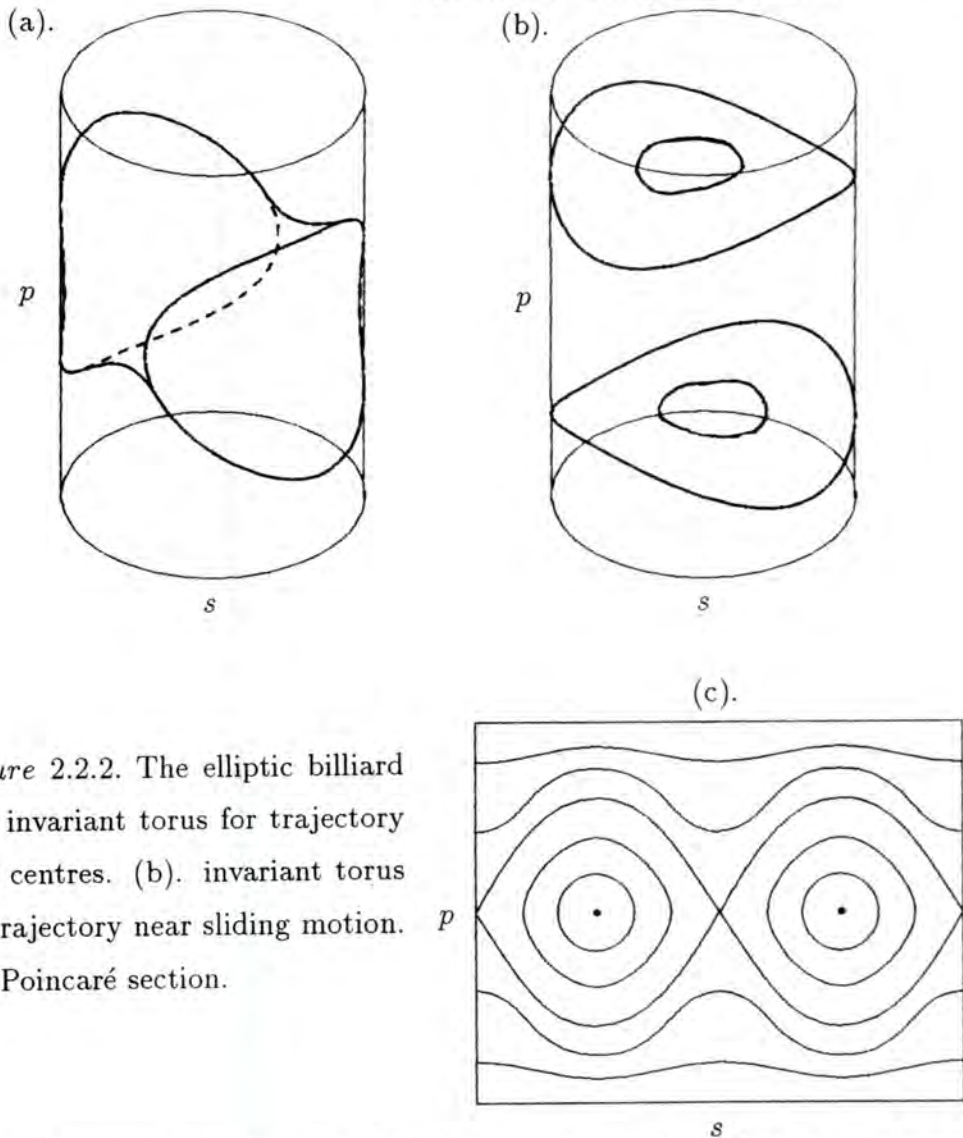


Figure 2.2.2. The elliptic billiard

- (a). invariant torus for trajectory near centres. (b). invariant torus for trajectory near sliding motion.
- (c). Poincaré section.

By changing the actions I_i , with the constraint $H(I) = E$, the invariant torus can be continuously varied through the energy surface. Sometimes the topology of the torus may change, through a ‘reconnection’. For instance, the hole in the torus may momentarily disappear, then reappear elsewhere. An example where this occurs is the elliptical billiard [37]. The two kinds of tori are shown in figure (2.2.2), where s is the arc length along the boundary, and p is the component of velocity tangential to the boundary. The reconnection we spoke of always occurs through an unstable fixed point.

We have now seen how the $2N$ -dimensional phase space is foliated with N -dimensional tori, but we would like to know how individual trajectories appear on the tori. It is easy to see that if the frequencies $\omega_1, \dots, \omega_N$ are mutually commensurable *i.e.* $(\omega_1, \dots, \omega_N) = (n_1, \dots, n_N)\omega_0$ (where n_i are integers) then

after n_i windings around each θ_i co-ordinate the trajectory will close, and this does not depend on the starting point on the torus. Hence such rational tori are completely filled by periodic orbits. For mutually incommensurable frequencies the orbit does not close, but densely fills the torus, and is ergodic on it. It is intuitive to suppose that a continuous and parabolic set of periodic orbits would be structurally unstable, because it is highly non-generic. This is indeed the case, and the system is no longer in general integrable, as we shall now see.

2.3 The KAM Theorem

Consider an integrable system, with action-angle variables I, θ and Hamiltonian $H_0(I)$. Now we add an nonlinear perturbation $\varepsilon V(I, \theta)$, so the new Hamiltonian is

$$H(I, \theta) = H_0(I) + \varepsilon V(I, \theta). \quad (2.16)$$

The old variables I, θ are no longer action-angle variables of the new system, but are still good canonically conjugate co-ordinates to use. We wish to see under what conditions we can define new variables I', θ' which *are* action-angle variables. *i.e.* we need to solve

$$H(I, \theta) = H'(I'). \quad (2.17)$$

This can be approached using the generating function $S(I', \theta)$; then this equation becomes

$$H(\partial_\theta S, \theta) = H'(I'). \quad (2.18)$$

Without perturbation S is simply $\theta \cdot I'$. So to first order in ε

$$\begin{aligned} S &= \theta \cdot I' + \varepsilon S_1(I', \theta) + \mathcal{O}(\varepsilon^2) \\ &= H_0(I') + \varepsilon [\partial_\theta S_1 \cdot \partial_{I'} H_0(I') + V(I', \theta)] + \mathcal{O}(\varepsilon^2). \end{aligned} \quad (2.19)$$

Now $\partial_{I'} H_0(I')$ is the unperturbed frequency vector $\omega_0(I')$. Also $V(I', \theta), S(I', \theta)$

are periodic in θ and hence can be written as Fourier series:

$$V(I', \theta) = \sum_{m=(m_1, \dots, m_N)} V_m(I') \exp(im.\theta) \quad (2.20)$$

$$S(I', \theta) = \sum_{m \neq 0} S_m(I') \exp(im.\theta) \quad (2.21)$$

Without loss of generality, the arbitrary constant of integration for $m = 0$ in the sum in the second expression is set equal to zero. Equating Fourier coefficients gives to first order in ε ,

$$H'(I') = H_0(I') + \varepsilon V_0(I') + \mathcal{O}(\varepsilon^2) \quad (2.22)$$

$$S(I', \theta) = \theta \cdot I' + i\varepsilon \sum_{m \neq 0} \frac{V_m(I')}{m \cdot \omega_0(I')} \exp(im.\theta) + \mathcal{O}(\varepsilon^2). \quad (2.23)$$

There now arise two difficulties which indicate the failure of perturbation theory in many cases:

- (a). the problem of convergence of the series in ε .
- (b). the problem of convergence of the sums over m .

Considering (b), we come back to the commensurability property of ω_0 , which can be restated as the property that $m \cdot \omega_0$ vanishes. Thus the sum over m diverges when ω_0 is commensurable (just considering one term for large enough m). However, it is not so clear what happens when ω_0 is incommensurable. Then $m \cdot \omega$ can be very small but never zero, and the sum may or may not diverge. This problem and the first difficulty were addressed by Kolmogorov, Arnol'd and Moser in the well known KAM Theorem [9] [8]. This theorem was constructed by an iterative process, applying perturbation theory at each step. In the two-dimensional case $N = 2$, the theorem states that tori 'close' to a rational value of ω_1/ω_2 do not survive. More quantitatively, if r/s is any rational number, then

$$\left| \frac{\omega_1}{\omega_2} - \frac{r}{s} \right| > \frac{K(\varepsilon)}{s^{2.5}} \quad \text{for all } r, s \quad (2.24)$$

is the condition for the tori to survive, where K is an unknown function. At first, it may seem that the set satisfying this condition is empty, because arbitrarily

close to any number is a rational number. But this measure of closeness is given by

$$\left| \frac{\omega_1}{\omega_2} - \frac{r}{s} \right| \lesssim \frac{1}{s^2}. \quad (2.25)$$

Thus, in general, some ratios of angular velocities will satisfy the KAM condition (2.24) and these are the ones closest to the upper bound of equation (2.25), called the ‘most’ irrational ratios. The rational and close to rational ratios (*i.e.* ones which satisfy equation (2.25) easily) are the first ones to be destroyed as ε is increased. The full statement of the theorem requires that ε is small, and that many derivatives of the Hamiltonian exist. Computationally, the theorem appears to apply more strongly than this, and the last torus to break up occurs when ε may be quite large. This torus is, as expected, the one when the ratio of angular velocities is a noble number (such as the golden mean) as these are the most irrational numbers.

2.4 Poincaré Surfaces of Section

A useful description of classical motion is the Poincaré map, surface of section or first return map (under its various names). Imagine a trajectory passing through a chosen surface, each time leaving a dot as it passes through in a particular direction. For a $2N$ -dimensional phase space, the Poincaré surface is $(2N - 2)$ -dimensional. Over a period of time, the trajectory will build up a series of dots on the surface. Suppose that (η, ξ) are co-ordinates on the surface (where η and ξ are $(N - 1)$ -dimensional vectors). Then the map

$$F(\eta_i, \xi_i) = (\eta_{i+1}, \xi_{i+1}) \quad (2.26)$$

is called the Poincaré map, and defines the generation of the whole set of points $(\eta_0, \xi_0), (\eta_1, \xi_1), \dots, (\eta_i, \xi_i), \dots$) corresponding to one trajectory (figure (2.4.1)). The important aspect of the Poincaré map is that the map F , and the surface

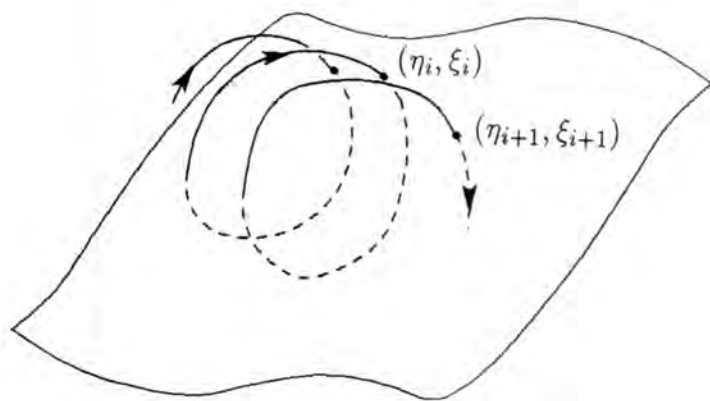


Figure 2.4.1. One trajectory as it passes through a Poincaré surface of section.

on which it is defined, uniquely determine the motion without the Hamiltonian: given η_0, ξ_0 and F , one can reconstruct the motion between (η_i, ξ_i) and (η_{i+1}, ξ_{i+1}) , and hence for all time.

Another important property is Liouville's theorem. This states that a volume element $dq_1 \dots dq_N dp_1 \dots dp_N$ in phase space is conserved under transportation by the Hamiltonian flow. Moreover, each individual area element $dq_i dp_i$ is also conserved. This means that if η, ξ are taken to be a set of canonically conjugate co-ordinates, then the 'area' $d\eta_1 \dots d\eta_{N-1} d\xi_1 \dots d\xi_{N-1}$ is conserved. In practice, only $N = 2$ systems have been extensively studied using Poincaré maps, and so this is a real area $d\eta_1 d\xi_1$.

We can use the area-preserving property to prove the Poincaré-Birkhoff theorem, which states that the commensurable periodic orbits $\omega_1/\omega_2 = r/s$ are not all destroyed under perturbation, but an even multiple of s fixed points of F^s remain. Suppose we have three tori of an integrable map F_0 , one \mathcal{T} with rational frequency ratio r/s , one with slightly greater, \mathcal{T}_+ , and one with slightly less, \mathcal{T}_- . Then under F_0^s , \mathcal{T} does not move, \mathcal{T}_+ rotates anticlockwise, \mathcal{T}_- rotates clockwise (figure (2.4.2)). Now when the map is perturbed to F_ε with ε small enough, these twists are preserved. Consider a curve R_ε , for which, like \mathcal{T} under F_0^s , the angular co-ordinate at each point is unchanged under F_ε^s . So R_ε is close to \mathcal{T} . Applying F_ε^s again to R_ε generates another closed curve $F_\varepsilon^s R_\varepsilon$. This must intersect R_ε , because it has the same area, and must enclose the fixed point O of F , and it must also intersect an even number of times (except for non-generic

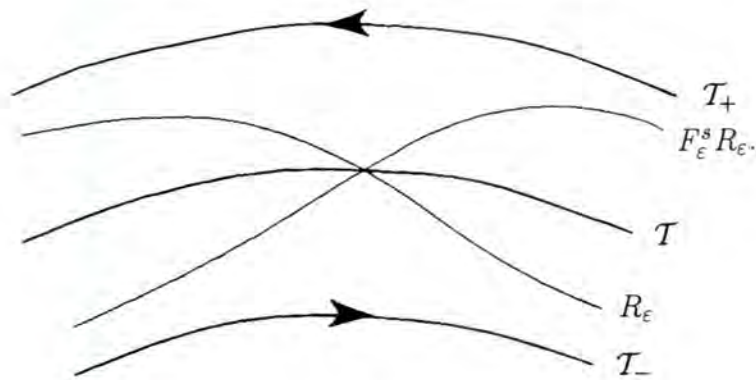


Figure 2.4.2. The Poincaré-Birkhoff theorem.

parabolic cases). These points are thus fixed points of F_ϵ^s , and each one generates a whole set of s fixed points, giving a total of $2ks$ fixed points, where k is an integer. It can be shown further that the fixed points alternate between elliptic and hyperbolic types, so the destroyed torus is replaced by many higher frequency tori. It is obvious from the continuity of the twist directions that this is the only possibility.

There is another structure which we have not yet discussed. This is the shape of the stable (unstable) manifolds whose points asymptotically converge (diverge) to (from) the hyperbolic fixed points. We have seen this already for the elliptical billiard (figure 2.2.2(c)), where the curves asymptotically diverge from one fixed point and asymptotically converge to the other. This is called a heteroclinic connection. Another possibility is a homoclinic connection where the curve is asymptotic at both ends to the same fixed point. Generically this is not the case. The curves may not join smoothly, but intersect each other (but not themselves—this is excluded by uniqueness!), at a homoclinic or heteroclinic point X (figure (2.4.3)). But by continuity, the neighbourhood of X must resemble the neighbourhood of $F(X)$, and hence by iteration there must be an infinity of these homoclinic (heteroclinic) points. In order for this to happen the interval between X and $F(X)$ must shrink. But the area \mathcal{A} enclosed by the two manifolds must remain constant. Thus the curve H_u becomes ever more convoluted as the intersections of H_u with H_s approach H . The same is true for H_s as the intersections of H_u with H_s diverge from H . Poincaré wrote:

"The intersections form a kind of lattice, web or network with infinitely tight

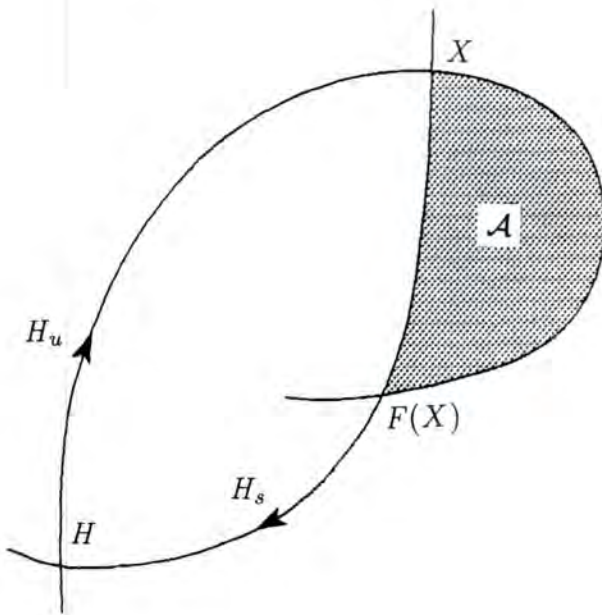


Figure 2.4.3. Homoclinic connections between stable and unstable manifolds.

loops; neither of the two curves must ever intersect itself, but it must bend in such a complex fashion that it intersects all the loops of the network infinitely many times.

“One is struck by the complexity of this figure which I am not even attempting to draw. Nothing can give us a better idea of the complexity of the three body problem and of all problems of dynamics where there is no holomorphic integral and Bolin’s series diverge.” [7] (Vol. III, p389)

There is one last structure to be discussed, and whereas the previous one has been known for nearly a century, this has been discovered relatively recently in 1978. It is known as the Cantor invariant torus or cantorus, and was proposed by Percival [38] and Aubry [39]. The basic idea is that as the strength of the perturbation is increased, the tori of highly irrational frequency, being the most structurally stable ones are not destroyed in the same way as the rational and close to rational tori. Instead, the tori break up into a Cantor set of invariant curves, named cantori.

2.5 Strongly Chaotic Motion

We have seen that regular features exist in generic non-integrable systems, but that other features exist that are so complex that their structure, either analytically or graphically, is beyond description. The language of evolution equations and their solutions is no longer a useful way of looking at this complexity, and in this section we shall develop some of the ideas that extend the analysis of complexity beyond.

The first idea is the concept of chaotic motion. We have seen that points initially lying on an invariant manifold are mapped under the action of F onto an infinitely convoluted curve, so that the final point is extremely sensitive to the initial point. Over a long period of time, the final point is effectively unpredictable from the initial point. When such sensitivity occurs for every point in a finite region of phase space, the motion is said to be chaotic within that region. Associated with this is also the property of indecomposability—that the region cannot be decomposed into parts which do not communicate, and regularity—that there exist periodic points that are dense in the region. These three properties define chaotic motion.

Sensitivity on initial conditions is measured by the Lyapunov exponent, which is the maximal exponent of the divergence of nearby trajectories averaged in the limit as $t \rightarrow \infty$. If the Lyapunov exponent is negative or zero, the motion is not sensitive on initial conditions, because over long time periods nearby trajectories diverge at most linearly, and the motion is regular. If the Lyapunov exponent is positive, then nearby trajectories diverge exponentially, and the motion is chaotic. For conservative systems, and area-preserving maps, the Lyapunov exponent is zero or positive, because such maps do not contract the flow. Positive exponents are allowed, because these maps can contract and expand the flow at the same time, and since the maximal exponent is measured, only the expansion is measured. Physically, if $D_0(x)$ is the separation at $t = 0$ of two trajectories in phase space close to x , and $D_t(x)$ is their separation after time t , then the Lyapunov exponent $\Lambda(x)$ is defined by

$$\Lambda \equiv \lim_{t \rightarrow \infty} \frac{1}{t} \log \left(\frac{D_t}{D_0} \right) \quad (2.27)$$

The second idea, from Kolmogorov's information theory [14], is the concept of algorithmic complexity, defined as the ratio \mathcal{C} of the minimum input information and the program length to the output information of a computer program or algorithm. The input information may be the number of bits required to specify an input real variable to a given accuracy for a given problem (say the initial point for a dynamical system), or it may be a list of parameters required to define an approximation to a curve. Together the input information and the computer program define the problem. The output information may be number of bits of an output string of numbers (say points on the trajectory of the dynamical system), or the list of points defining the curve to a given accuracy. Suppose we take the limit as the approximation tends to zero (or as the length of the orbit tends to infinity). Then if \mathcal{C} tends to a finite constant, the input information required to define the problem is 'as great' (the same cardinality) as the information contained in the solution. For instance, to define a chaotic trajectory exactly, the information required for the initial point is as great as the information contained in the whole orbit. The information required to define stable and unstable manifolds of a hyperbolic fixed point is as great as the information contained in the points of the manifolds themselves. Such complexity distinguishes chaotic from non-chaotic motion. Thus, a problem is defined to be algorithmically complex if $\mathcal{C} \rightarrow \text{const.}$ as $t \rightarrow \infty$ (or the length of the output string $\rightarrow \infty$), and the output string is itself the shortest representation of the solution, and it is said to be algorithmically incompressible.

Algorithmic complexity is akin to randomness, and this is particularly apparent for the case of a Bernoulli sequence. This is a sequence of random symbols or digits—let us for simplicity choose a random number in base two in the interval $[0, 1]$, $0.a_1a_2\dots a_i\dots$, where a_i is either 0 or 1. Then one shifts the sequence left (by multiplication by two) and keeps the fraction for the next iteration, taking the digit a_0 away as the result. The digits generated $a_0, a_1, \dots, a_i, \dots$ by the process are equivalent to coin tosses, 1 for heads, 0 for tails. Suppose now the sequence is not random, but the same process is used to reveal the digits of a given number, the digits again representing heads or tails, with the number representing the initial conditions of a perfect die. In order to determine the full

sequence of heads and tails, one must know the number to exponential accuracy, and the process is algorithmically complex. If, as must be true in practice, the number is known only to a finite number of digits, then the sequence of heads and tails after that is effectively random.

One of the important methods of ergodic theory is to code a chaotic trajectory by a sequence of symbols $\dots s_{-1}s_0s_1\dots$ so that each trajectory is in one-one correspondance with a sequence, and hence prove that a particular system is a Bernoulli system (*i.e.* trajectories are indistinguishable from random ones). The sequence, at once, represents all the points on the trajectory, because the action of the Poincaré map is simplified to trivially shifting the sequence left to find the next point (positive t), and right to find the previous point (negative t). The value of a symbol represents a partition of phase space. The symbol s_0 partitions the whole phase space, s_1 partitions each partition of s_0 and so on. In the direction of negative time, s_{-1} is partitioned by s_0 and so on. If the sequence repeats itself forever, it represents a periodic orbit; if it does not then it is a chaotic orbit; if it does not repeat itself at one end, but does at the other then it is a trajectory on a stable or unstable manifold.

Information theory was used to calculate the content of a digital signal (communicating the pages of a book, or the music of the London Philharmonic Orchestra, or the first 3 billion decimal places of π , for instance) and find out how this information could be compressed. With each subsequence i is associated a probability p_i of that particular sequence appearing in the whole sequence. So if we had an ensemble of ν sequences, we would expect i to appear $\nu_i = p_i\nu$ times. Thus the total number of states of the ensemble is

$$\Omega = \frac{\nu!}{\nu_1! \dots \nu_i! \dots \nu_n!} \quad (2.28)$$

for n subsequences. In the same way as in statistical mechanics, we define the entropy of the sequence to be

$$\begin{aligned}
 h_{SM} &= \frac{\text{entropy of ensemble}}{\nu} = \log \Omega/\nu \\
 &\approx \log \nu - \frac{1}{\nu} \sum_i \nu_i \log \nu_i = - \sum_i \frac{\nu_i}{\nu} \log \left(\frac{\nu_i}{\nu} \right) \\
 &= - \sum_i p_i \log p_i.
 \end{aligned} \tag{2.29}$$

This measures the disorder or chaos of the sequence. Thus sequences that repeat a subsequence i have a probability $p_i = 1$ of appearing, so $h_{SM} = 0$. A random binary digit has $p_n = 2^{-n}$ for a subsequence of length n , and hence its entropy is $h_{SM} = \sum_n 2^{-n} n$. It is not easy to show, but the probability p_i is related to the Lyapunov exponent, and it can be shown that, if x is a trajectory and s is its symbol sequence with probabilities p_i , then

$$\Lambda(x) = - \sum_i \log p_i \tag{2.30}$$

and the Kolmogorov entropy h_{KS} [12] is

$$h_{KS} = \int d\mu \Lambda(x) = - \sum_i p_i \log p_i. \tag{2.31}$$

2.6 Stationary Billiards

A classical billiard system is defined to be the free motion of a point-like classical particle within a two-dimensional region, bounded by a closed hard-walled enclosure. The collisions with the wall are perfectly elastic (with the angle of reflection equal to the angle of incidence) and instantaneous.

Billiards are good systems to study. Firstly, they are mathematically simple, but still exhibit all the properties associated with non-integrable systems of two freedoms. This is because all of the nonlinearity of the problem is compressed into the interaction with the wall, leaving free motion between bounces. Secondly, $N = 2$ is the minimum freedoms required for chaotic motion. Thirdly,

they are the most convenient systems to study quantum mechanically—the quantum equivalent is related to the ‘drum’. Lastly, Birkhoff [6] has remarked on the generality of billiard systems.

In order to study billiards, we would like to define an appropriate Poincaré map. The surface of section that seems most obvious is the section through phase space where the particle hits the boundary. There are always two directions through which the trajectory can pass through the surface. In this case, there is the phase point immediately before impact, and the phase point immediately after impact. We use the latter. There are now two co-ordinates which define the motion of the particle: its position on the boundary (arc length s from a reference point), and its direction of motion after impact (angle of projection ψ with the forward tangent)—figure (2.6.1). The speed of the particle is conserved, and with the mass can be rescaled to be equal to one. It so happens that the canonically conjugate variables to use are s and $p \equiv \cos \psi$ (for proof see [37]). Thus the Poincaré map $(s_{n+1}, p_{n+1}) = F(s_n, p_n)$ is area-preserving. Unfortunately, this does not hold for rotating billiards, because the speed does not remain constant, but it does still apply for billiards in uniform magnetic fields.

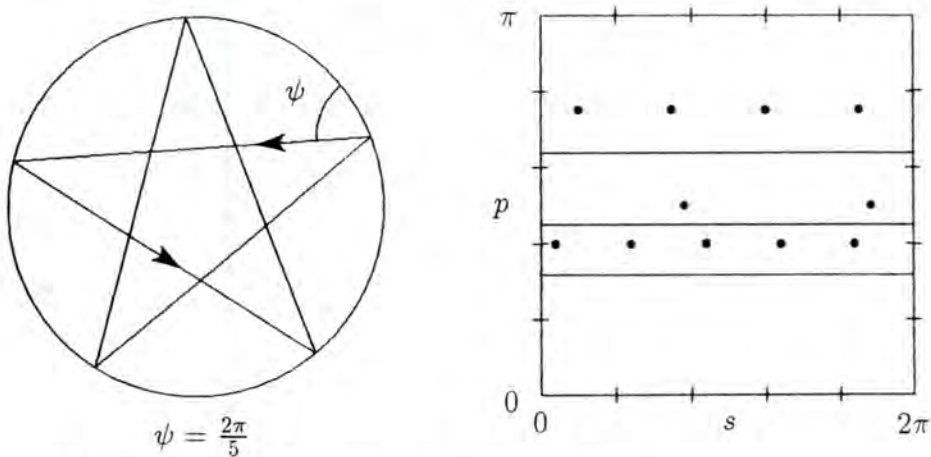


Figure 2.6.1. The circular billiard and Poincaré map.

The class of billiards offers a wide variety of types of motion, ranging from perfectly regular to Bernoulli systems. The circular, rectangular and elliptic billiards are integrable. Oval billiards have both regular and chaotic regions [37], similar to those predicted by KAM, although there does not exist a KAM

theorem for billiards. The Sinai billiard and the stadium of Bunimovich are the most chaotic systems of all.

Ergodic theorems exist for billiards, but tend to be specific to particular systems. This is due to the variety of billiards themselves rather than a failure of the mathematicians. Using ergodic theory and ideas from Sinai's work, Bunimovich proved that the stadium billiard is a K-system (and, more recently, Bernouilli) and Sinai has proved that the Sinai billiard is Bernouilli. Lazutkin has shown that billiards with convex boundaries that are C^{553} smooth are not ergodic (*i.e.* some tori exist). Polygonal billiards are shown to have zero entropy—and are hence regular—but singularities in the Poincaré section mean that the invariant manifolds are not tori, but compact manifolds with genus greater than one. Berry and Robnik have studied systems, such as the Africa billiard and heart-shaped billiards, where concave portions of the boundary cause defocusing of trajectories and lead (computationally) to ergodicity. They are also the only ones (as far as I know) to study billiards which approach the generality of Birkhoff—billiards under the influence of a uniform magnetic field (which is equivalent to a rotating billiard with a harmonic oscillator field at the centre of rotation strong enough to cancel the centrifugal field).

The circular billiard is the integrable limit of the rotating circular billiard, when the speed of the particle tends to infinity, or the speed of rotation tends to zero. The frequency ratio $\beta \equiv \omega_1/\omega_2$ is simply ψ/π . Thus trajectories are ergodic on the torus for β irrational, and periodic for β rational. We expect the tori with β close to a rational value to be destroyed and replaced by island chains according to the Poincaré-Birkhoff theorem, when the system is perturbed by rotation.

2.7 Semiclassical Mechanics of Chaotic Systems

In this section, following the review by Gutzwiller [19] [20], and the work by Balian and Bloch, we will develop semiclassical mechanics from the Feynman path integral to the Gutzwiller trace formula.

The Feynman path integral for the propagator is

$$K(q'q''t't'') = \int_{q(t')t'}^{q(t'')t''} \mathcal{D}(q(t)) \exp \left\{ \frac{i}{\hbar} \int_{t'}^{t''} dt L(q, \dot{q}, t) \right\}, \quad (2.32)$$

where K satisfies the Schrödinger equation $i\hbar(\partial K/\partial t'') - HK = 0$, and the wavefunction is defined by $\psi'' = \int dq' K''' \psi'$. For a quickly changing phase (*i.e.* when \hbar is small), the main contribution to K comes from when the phase is stationary. This is the contribution from classical mechanics, if the stationary point is a minimum. The term in the exponent for this path is the Hamilton principal function, R (equation (2.1)). The first variation of R is zero and gives the equations of motion (equations (2.3), (2.4)). The second variation of R is important for semiclassical mechanics. For this, one needs to regard the Feynman integral more carefully, considering each path as discretised into $M + 1$ points, $q' = q_0, q_1, \dots, q_M = q''$ and $t' = t_0 \leq t_1 \leq \dots \leq t_M = t''$, and taking the limit as $M \rightarrow \infty$ to regain the continuum result. Thus

$$K = \lim_{M \rightarrow \infty} \underbrace{\prod_{i=1}^M \left[\frac{m}{2\pi i \hbar (t_i - t_{i-1})} \right]^{\frac{N}{2}} \int d^N q_1 \dots \int d^N q_M e^{iR_M/\hbar}}_{\mathcal{D}_M(q(t))}, \quad (2.33)$$

where

$$R_M = \sum_{i=1}^M (t_i - t_{i-1}) L \left(\frac{q_i - q_{i-1}}{t_i - t_{i-1}}, q_i, t \right). \quad (2.34)$$

Now we consider the variation of R_M with q_0, q_M fixed, and q_1, \dots, q_{M-1} varying. When R_M is stationary the path is approximately the classical one. So this gives the $e^{iR/\hbar}$ phase contribution. The second variation is the next non zero term, and gives a contribution from each of the path segments q_{i-1} to q_i , $i = 1, \dots, M - 1$. This variation is

$$\delta^2 R = \frac{1}{2} \sum_{i,j=1}^{M-1} R_{ij} \delta q_i \delta q_j + \mathcal{O}((\delta q)^3). \quad (2.35)$$

Note that the matrix R_{ij} is larger than it seems because δq_i is an N -column

vector. So R_{ij} has dimension $N(M - 1)$. Thus the contribution to K is

$$\int \mathcal{D}_M(q(t)) \exp \left\{ \frac{i}{2\hbar} \sum R_{ij} \delta q_i \delta q_j \right\}. \quad (2.36)$$

The integral is performed by diagonalising R_{ij} and evaluating the $N(M - 1)$ Fresnel integrals with respect to the eigenvectors ξ of R_{ij} . Each Fresnel integral gives a contribution

$$\int_{-\infty}^{\infty} d\xi \exp \left(\frac{i}{2\hbar} \xi \lambda \xi \right) = \frac{(2\pi\hbar)^{\frac{1}{2}}}{\sqrt{\lambda}} \exp(i\pi \text{sign}(\lambda)/4), \quad (2.37)$$

where λ is the eigenvalue. Thus expression (2.36) becomes

$$\frac{1}{(2\pi i\hbar)^{\frac{N}{2}}} \prod_{i=1}^M \left(\frac{m}{t_i - t_{i-1}} \right)^{\frac{N}{2}} \frac{\exp(-i\pi\mu/2)}{(\det R_{ij})^{\frac{1}{2}}}. \quad (2.38)$$

where μ is the number of negative eigenvalues of R_{ij} (the positive ones cancel phase with the \sqrt{i} factors in the denominator of equation (2.33)). It can be shown that

$$\lim_{m \rightarrow \infty} \prod_{i=1}^M \left(\frac{m}{t_i - t_{i-1}} \right)^N (\det R_{ij})^{-1} = \det \left(\frac{\partial p'}{\partial q''} \right), \quad (2.39)$$

but this is not a trivial result, and the reader is referred to Morette [42] and Papadopoulos [43].

The Jacobian $\partial p'/\partial q''$ shows how the initial momentum varies as the final position varies. Suppose we choose to vary q'' along one of the eigenvectors of $\delta p' = (\partial p'/\partial q'') \delta q''$ (figure (2.7.1)), then p' varies along its eigenvector. However we can see that if q'' lies on a caustic, then we are restricted in our choice for $\delta q''$. Mathematically, $\partial p'/\partial q''$ is reduced in rank. Also for values of q'' on the other side of the point on the caustic (called a conjugate point), p will vary in the opposite direction for that eigenvector. In other words, the relevant eigenvalue of $\partial p'/\partial q''$ has changed sign.

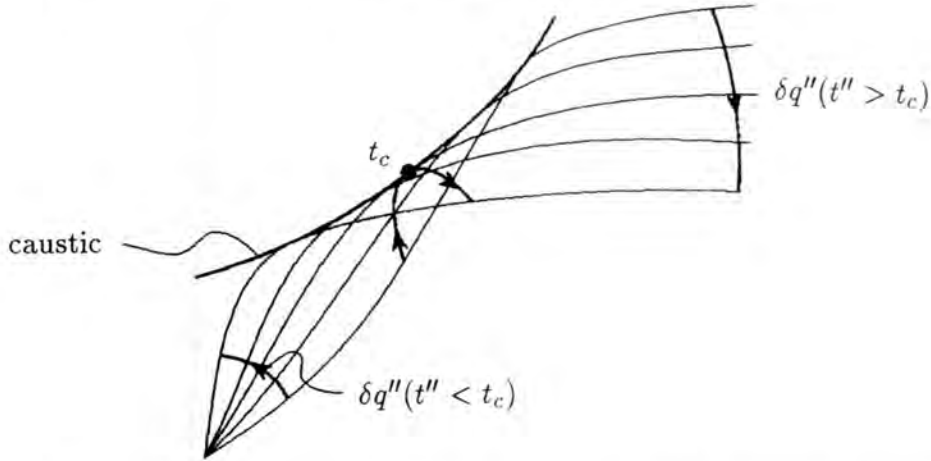


Figure 2.7.1. A typical set of paths with varying initial momentum, passing through a conjugate point at time t_c .

It can be easily seen that the number of times an eigenvalue of $\partial p'/\partial q''$ changes sign is equal to the number of negative eigenvalues of R_{ij} . That is μ is the number of conjugate points between t' and t'' , called the Maslov index. Now

$$\frac{\partial p'}{\partial q''} = -\frac{\partial^2 R}{\partial q'' \partial q'}, \quad (2.40)$$

hence the complete formula for the semiclassical propagator is

$$K(q'q''t't'') \approx \sum_{\text{cl. tr.}} \frac{1}{(2\pi i\hbar)^{\frac{N}{2}}} \det^{\frac{1}{2}} \left(-\frac{\partial^2 R}{\partial q'' \partial q'} \right) \exp \left\{ \frac{i}{\hbar} R(q'q''t't'') - \frac{i\pi}{2} \mu \right\}. \quad (2.41)$$

Since we shall be using time-independent solutions of the Schrödinger equation, we shall want to work with the constant energy Green function, which can be written in terms of the propagator by

$$G(q'q''E) = \frac{1}{i\hbar} \int_0^\infty dt K(q'q''t't'') \exp \left(\frac{i}{\hbar} Et \right) \quad (2.42)$$

where $t = t'' - t'$. The Green function satisfies the equation

$$(E - \hat{H})G(q'q''E) = \delta(q'' - q'). \quad (2.43)$$

We use the usual method for evaluating the integral; we analytically continue G onto the complex plane, making E complex by adding a small imaginary part

$i\varepsilon$, and enforcing $G(q'q''E) = [G(q'q''E^*)]^*$. On substituting equation (2.41), the integral is a Laplace integral, and can be performed approximately by stationary phase. The factor in the exponent is the action integral

$$S = R + Et. \quad (2.44)$$

which is stationary with respect to time when $\partial R/\partial t = -E$. The second variation with respect to time gives $\frac{1}{2}(\partial^2 R/\partial t^2)(\delta t)^2$, which is again a quadratic form giving the Fresnel integral

$$\int_0^\infty dt \exp \left\{ \frac{i}{2\hbar} \frac{\partial^2 R}{\partial t^2} (\delta t)^2 \right\} = \frac{(2\pi\hbar)^{\frac{1}{2}}}{|(\partial^2 R/\partial t^2)|^{\frac{1}{2}}} \exp \left\{ \frac{i\pi}{4} \text{sign}(\partial^2 R/\partial t^2) \right\}, \quad (2.45)$$

so that the Green function becomes

$$G(q'q''E) \approx \sum_{\text{cl. tr.}} \frac{2\pi}{(2\pi i\hbar)^{\frac{N+1}{2}}} \frac{\det |\partial^2 R/\partial q' \partial q''|^{\frac{1}{2}}}{|\partial^2 R/\partial t^2|^{\frac{1}{2}}} \exp \left(\frac{i}{\hbar} S - \frac{i\pi}{2} \nu \right), \quad (2.46)$$

where ν differs from μ by, at most, one. Suppose that q_0 is the co-ordinate along the trajectory, then it is easy to show that

$$\begin{aligned} \frac{\det (-\partial^2 R/\partial q' \partial q'')}{(\partial^2 R/\partial t^2)} &= -\det \begin{pmatrix} \frac{\partial^2 S}{\partial q' \partial q''} & \frac{\partial^2 S}{\partial q' \partial E} \\ \frac{\partial^2 S}{\partial E \partial q''} & \frac{\partial^2 S}{\partial E^2} \end{pmatrix} \\ &= \frac{1}{\dot{q}' \dot{q}''} \det' \left(-\frac{\partial^2 S}{\partial q' \partial q''} \right) \end{aligned} \quad (2.47)$$

where the prime indicates the omission of the first row and column, because S does not change along q_0 . Hence

$$G(q'q''E) \approx \sum_{\text{cl. tr.}} \frac{2\pi}{(2\pi i\hbar)^{\frac{N+1}{2}}} \frac{1}{(\dot{q}' \dot{q}'')^{\frac{1}{2}}} \det'^{\frac{1}{2}} \left(-\frac{\partial^2 S}{\partial q' \partial q''} \right) \exp \left(\frac{i}{\hbar} S - \frac{i\pi}{2} \nu \right). \quad (2.48)$$

One comment on ν : the conjugate points of $\partial p'/\partial q''$ are cancelled by the $\partial^2 R/\partial t^2$ term, but between these conjugate points are new ones, alternate with the old. Thus on average, the number of conjugate points are equal, but may sometimes differ by one (*i.e.* $\nu = \mu(+1)$). For fuller arguments consult [44]. The new conjugate points are also those of $\partial^2 S/\partial q' \partial q''$.

The exact Green function can be written in terms of the eigenfunctions $\phi_j(q)$ of $\hat{H}\phi_j = E_j\phi_j$ giving

$$G(q'q''E) = \sum_j \frac{\phi_j(q'')\phi_j^*(q')}{E - E_j}. \quad (2.49)$$

So

$$\int d^N q [G(q'q''E)]_{q'=q''=q} = \sum_j \frac{1}{E - E_j} \int d^N q \phi_j(q)\phi_j^*(q) = \sum_j \frac{1}{E - E_j}. \quad (2.50)$$

We define $g(E) \equiv \sum \frac{1}{E - E_j}$ so

$$g(E) = \int d^N q [G(qqE)]. \quad (2.51)$$

Again we see that the greatest contribution comes from those orbits where the phase is stationary, because otherwise $\exp\{iS(qqE)/\hbar\}$ varies wildly and destructive interference occurs for $\delta S \gg \hbar$. Thus we consider the sum over classical trajectories in equation (2.48) as though it were an integral and consider variations of S , where the endpoints are the same *i.e.* when $q = q' = q''$. Since $\delta S = 0$ we have

$$\left. \frac{\partial S}{\partial q} \right|_{q=q'=q''} = \left(\frac{\partial S}{\partial q''} + \frac{\partial S}{\partial q'} \right)_{q=q'=q''} = p'' - p' = 0. \quad (2.52)$$

Hence the main contribution comes from trajectories whose endpoints have the same momenta as well as position, that is from periodic orbits. The action $S(qqE)$ does not depend on where on the periodic orbit one starts, so we only consider variations normal to the periodic orbit. The second variation of S has the quadratic form

$$\delta^2 S = \left. \frac{\partial^2 S}{\partial q^2} \right|_{\perp} (\delta q)^2 = \delta q \left[\frac{\partial^2 S}{\partial q''^2} + \frac{\partial^2 S}{\partial q'\partial q''} + \frac{\partial^2 S}{\partial q''\partial q'} + \frac{\partial^2 S}{\partial q'^2} \right]_{\perp} \delta q \quad (2.53)$$

where δq has $(N - 1)$ components normal (\perp) to the periodic orbit and $\partial^2 S / \partial q^2$ is an $(N - 1)$ by $(N - 1)$ matrix. Thus the stationary phase approximation,

as before, gives a $\det^{-\frac{1}{2}}(\partial^2 S/\partial q^2)$ contribution to the amplitude and a phase factor of $\sum_{N=1} \pm i\pi/4$ where the signs are given by the signs of the eigenvalues of $\partial^2 S/\partial q^2$. Having done the $(N - 1)$ integrals with respect to q , we are left with the closed integral around the periodic orbit. This combines with other factors to give

$$\oint dq \left[\frac{1}{(\dot{q}'\dot{q}'')^{\frac{1}{2}}} \right]_{\dot{q}'=\dot{q}''=\dot{q}} \det^{\frac{1}{2}} \left(-\frac{\partial^2 S}{\partial q' \partial q''} \right) = \oint d\tau \det^{\frac{1}{2}} \left(-\frac{\partial^2 S}{\partial q' \partial q''} \right). \quad (2.54)$$

The other factors can be shown to be constant along the periodic orbit, and so the integral gives simply T_j , the period of the primitive periodic orbit.

The determinant of $\partial^2 S/\partial q^2$ can be evaluated using the monodromy matrix or tangent map M of the Poincaré map. This is the matrix which describes the local linear transformations of displacements between close trajectories, under the action of the map. Suppose $\delta x'$ is a $(2N - 1)$ -dimensional vector on the surface of section, and $\delta x''$ is this vector after the first return, then

$$\delta x'' = M \delta x'. \quad (2.55)$$

It can be shown that the characteristic equation

$$F(\sigma) = |M - \sigma I| \quad (2.56)$$

whose zeros determine the Lyapunov exponents: $F(e^{i\Lambda}) = 0$, can be expressed as

$$F(\sigma) = \frac{\det (\sigma \partial^2 S/\partial q''^2 + \partial^2 S/\partial q' \partial q'' + \partial^2 S/\partial q'' \partial q' + \partial^2 S/\partial q'^2)}{\det (\partial^2 S/\partial q' \partial q'')} \quad (2.57)$$

Hence the ratio of determinants in the equation for $g(E)$ are simply $1/F^{\frac{1}{2}}(1)$, and we obtain Gutzwiller's semiclassical trace formula:

$$\sum \frac{1}{E - E_j} \equiv g(E) \approx g_0(E) + \underbrace{\frac{1}{i\hbar} \sum_{j,n} \frac{T_j}{[F_j(1)]^{\frac{1}{2}}} \exp \left(\frac{i}{\hbar} n S_j - \frac{i\pi}{2} n \alpha_j \right)}_{g_{\text{osc}}(E)}. \quad (2.58)$$

where n is the number of repetitions of the j^{th} primitive periodic orbit. The conjugate points are related to the old ones by $\alpha = \nu(+1)$, where the $(+1)$

means there may be one extra conjugate point due to the $\partial^2 S / \partial q^2$ term. The term $g_0(E)$ is the asymptotic contribution due to zero length paths which do not go anywhere else other than starting and ending at $q = q' = q''$. It is related to the Weyl formula for the density of states, and will be discussed in a later section. It depends only on geometric (rather than dynamical) properties of the system, such as the shape and perimeter of the boundary, and the volume that it contains.

There are some important remarks to make about equation (2.58). Firstly, being a semiclassical sum rule, it relates purely quantum mechanical quantities on the left hand side—energy eigenvalues—to purely classical quantities on the right hand side—periods of closed orbits, classical actions, Maslov indices, stability exponents, and geometry. Secondly, it is conditionally convergent at best, and so great care has to be taken in enumerating the infinite sum, in particular in the ordering of the terms, and in obtaining all the periodic orbits. This is no easy task for a general system—orbits proliferate exponentially with length for a chaotic system, and so coding the orbits is very important. This is possible for completely chaotic systems, but as yet no scheme has been found for mixed systems. One way of obtaining convergence is to smooth $g(E)$, by for example Gaussian smearing [45].

Some remarks of Berry [24] are made below. The energy wavelengths ΔE_j of the oscillatory terms in equation (2.58) are given by

$$\frac{n}{\hbar} [S_j(E + \Delta E_j) - S_j(E)] = \frac{n}{\hbar} \frac{dS_j}{dE} \Delta E_j = \frac{n}{\hbar} T_j \Delta E_j. \quad (2.59)$$

Hence

$$\Delta E_j = \frac{2\pi\hbar}{nT_j(E)}. \quad (2.60)$$

The mean level spacing $\langle \Delta E \rangle$ is given by the asymptotic rule that an eigenvalue takes up a volume h^N in phase space so that $\langle \Delta E \rangle \sim h^N / \frac{dV}{dE}$. Hence the oscillations in the RHS of the sum are on a scale much larger than the level spacing.

The importance of ordering is apparent if we sum over all repetitions of a periodic orbit before summing over other orbits. Then for some energy E_k , such that $S_j(E_k) = 2\pi k + \frac{\pi\alpha_j}{2n}$, the contribution to $g(E)$ is $\sum_n e^{2i\pi kn} \dots$, and there would be delta peaks or Lorentzian peaks at E_k . However, these cannot be at the correct eigenvalues, because the spacing is approximately \hbar . The problem is that we were summing periodic orbits of very different periods nT_j . We should have ordered the periodic orbits (not just primitive ones) in increasing period nT_j before summing. There is also a cutoff period, determined by summing over all periodic orbits whose wavelength ΔE_j is greater than the mean level spacing $\langle \Delta E \rangle$, so that the true eigenvalues emerge, and higher frequency ‘noise’ is avoided. *i.e.*

$$\frac{2\pi\hbar}{nT_j} > \frac{\hbar^N}{dV(E)/dE}$$

$$nT_j < T_{\max} \equiv \frac{dV(E)/dE}{\hbar^{N-1}}. \quad (2.61)$$

For strongly chaotic systems, because the number of isolated periodic orbits proliferate exponentially with the period, the Gutzwiller trace formula is an impractical way of finding the energy levels. However, the only other way is by matrix diagonalisation. Even though this is also computationally intensive, the number of steps required are a power of $1/\hbar$, rather than exponential in $1/\hbar$, and hence it is still much faster.

For integrable systems the situation is much better. There is an extension of the Bohr-Sommerfeld-Einstein semiclassical quantisation formula, which has been developed from modern classical mechanics and the KAM theorem. It is called torus quantisation and is introduced in the next section.

2.8 Torus Quantisation of Integrable Systems

Consider an integrable system, as defined in section (2.2), having N constants of motion I_i of the classical system given by

$$I_i = \frac{1}{2\pi} \oint_{C_i} p_i dq = \frac{\Delta S_i}{2\pi}. \quad (2.62)$$

The semiclassical Green function for integrable systems, corresponding to equa-

tion (2.58) will have a similar phase, but depending on the action for the torus, rather than for a periodic orbit. The Green function must be single-valued so the phase change around the circuit \mathcal{C}_i must be $2\pi m_i$, where m_i is an integer. Hence

$$I_i = (m_i + \frac{1}{4}\alpha_i)\hbar. \quad (2.63)$$

Thus the classically conserved quantities are quantised in steps of \hbar and give rise to N independent quantum numbers $m = (m_1, \dots, m_N)$ which label the energy eigenvalues by virtue of

$$E_m = H_{cl} \left((m + \frac{1}{4}\alpha)\hbar \right). \quad (2.64)$$

This is a generalisation of the Bohr-Sommerfeld model of angular momentum quantisation, which was first realised by Einstein [46] although in his treatment the $\alpha/4$ term was neglected, because this had not yet been discovered in classical mechanics.

We see that semiclassically we can represent states as points I_m on a regular lattice in action space (figure (2.8.1)). The energy spectrum given by equation (2.64) is then simply the projection of these points onto the E co-ordinate (*i.e.* the co-ordinate perpendicular to the energy surface $E = H(p, q)$). Thus the spectrum is ‘regular’. However, if we only know E_m and not I_m there is some loss of information about the spectrum. In particular, the ordering of the labels m is lost in the projection, and we can thus associate statistical properties with the spectrum, which will be discussed in section (2.10).

This even more so for large m , where the ‘wood’ is thicker so that consecutive eigenvalues, with energy surfaces of radius in I -space of approximately $\hbar R$, can have m_i differing by as much as R . Berry and Tabor [47] more rigorously use these arguments to derive the Poisson formula for the level spacing distribution for integrable systems.

We may derive a similar formula to the Gutzwiller trace formula (equation (2.58)), but this time for integrable systems (Berry and Tabor [48,49]). The main difference is that periodic orbits are no longer isolated, so the sum is

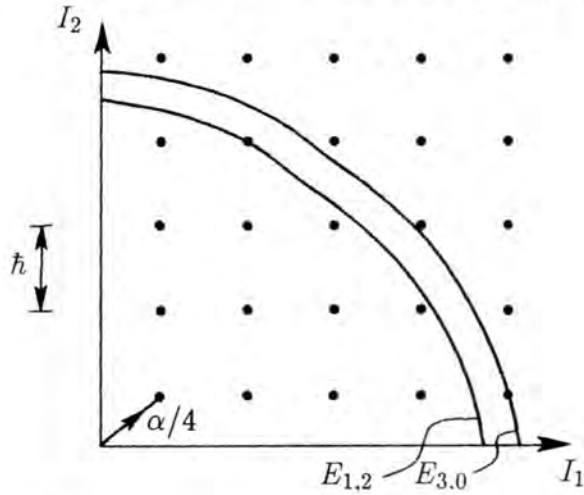


Figure 2.8.1. Quantum numbers in I -space, with two energy surfaces.

now over invariant tori instead. We start from the time-dependent propagator (equation (2.41)),

$$K(q'q''t) = \frac{1}{(2\pi i\hbar)^{\frac{N}{2}}} \sum_p |D_p|^{\frac{1}{2}} \exp \left\{ i \left(\frac{R_p}{\hbar} - \frac{\pi\mu_p}{2} \right) \right\}, \quad (2.65)$$

where we have written $t = t'' - t'$, $D_p = \det(-\partial^2 R_p / \partial q'' \partial q')$. The label p runs through all classical trajectories from q' to q'' . In angle-action variables D_p can be written

$$D_p = \det \left(\frac{\partial \theta''}{\partial I'_p} \right)^{-1}. \quad (2.66)$$

But $\theta'' - \theta' = \omega(I_p)t$, hence

$$D_p = \det \left(\frac{\partial \omega_i}{\partial I_{p,j}} t \right)^{-1} = t^{-N} [\det(\partial \omega_i / \partial I_{p,j})]^{-1}. \quad (2.67)$$

Also

$$R_p = I_p \cdot (\theta'' - \theta') - H(I_p)t. \quad (2.68)$$

Now the density of states, $\rho(E) \equiv \sum \delta(E - E_p)$, is

$$\rho(E) = \text{Re} \frac{1}{\pi\hbar} \int_0^\infty dt e^{iEt/\hbar} \int d^N q [K(q'q''t)]_{q'=q''=q}. \quad (2.69)$$

The requirement that $q'' = q' = q$ means, in angle-action variables, that $\theta'' - \theta' =$

$2\pi m$ for the torus I_m . Hence

$$\begin{aligned} \int d^N q [K(q'q''t)]_{q'=q''=q} &= \sum_m \int_0^{2\pi} d^N \theta \frac{1}{(2\pi i \hbar)^{\frac{N}{2}}} |D_m|^{\frac{1}{2}} \exp \left\{ i \left(\frac{R_m}{\hbar} - \frac{\pi \alpha_m}{2} \right) \right\} \\ &= \frac{(2\pi)^N}{(2\pi i \hbar)^{\frac{N}{2}}} \sum_{m \geq 0} \frac{\exp \left\{ i \left(\frac{R_m}{\hbar} - \frac{\pi \alpha_m}{2} \right) \right\}}{t^{\frac{N}{2}} |\det(\partial \omega_i / \partial I_{m_j})|^{\frac{1}{2}}}, \end{aligned} \quad (2.70)$$

where $R_m = 2\pi I_m \cdot m - H(I_m)t$. For the t integral, we can use the stationary phase method, which gives $H(I_m) = E$ and hence the period T_m of the torus. The amplitude factor is given by

$$\frac{\partial^2}{\partial t^2} (\text{phase}) = -\omega(I_m) \cdot \frac{\partial I_m}{\partial t} (2\pi i \hbar)^{\frac{1}{2}}. \quad (2.71)$$

Hence

$$\begin{aligned} \rho(E) &= \frac{1}{\pi \hbar} \operatorname{Re} \sum_{m \geq 0} \frac{(2\pi)^N}{(2\pi i \hbar)^{(N-1)/2}} \frac{\exp \left\{ i 2\pi m \cdot \left(\frac{I_m}{\hbar} - \frac{\alpha_m}{4} \right) \right\}}{T_m^{\frac{N}{2}} |\det(\partial \omega_i / \partial I_{m_j})|^{\frac{1}{2}} (-\omega_m \cdot \partial I_m / \partial t)^{\frac{1}{2}}} \\ &= \rho_0(E) + \frac{2}{\hbar^{(N+1)/2}} \operatorname{Re} \sum_{\substack{m \neq 0 \\ m > 0}} A_m \exp \left\{ i 2\pi m \cdot \left(\frac{I_m}{\hbar} - \frac{\alpha_m}{4} \right) \right\} \end{aligned} \quad (2.72)$$

where

$$A_m^2 = \frac{(2\pi)^{N-1}}{i^{N+1} T_m^N |\det(\partial \omega_i / \partial I_{m_j})| (\omega(I_m) \cdot \partial I_m / \partial t)}. \quad (2.73)$$

2.9 The Asymptotic Level Density for Stationary Billiards

We return now to the level density $\rho(E)$ defined by

$$\rho(E) = \sum_j \delta(E - E_j). \quad (2.74)$$

This was mentioned briefly in section (2.7), and is related to $g(E)$ by

$$\rho(E) = -\frac{\operatorname{Im}}{\pi} g(E). \quad (2.75)$$

This must be evaluated carefully, because of the poles along the real axis. It is conventional to take the contour below the real axis, by adding a small imaginary part to E .

We will be interested in statistical fluctuation properties of energy levels in section (2.10), but here we discuss the average behaviour of levels. As with $g(E)$ we can treat $\rho(E)$ as consisting of average terms contained in $\rho_0(E)$ and oscillatory terms $\rho_{\text{osc}}(E)$:

$$\rho(E) = \rho_0(E) + \rho_{\text{osc}}(E). \quad (2.76)$$

The calculation of ρ_{osc} is just the same as $g_{\text{osc}}(E)$ given in section (2.7). Here we will review some calculations of the asymptotic mean level density $\rho_0(E)$ for stationary billiards. The original results in physics are due mainly to Balian and Bloch , but there are also many results from mathematicians; a definite review is given by Baltes and Hilf [53] , and other sources are Berry [24] and Bohigas and Giannoni [25]. The two approaches we adopt are the heat kernel method and the time-independent Green function formulation.

Using the second approach, and the Green function defined by equation (2.42) we find

$$\begin{aligned} \rho_0(E) &= -\frac{1}{\pi} \lim_{\varepsilon \rightarrow 0} \int d^N q [G(q'q''E + i\varepsilon) - G(q'q''E - i\varepsilon)]_{q'=q''=q} \\ &= -\frac{\text{Im}}{\pi} \int d^N q [G(q'q''E)]_{q'=q''=q} \\ &= -\frac{\text{Im}}{\pi} g_0(E). \end{aligned} \quad (2.77)$$

Here the $q' = q'' = q$ constraint is only for zero length periodic orbits. The commutation of the Im operator with the \int operator must be done carefully, and usually a convergence factor is introduced which we have not written for sake of clarity.

The first result is for the level density inside a box, with infinite potential walls, but with no potential inside the box—a stationary quantum billiard. We approximate $G(q'q''E)$ as simply the free particle Green function inside the box, and zero outside. For $q' \approx q''$ this is

$$G(q'q''E) \approx -\frac{2im}{(2\hbar)^{\frac{N}{2}+1}} \left(\frac{p(q)}{|q'' - q'|} \right)^{\frac{N}{2}-1} H_{\frac{N}{2}-1}^{(1)}(p(q)|q'' - q'|/\hbar) \quad (2.78)$$

where $H_{\frac{N}{2}-1}^{(1)}(x)$ is the Hankel function (Abramowitz and Stegun [54]). Then

$\rho_0(E)$ is

$$\rho_0(E) \sim \frac{1}{h^N} \int d^N p d^N q \delta(E - H(p, q)) \equiv \frac{1}{h^N} \frac{dV(E)}{dE} \quad (2.79)$$

where $V(E)$ is the volume of phase space contained within the surface $H(p, q) = E$. Equation (2.79) is simply the Weyl formula that each mode takes up a volume h^N in phase space.

This can also be calculated from the heat kernel defined by

$$\begin{aligned} \left(\hat{H} - \frac{\partial}{\partial t} \right) K_H(q' q'' t) &= 0, \quad t > 0 \\ K_H(q' q'' 0) &= \delta(q'' - q'), \end{aligned} \quad (2.80)$$

whose solution in terms of eigenfunctions $\phi_i(q)$ is

$$K_H(q' q'' t) = \sum_j \phi_j(q'') e^{-E_j t} \phi_j^*(q') \quad (2.81)$$

and whose partition function is given by

$$\Phi(t) = \int_{q'=q''=q} d^N q K_H(q' q'' t) = \sum_j e^{-E_j t} = \int_0^\infty dE e^{-Et} \rho_0(E). \quad (2.82)$$

So the inverse Laplace transform is $\rho_0(E)$. If we approximate $K_H(q' q'' t)$ as free diffusion within the box so

$$K_H(q' q'' t) = \left(\frac{m}{2\pi\hbar t} \right)^{\frac{N}{2}} \exp \left\{ -m(q'' - q')^2 / 2\hbar t \right\}, \quad (2.83)$$

then

$$\Phi_0(E) = \left(\frac{m}{2\pi\hbar^2} \right)^{\frac{N}{2}} \frac{V_q}{t^{\frac{N}{2}}}, \quad (2.84)$$

giving

$$\rho_0(E) = \frac{1}{\hbar} \mathcal{L}^{-1} \left[e^{-Et/\hbar} \Phi_0(t) \right] = \left(\frac{m}{2\pi\hbar^2} \right)^{\frac{N}{2}} \frac{V_q}{\Gamma(\frac{N}{2})} E^{\frac{N}{2}-1}, \quad (2.85)$$

where V_q is the q -space volume contained in the billiard, related to $V(E)$ by

$$V(E) = \left(\frac{mE}{2\pi\hbar^2} \right)^{\frac{N}{2}} \frac{V_q}{\Gamma(\frac{N}{2} + 1)}. \quad (2.86)$$

Thus we arrive at exactly the same answer for $\rho_0(E)$ as equation (2.79). However, the Green function or heat kernel is not well approximated by the above formulae

when q' is close to the boundary; the first contribution due to this depends on the surface area of the boundary. The simplest method uses the heat kernel. By the method of images,

$$K_H(q'q''t) \approx K_0(q'q''t) - K_0(q'_1q''t) \quad (2.87)$$

where q'_1 is the image of q' in a plane P tangent to the surface \mathcal{S} (figure (2.9.1)).

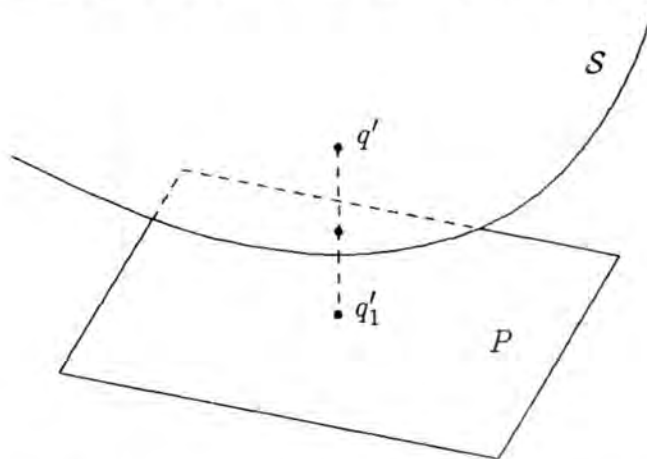


Figure 2.9.1. Image of a point q' in the tangent plane P to \mathcal{S} .

Suppose $d\sigma$ is a surface element, and z is the distance of q'' to the nearest tangent plane. Then the correction to $\Phi(t)$ is

$$\begin{aligned} - \int_{q'=q''=q} d^N q K_0(q'_1 q'' t) &= \left(\frac{m}{2\pi\hbar t} \right)^{\frac{N}{2}} \int_{\mathcal{S}} d\sigma \int_0^\infty dz \exp\{-2mz^2/\hbar t\} \\ &= -\frac{1}{4} \left(\frac{m}{2\pi\hbar t} \right)^{\frac{N}{2}-\frac{1}{2}} S_q, \end{aligned} \quad (2.88)$$

where S_q is the surface area of \mathcal{S} . The inverse Laplace transform, which is the surface contribution to $\rho_0(E)$, is

$$-\frac{1}{4} \left(\frac{m}{2\pi\hbar^2} \right)^{\frac{N}{2}-\frac{1}{2}} \frac{E^{\frac{N}{2}-\frac{3}{2}}}{\Gamma(\frac{N-1}{2})} S_q. \quad (2.89)$$

The Green function method can also be used to obtain this result, and also the next term which depends on the curvature and corners of the boundary.

In two dimensions, the volume term (2.85) and surface term (2.89) contributions give

$$\rho_0(E) \approx \frac{m\mathcal{A}}{2\pi\hbar^2} - \frac{1}{8\pi} \left(\frac{2m}{\hbar^2} \right)^{\frac{1}{2}} \mathcal{L} E^{-\frac{1}{2}}. \quad (2.90)$$

So the asymptotic number of modes is

$$\begin{aligned} \mathcal{N}_0(E) &\approx \frac{m\mathcal{A}E}{2\pi\hbar^2} - \frac{1}{4\pi} \left(\frac{2m}{\hbar^2} \right)^{\frac{1}{2}} \mathcal{L} E^{\frac{1}{2}}, \\ &\approx \frac{\mathcal{A}k^2}{4\pi} - \frac{\mathcal{L}k}{4\pi}, \end{aligned} \quad (2.91)$$

where

$$k = \frac{\sqrt{2mE}}{\hbar} \quad \text{and} \quad \mathcal{A} \equiv V_q, \quad \mathcal{L} \equiv S_q. \quad (2.92)$$

These are the first two terms in an asymptotic expansion. The next term is a constant due to the curvature κ of the boundary and its corners of internal angle β_i (Balte and Hilf [53]):

$$\sum_i \int_{\mathcal{L}_i} \frac{\kappa(s) ds}{12\pi} + \sum_i \left(\frac{\pi}{\beta_i} - \frac{\beta_i}{\pi} \right) \Big/ 24. \quad (2.93)$$

where s is the arc length along the boundary, i runs over all the corners, and \mathcal{L}_i are the piece-wise smooth sections of boundary.

In a later chapter, the case of a billiard in a scalar and vector potential will be considered, and we will derive the area and perimeter terms, but not the curvature term. As the curvature term is a constant, this can be estimated numerically.

2.10 Spectral Fluctuation Properties

In this section, the theory of random matrices as applied to classically chaotic systems will be reviewed. Mention shall be made of deviations from this theory and their connection to the periodic orbits of the classical system.

Random matrix theory was devised in the 1950's and 1960's by several nuclear physicists including C.E. Porter, E.P. Wigner, M.L. Mehta and F.J. Dyson. A useful collection of original papers is [26] and a recent review is [55]. It is used to describe the high energy levels of complex nuclei where the levels are so close that it is impractical to consider individual levels and one becomes interested in only the statistical properties of the spectrum. Their theory shows that one may regard these levels as eigenvalues of a random matrix chosen from an ensemble of matrices, invariant under certain symmetry transformations.

One way of understanding how this applies to non-integrable systems is to consider the simplest case of a two by two Hermitian matrix. Suppose that the system depends on a parameter α and consider the Hamiltonian $\hat{H}(\alpha + \delta\alpha)$ close to $\hat{H}(\alpha)$ where two eigenfunctions ϕ_1 and ϕ_2 have almost the same energies E_1^0 and E_2^0 . Since $\hat{H}(\alpha + \delta\alpha)$ is a small perturbation of $\hat{H}(\alpha)$ we can approximate the eigenfunctions of $\hat{H}(\alpha + \delta\alpha)$ by

$$\psi = a\phi_1 + b\phi_2. \quad (2.94)$$

Now approximating $\hat{H}(\alpha + \delta\alpha) \approx \hat{H}(\alpha) + \hat{V}(\alpha)$, the new levels are the solution of

$$\begin{vmatrix} E_0 + V_{11} - E & V_{12} \\ V_{12}^* & E_0 + V_{22} - E \end{vmatrix} = 0, \quad (2.95)$$

where $V_{ij} = \langle \phi_i | V | \phi_j \rangle$. This gives

$$E_{1,2} = E_0 + \frac{1}{2}(V_{11} + V_{22}) \pm \frac{1}{2}\sqrt{(V_{11} - V_{22})^2 + 4|V_{12}|^2}. \quad (2.96)$$

Thus the squared difference in energy levels is a sum of squares:

$$(\Delta E)^2 = (V_{11} - V_{22})^2 + 4|V_{12}|^2. \quad (2.97)$$

For degeneracy, we require $V_{11} = V_{22}$, $V_{12} = 0$. If \hat{H} is complex Hermitian then V_{12} is complex and so these are three conditions in real variables. If \hat{H} is real symmetric two conditions are required. One may think of \hat{H} as inhabiting a two- or three-dimensional parameter space for real symmetric, complex Hermitian

matrices respectively, with a degeneracy in energy at *one* point in this space. This is the tip of a double cone, with the levels $E_{1,2}$ lying on the double cone for all other values of the parameters. However \hat{H} depends on only one parameter, α . Thus as we vary this parameter we will in general miss this degeneracy, and the slice through the double cone will show levels which ‘repel’ each other before getting too close.

If one assumes that the two state analysis above is valid, so that the spectrum is dominated by avoided crossings, then one may derive the probability distribution $P(H)dH$ that H is taken from within a volume element dH of an ensemble of random matrices (we have dropped the hat convention here for convenience). Suppose that the ensemble is invariant under a transformation, $H' = W^\dagger HW$, then requiring $P(H')dH' = P(H)dH$ gives the form of $P(H)$. For Gaussian orthogonal ensembles (GOE), where W is an orthogonal matrix, it can be shown that (see review by Eckhardt [55]),

$$P(H) = 2^{-\frac{N}{2}}(\gamma/2\pi)^{N(N+1)/4} \exp(-\text{Tr } H^2/4\gamma) \quad (2.98)$$

where γ is a constant. For Gaussian unitary ensembles (GUE), where W is unitary, it can be shown that

$$P(H) = 2^{-\frac{N}{2}}(\gamma/2\pi)^{N^2/2} \exp(-\text{Tr } H^2/4\gamma). \quad (2.99)$$

For the spacing distribution, we will consider just the case when H is real symmetric, and two by two:

$$H = \begin{pmatrix} A & B \\ C & D \end{pmatrix}. \quad (2.100)$$

We define new variables E_\pm and the angle ϕ which make H diagonal:

$$\begin{aligned} A &= E_+ \cos^2 \phi + E_- \sin^2 \phi \\ B &= (E_+ - E_-) \cos \phi \sin \phi \\ C &= E_+ \sin^2 \phi + E_- \cos^2 \phi, \end{aligned} \quad (2.101)$$

with Jacobian,

$$\frac{\partial(A, B, C)}{\partial(E_+, E_-, \phi)} = E_+ - E_-.$$
 (2.102)

Thus writing $P(H) = P(A, B, C)$ we find

$$P(E_+, E_-, \phi) = (E_+ - E_-)P(A, B, C),$$
 (2.103)

where substitutions of E_+, E_-, ϕ in A, B, C are implicitly understood. The spacing distribution $P(S)$, which is defined as the probability $P(S) dS$ of finding eigenvalues such that $S_i = E_{i+1} - E_i$ is in the interval S to $S + dS$, is then

$$\begin{aligned} P(S) &= \iiint dE_+ dE_- d\phi \delta(S - (E_+ - E_-)) P(E_+, E_-, \phi) \\ &= S \iiint dE_+ dE_- d\phi \delta(S - (E_+ - E_-)) P(A, B, C). \end{aligned}$$
 (2.104)

Substituting in equation (2.99) with $N = 2$, we obtain

$$P(S) = (\gamma/4)S \exp\{-(\gamma/8)S^2\}.$$
 (2.105)

Normalisation of this gives $\gamma = 2\pi$. So for GOE we have

$$P(S) = \frac{\pi}{2}S \exp(-\pi S^2/4).$$
 (2.106)

This result generalises for N -dimensional matrices if one assumes that there are only pair couplings, and that higher order couplings can be neglected—In other words, that we do not see more than two levels come close together.

Similarly, it can be shown that for complex Hermitian matrices, satisfying GUE statistics,

$$P(S) = \frac{32}{\pi^2}S^2 \exp\left(-\frac{4}{\pi}S^2\right).$$
 (2.107)

It would be interesting to consider the distribution $P(S)$ when the system is integrable. We can find $P(S)$ by considering the probability $g(y) dy$ of finding a

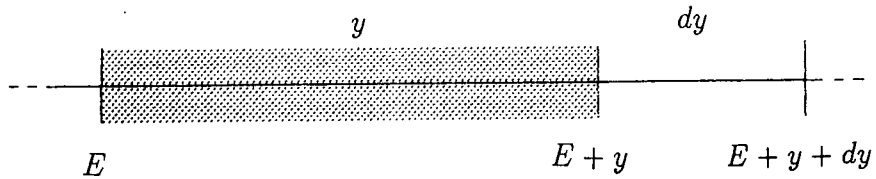


Figure 2.10.1.

level in the interval $E + y$ to $E + y + dy$ given that there is a level at E (figure (2.10.1)).

Then

$$\begin{aligned} P(S) dS &= (\text{prob. of level in } [E + y, E + y + dy]) \times (\text{prob. not in } [E, E + y]) \\ &= dS g(S) \left[1 - \int_0^S P(x) dx \right]. \end{aligned} \tag{2.108}$$

So

$$P(S) = g(S) \int_S^\infty P(x) dx. \tag{2.109}$$

This can be solved for $P(S)$ to give

$$P(S) = g(S) \exp \left(- \int_0^S g(x) dx \right). \tag{2.110}$$

Thus for GOE, $g(S) = \frac{\pi}{2}S$. Coming back to integrable systems, we can easily see that the energy levels do not repel each other. Suppose $I_{m_1} = (m_1 + \alpha_1/4)\hbar$, $I_{m_2} = (m_2 + \alpha_2/4)\hbar$ label two nearby tori, then the energy levels are approximately degenerate if

$$\begin{aligned} E_{m_1} - E_{m_2} &\approx H(I_{m_1}) - H(I_{m_2}) \\ &\approx \hbar(m_1 - m_2) \cdot \nabla_I H((I_{m_1} + I_{m_2})/2) = 0. \end{aligned} \tag{2.111}$$

But $\nabla_I H$ are the frequencies ω . Hence this is the condition of resonance, which is very common for integrable systems. Hence we expect energy levels to be independent of each other. If they are random variables, we expect this to be

expressed by $g(y) = 1$. This gives a Poisson process for the level spacing with

$$P(S) = e^{-S}. \quad (2.112)$$

This intuitive argument that $g(y) = 1$ has been properly proved for generic integrable systems by Berry and Tabor [47] by considering the periodic sum formula for the density fluctuations. They showed that for sufficiently small spacings, the sum is dominated by the long orbits $T_m > \Delta E/2\pi\hbar$ and these have the universal property that

$$\left\langle \sum_m A_m^2 \delta(T - T_m) \right\rangle \rightarrow \frac{dV/dE}{(2\pi)^{N+1}}, \quad (2.113)$$

where $\langle \dots \rangle$ denotes average over the energy range within ΔE , and A_m^2 is the intensity of the m^{th} torus given by equation (2.73) and T_m is its period. It can then be shown that $g(y) = 1$. There are however exceptions to this, the most notable being the case of a set of harmonic oscillators. These show level repulsion, both theoretically and computationally.

A similar universality property to equation (2.113) occurs for completely chaotic systems. Refer to the semiclassical trace formula of Gutzwiller (equation (2.58)). The factor $F(1)$ is approximately $\exp(h_{KS}T)$ for long orbits of period T . Hence the amplitude of an orbit j is $A_j \sim T \exp(-\frac{1}{2}h_{KS}T)$. This can be combined with the exponential growth law of the number density $\rho(T)$ of orbits of period T [56] ,

$$\rho(T) \sim \exp(h_{KS}T)/T \quad T \gg 0. \quad (2.114)$$

to give the Hannay-Ozorio de Almeida classical sum rule [57] :

$$\left\langle \sum_j A_j^2 \delta(T - T_j) \right\rangle \rightarrow \frac{T}{4\pi^2} \quad T \gg 0. \quad (2.115)$$

The universality of this rule is due to the fact that for a chaotic system the time-averaged exponential divergence of trajectories is the space-averaged divergence

(i.e. that h_{KS} is the same for all points in phase space). This implies that for long orbits this classical sum rule does not depend on the particular dynamics of the system. Unfortunately, it is not as easy to find the level statistics from the Gutzwiller trace formula, as it was for integrable systems. However, the universality of (2.115) does lead us to expect random matrix theory to be applicable to chaotic systems, and indeed this has been seen numerically to be the case in many systems.

For level spacing statistics the energy spacings are always small enough for the universality to hold. But it would be interesting to study statistical properties where this law is no longer valid. We would then be able to see how the particular dynamics of short orbits affects the statistical properties. This would be seen as a deviation from random matrix theory. A long energy range statistic that is particularly suitable is the Dyson $\Delta(L)$ statistic [58], a two-point correlation function defined as the local average of the mean square deviation of the staircase $\mathcal{N}(E)$ from the best fitting straight line over an energy range corresponding to L mean level spacings:

$$\begin{aligned} \Delta(L) &\equiv \left\langle \min_{A,B} \frac{\langle \rho(E) \rangle}{L} \int_{-L/2\langle \rho \rangle}^{L/2\langle \rho \rangle} dx [\mathcal{N}(E+x) - A - Bx]^2 \right\rangle \\ &= \left\langle \frac{\langle \rho \rangle}{L} \int_{-L/2\langle \rho \rangle}^{L/2\langle \rho \rangle} dx \mathcal{N}^2(E+x) - \left[\frac{\langle \rho \rangle}{L} \int_{-L/2\langle \rho \rangle}^{L/2\langle \rho \rangle} dx \mathcal{N}(E+x) \right]^2 \right. \\ &\quad \left. - 12 \left[\frac{\langle \rho \rangle^2}{L^2} \int_{-L/2\langle \rho \rangle}^{L/2\langle \rho \rangle} dx x \mathcal{N}(E+x) \right]^2 \right\rangle. \end{aligned} \quad (2.116)$$

The theory of spectral rigidity of chaotic and integrable systems below is due to Berry [59]. For $L \ll 1$, the limit $\Delta(L) \rightarrow L/15$ is independent of the particular distribution of the levels. For L in a range greater than the mean spacing, but still semiclassical, one can use the Gutzwiller trace formula. For chaotic systems

$$\rho(E) = \rho_0 + \operatorname{Re} \frac{1}{\pi\hbar} \sum_j \frac{T_j}{F_J^{\frac{1}{2}}(1)} \exp \{i(S_j/\hbar - \pi\alpha_j/2)\}, \quad (2.117)$$

where j labels all periodic orbits, multiple, positive and negative (not zero) as

well as primitive ones. And for integrable systems it is

$$\rho(E) = \rho_0 + 2\operatorname{Re} \sum_{m \neq 0} A_m \exp \{i 2\pi m.(I_m/\hbar - \alpha_m/4)\}, \quad (2.118)$$

where A_m is given by equation (2.73).

One may write these as

$$\rho(E) = \rho_0(E) + \frac{\operatorname{Re}}{\hbar^{\mu+1}} \sum_j A_j \exp \{i(S_j/\hbar - \pi\alpha_j/2)\}, \quad (2.119)$$

where

$$A_j = \begin{cases} \frac{T_j}{\pi F_j^{\frac{1}{2}}(1)}, & \mu = 0 \\ A_m, & \mu = \frac{1}{2}(N-1) \end{cases} \quad \begin{array}{l} \text{for chaotic systems;} \\ \text{for integrable systems.} \end{array}$$

Integrating equation (2.119) gives

$$\mathcal{N}(E) = \mathcal{N}_0(E) + \operatorname{Re} \frac{-i}{\hbar^\mu} \sum_j \frac{A_j}{T_j} \exp \{i(S_j/\hbar - \pi\alpha_j/2)\}. \quad (2.120)$$

If one approximates $S_j(E+x) \approx S_j(E) + xT_j(E)$, then substitutes for $\mathcal{N}(E)$ into equation (2.116), one obtains

$$\begin{aligned} \Delta(L) = & \left\langle \frac{1}{\hbar^{2\mu}} \sum_i \sum_j \frac{A_i A_j}{T_i T_j} \exp \left\{i \frac{\pi}{2}(\mu_j - \mu_i)\right\} \exp \left\{i(S_i - S_j)/\hbar\right\} \right. \\ & \times \left. \left[F(y_i - y_j) - F(y_i)F(y_j) - 3F'(y_i)F'(y_j) \right] \right\rangle, \end{aligned} \quad (2.121)$$

where $F(y) = \sin y/y$, $y_j = LT_j/2\hbar\rho_0$.

(i) *Integrable systems.*

Consider the long orbit approximation $L \ll L_{\max}$ where $L_{\max} = \hbar\rho_0/T_{\min} \sim \hbar^{-(N-1)}$, where T_{\min} is for the shortest periodic orbit. For integrable systems, $|y_i - y_j|$ is very small for these orbits, so we can write

$$\Delta(L) = \frac{2}{\hbar^{2\mu}} \int_0^\infty \frac{dT}{T^2} \phi(T) G(LT/2\hbar\rho_0), \quad (2.122)$$

where

$$G(y) = 1 - [F(y)]^2 - 3 [F'(y)]^2$$

$$\phi(T) = \left\langle \sum_i \sum_{\substack{j \\ T_i > 0 \\ T_j > 0}} A_i A_j \cos \{(S_i - S_j)/\hbar\} \delta \left(T - \frac{1}{2}(T_i + T_j) \right) \right\rangle. \quad (2.123)$$

It can be shown that $\phi(T)$ is dominated by the diagonal term in this case and using equation (2.113), one obtains

$$\Delta(L) = \frac{2}{\hbar^{2\mu}} \frac{dV/dE}{(2\pi)^{N+1}} \int_0^\infty \frac{dT}{T^2} G(y)$$

$$= \frac{L}{2\pi} \int_0^\infty \frac{dy}{y^2} G(y). \quad (2.124)$$

The integral is simple but laborious, and yields the value $2\pi/15$, giving

$$\Delta(L) = \frac{1}{15} L. \quad (2.125)$$

This is the universal regime of $L \ll L_{\max}$, and is also the result that would be obtained from random matrix theory. For $L \gg L_{\max}$, $G(y) \approx 1$ so

$$\Delta(L) = \frac{2}{\hbar N - 1} \sum_{m>0} \frac{A_m^2}{T_m^2} = \text{const.} \quad (2.126)$$

Thus the spectral rigidity saturates above $L = L_{\max}$, and is linearly dependent on L for $L \ll L_{\max}$. For $L \sim L_{\max}$, small oscillations in $G(y)$ give a slightly oscillatory $\Delta(L)$.

(ii) Chaotic Systems.

Here for $L \ll L_{\max}$, the diagonal approximation is again valid and using (2.115), we obtain

$$\phi(T) \rightarrow \begin{cases} T/4\pi^2, & \text{for } T_{\max} \gg T \gg T_{\min}; \\ \rho_0\hbar/2\pi, & \text{for } T \gg T_{\max}, \end{cases} \quad (2.127)$$

where $T_{\max} = 2\pi\hbar\rho_0 = \frac{dV/dE}{\hbar^{N-1}}$ (equation (2.61)). Thus $\Delta(L)$ can be calculated using the simplest approximation for $\phi(T)$, namely

$$\phi(T) \rightarrow \begin{cases} T/4\pi^2, & \text{for } T \leq T_{\max}; \\ \rho_0\hbar/2\pi, & \text{for } T \geq T_{\max}. \end{cases} \quad (2.128)$$

Then $\Delta(L)$ is simply

$$\begin{aligned} \Delta(L) &= \frac{1}{2\pi^2} \int_0^{T_{\max}} \frac{dT}{T} G(y) + \frac{\rho_0\hbar}{\pi} \int_{T_{\max}}^{\infty} \frac{dT}{T^2} \\ &= \frac{1}{2\pi^2} \int_0^{\pi L} \frac{dy}{y} G(y) + \frac{L}{2\pi} \int_{\pi L}^{\infty} \frac{dy}{y^2} \\ &= \frac{1}{2\pi^2} \left\{ \log(2\pi L) + \gamma_E - \frac{5}{4} \right\}, \end{aligned} \quad (2.129)$$

where γ_E is the Euler constant 0.577.... This is exactly the form given by random matrix theory for GUE. For time-reversal systems, formula (2.127) is not valid. The reason is that there is coherence between time-reversed orbits, so that the amplitude of $\phi(T)$ is twice as large for $T_{\max} \gg T \gg T_{\min}$. So the correct interpolation (which is not linear) gives

$$\Delta(L) = \frac{1}{\pi^2} \left[\log(2\pi L) + \gamma_E - \frac{5}{4} - \frac{1}{8}\pi^2 \right]. \quad (2.130)$$

This agrees with the formula given by random matrix theory for GOE.

When $L \gg L_{\max}$, the universality of (2.115) breaks down—short orbits become important. We have

$$\Delta(L) = 2 \int_0^{\infty} \frac{dT}{T^2} \phi(T) \quad \text{for } L \gg L_{\max}. \quad (2.131)$$

Thus we can split the integral into two parts, a non-universal part for $0 < T \ll T_{\min}$, and a universal part for $T \gg T_{\min}$. The universal part gives a saturation

constant:

$$\Delta(L) \approx \frac{1}{2\pi^2} [\log(L_{\max}) + 1]. \quad (2.132)$$

And the non-universal part gives oscillatory terms to $\Delta(L)$, which must be calculated for each system. For time-reversal systems this constant should be replaced by

$$\Delta(L) \approx \frac{1}{\pi^2} [\log(L_{\max}) + 1 - \frac{1}{8}\pi^2]. \quad (2.133)$$

Thus for chaotic systems, the saturation value of $\Delta(L)$ is approximately \hbar^{N-1} larger than for integrable systems, reflecting the fact that spectral fluctuations are much weaker, and the spectrum more rigid. Note that here saturation again indicates deviation from random matrix theory.

3. Classical Billiards in a Rotating Boundary

3.1 Introduction

A classical particle with mass m moves freely in a plane region which is bounded by a perfectly reflecting smooth closed curve, rotating uniformly about a fixed axis perpendicular to the plane. Between bounces the particle will travel in a straight line at constant velocity, but it will lose or gain momentum instantaneously on reflection. Thus the energy of the particle is not conserved, and so we might not expect to find a conserved Hamiltonian. However, when the standard transformation is made to a frame rotating at the same angular speed ω as the boundary, it becomes clear that a suitable Hamiltonian can be constructed.

It is convenient to parametrise the (x, y) co-ordinates of the particle in this frame by the complex variable $z = x + iy$. Then suppose that at time $t = 0$, the particle is at a point $z = a$ on the boundary, and that its velocity immediately after reflection is b (in the laboratory frame). Then its position in the rotating frame at time t is

$$z = (a + bt)e^{-i\omega t} \quad (3.1)$$

and its velocity is

$$\dot{z} = be^{-i\omega t} - i\omega z. \quad (3.2)$$

In particular, its initial velocity is $\dot{z}_0 = b - i\omega a$. Equation (3.2) gives the equation of motion,

$$\ddot{z} = -2i\omega\dot{z} + \omega^2 z. \quad (3.3)$$

It is easy to show either from this, or by transforming the free particle Hamiltonian $\frac{1}{2m}\mathbf{p}^2$ directly, that a Hamiltonian in the rotating frame can be constructed:

$$H = \frac{1}{2m}\mathbf{p}^2 + \omega(yp_x - xp_y) + U(x, y), \quad (3.4)$$

where $\mathbf{p} = (p_x, p_y)$ is the conjugate momentum, and U is the infinite potential

well,

$$U(x, y) = \begin{cases} 0 & \text{inside boundary} \\ \infty & \text{outside boundary.} \end{cases} \quad (3.5)$$

A word of explanation is required here. In the rotating frame the boundary appears stationary; thus the particle is specularly reflected in this frame, and so (3.5) is the correct equation to use for the potential. This means that H is conserved in the rotating frame even though the particle is gaining and losing momentum in the laboratory frame. So the rotating frame is the natural one in which to examine the problem.

The force from (3.3) consists of a Coriolis part, $-2im\omega\dot{z}$, and a centrifugal part $m\omega^2z$. This is equivalent to the force on a particle of charge q in the presence of a uniform magnetic field of strength $B = 2m\omega/q$ perpendicular to the plane region, and an electric field $E = m\omega^2z/q$. We can rewrite H to make this analogy more apparent:

$$H = \frac{1}{2m}(\mathbf{p} - q\mathbf{A})^2 - \frac{1}{2}m\omega^2\mathbf{r}^2 + U(\mathbf{r}), \quad (3.6)$$

where \mathbf{A} is the vector potential given by

$$B = \frac{\partial A_y}{\partial x} - \frac{\partial A_x}{\partial y}. \quad (3.7)$$

Equation (3.4) and (3.6) have to agree, so $\mathbf{A} = \frac{m\omega}{q}(-y, x)$ giving

$$H = \frac{1}{2m}(p_x + m\omega y)^2 + \frac{1}{2m}(p_y - m\omega x)^2 - \frac{1}{2}m\omega^2(x^2 + y^2) + U(x, y). \quad (3.8)$$

The conjugate momentum \mathbf{p} is not the true momentum $m\dot{\mathbf{r}}$, but is in fact

$$\mathbf{p} = m\dot{\mathbf{r}} + q\mathbf{A}, \quad (3.9)$$

so

$$H = \frac{1}{2}m\dot{\mathbf{r}}^2 - \frac{1}{2}m\omega^2\mathbf{r}^2 + U(\mathbf{r}). \quad (3.10)$$

In complex notation $p = m\dot{z} + im\omega z = mbe^{-i\omega t}$. Thus p is similar to the momentum in the laboratory frame. Hence $\frac{1}{2m}\mathbf{p}^2$ and $\omega(yp_x - xp_y)$ are independently

conserved between reflections, and correspond to conservation of linear and angular momentum in the laboratory frame. However they are not conserved on reflection, although their sum is.

It will be useful later to think of the 3-dimensional ‘surface’ of constant energy in 4-dimensional phase space. It is easier to use $m\mathbf{v} = m\dot{\mathbf{r}}$ rather than \mathbf{p} as the ‘momentum’. Then the surface of constant energy $E = H(\mathbf{p}, \mathbf{r})$ is the surface of a 4-dimensional hyperboloid (formed by rotating a two-dimensional hyperbola about one axis into the third dimension, and then about the second axis into the remaining dimension (figure (3.1.1)). The 4-volume contained below the energy surface and within the walls of the billiard will be used to calculate the density of states for the quantum problem, using the Weyl rule with corrections due to the boundary. Because H is not positive definite we need to investigate $E < 0$ as well as $E \geq 0$. $E < 0$ is interesting; the velocity reaches zero at a finite distance $\delta = \sqrt{-2E/m\omega^2}$ from the axis of rotation, and the disc $|\mathbf{r}| < \delta$ is classically forbidden. This can be seen in the pictures of trajectories within the billiard, where there exists a caustic boundary at $|\mathbf{r}| = \delta$. The energy surface is a hyperboloid whose foci lie on the plane $\mathbf{v} = 0$, and this surface is asymptotic to the conic surface $\mathbf{v}^2 = \omega^2 \mathbf{r}^2$. As E increases from its minimum value (*i.e.* when the forbidden region fills the whole billiard and δ is maximum), δ decreases and the energy surface becomes closer to the conic surface $\mathbf{v}^2 = \omega^2 \mathbf{r}^2$, until at $E = 0$ they join. For $E > 0$ the hyperboloid is inverted and has foci in the plane $\mathbf{r} = 0$, and the whole of the billiard is accessible. For $E < 0$ and for certain boundary shapes it is possible to have several classically disconnected regions of motion. This could be interesting quantum mechanically, with the possibility of quantum tunnelling between the regions.

3.2 The Rotating Circular Billiard

Possibly the simplest example of rotating billiards is the circular billiard table, rotating about a point on its edge. This was the first example to be studied, primarily because its boundary is C^∞ , and also because at zero rotation it is integrable; any non-integrability is due to the rotation. Suppose that the circle has radius ρ , and the equation of the boundary is $|\mathbf{r}| = \rho(1 + \cos\theta)$,

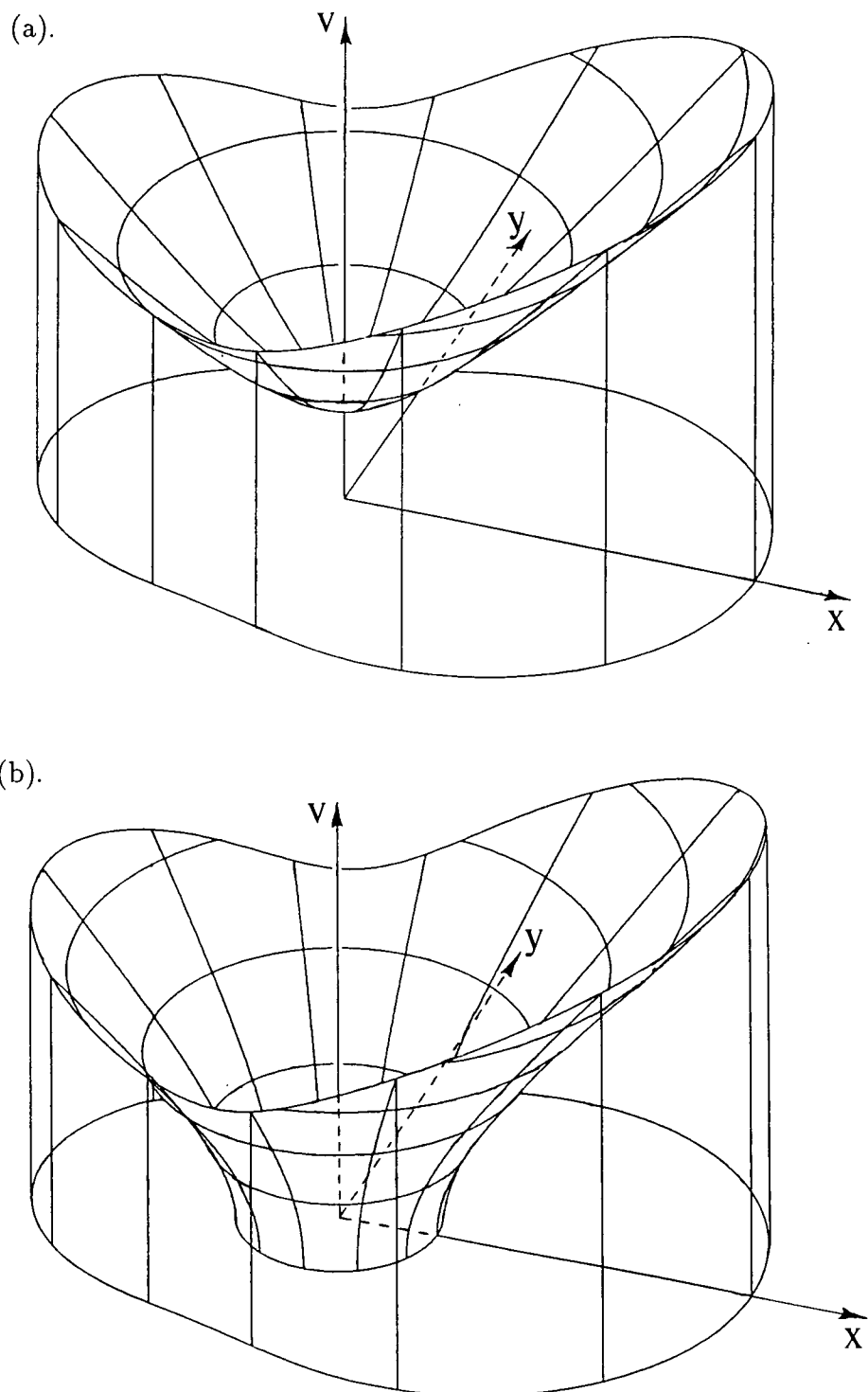


Figure 3.1.1. The energy surface $E = \text{const.}$ shown in three of the four dimensions of phase space x , y and $v = |\mathbf{v}|$, (a). for $E > 0$, (b). for $E < 0$.

where (r, θ) are polar co-ordinates from the centre of the circle, with the axis of rotation at $(r, \theta) = (1, \pi)$. We can rescale the problem using $z \mapsto z/\rho$, $t \mapsto \omega t$, $H \mapsto H/m\rho^2\omega^2$ to obtain dimensionless variables. We now see that the energy is the only parameter of the system; all changes in size of boundary, speed of rotation and masses of particle are equivalent to a change in energy with appropriate scaling. The rescaled Hamiltonian is

$$H = \frac{1}{2}\mathbf{v}^2 - \frac{1}{2}\mathbf{r}^2 + U(r). \quad (3.11)$$

This gives the equation of motion

$$z = (a + bt) \exp(-it), \quad (3.12)$$

with the boundary given by

$$z = 1 + e^{i\theta}. \quad (3.13)$$

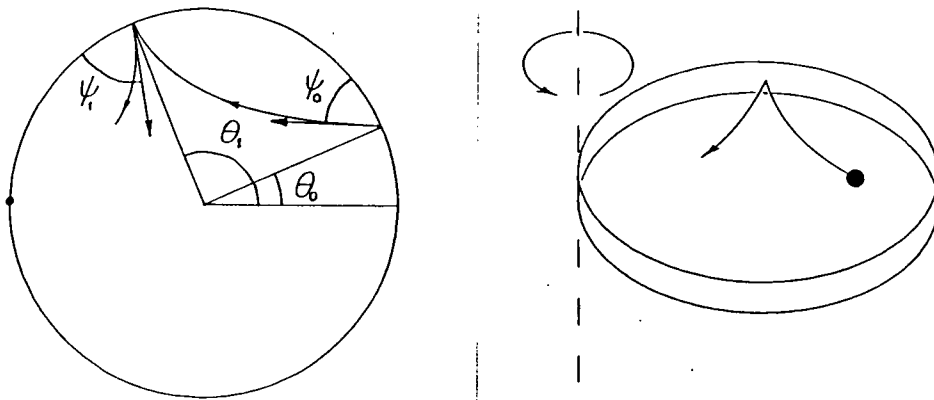


Figure 3.2.1. The phase co-ordinates (θ_i, ψ_i) of a typical trajectory in the rotating frame. Perspective view of the billiard.

The co-ordinates we use are defined in figure (3.2.1). Suppose that at $t = 0$ the particle is on the boundary at $\theta = \theta_0$ and is projected at a speed v and at an angle ψ_0 to the tangent of the circle (measured anti-clockwise). Then the particle is at a point $a = 1 + e^{i\theta_0}$ on the boundary, and has a velocity

$\dot{z}_0 = b - ia = iv e^{i(\theta_0 + \psi_0)}$. Thus its position at time t is

$$z(t) = \left[(1 + e^{i\theta_0})(1 + it) + iv t e^{i(\theta_0 + \psi_0)} \right] e^{-it}. \quad (3.14)$$

We can write the distance of the particle from the boundary as $d = 1 - |z - 1|$, so that it hits the boundary when d again becomes zero at $t = T$. The condition $d(t) = 0$ can be easily solved numerically, but we must be careful that the *shortest* T is found. A little thought will show that there is the possibility of one (and no more than one) minimum in $d(t)$ which may just go below zero, so that the root may be easily missed. The method we used to cope with this problem was to have a large step size $\Delta t = 0.1$ and find when the situation $d(t_i - \Delta t) > d(t_i) < d(t_i + \Delta t)$ occurs, which indicates a minimum, and then find this minimum exactly using a standard NAG routine. If the minimum is negative we can bracket the root between $(t_i - \Delta t, t_{min})$. Otherwise, we continue stepping t until $d(t_j) < 0$. We can then bracket the root between $(t_j - \Delta t, t_j)$. T must be less than 2π because this is the time for one complete revolution, and so $t_j < 2\pi$. This test checks any errors in the program. Having bracketed the root, we can then use a standard root-finding NAG routine to find T exactly. This method is likely to work for most trajectories. But for a trajectory in which a minimum and maximum both occur within a time span of $2\Delta t$, the first root may not be detected. This is however a very rare event.

The reflection condition $v'_{\perp} = -v_{\perp}$, $v'_{\parallel} = v_{\parallel}$ (where prime denotes quantity after reflection) has a particularly nice form using the complex notation:

$$\dot{z}' = -\bar{z}(z - 1)^2. \quad (3.15)$$

Figure (3.2.2) shows why this is so. From the diagram we find that

$$\dot{z} = iv e^{i(\theta - \psi)} = iv(z - 1)e^{-i\psi}, \quad (3.16)$$

$$\dot{z}' = iv e^{i(\theta + \psi)} = iv(z - 1)e^{i\psi}. \quad (3.17)$$

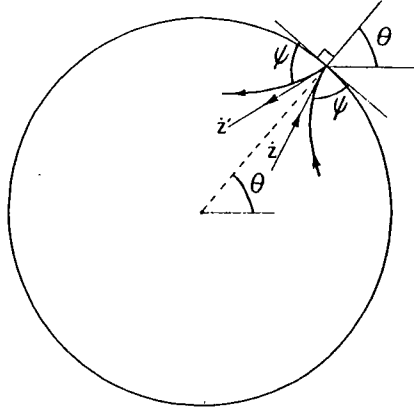


Figure 3.2.2. Specular reflection of the particle in the rotating frame.

Hence

$$\dot{\bar{z}} = -iv(\bar{z} - 1)e^{i\psi} = -iv(z - 1)^{-1}e^{i\psi}, \quad (3.18)$$

and so equation (3.15) follows.

Thus by numerically solving for T , and using the reflection condition, we can build up a series of bounce co-ordinates $(\theta_0, \psi_0), (\theta_1, \psi_1), \dots, (\theta_i, \psi_i), \dots$. Thus the bounce map has been implicitly defined.

It is interesting to study the angular momentum $L = (yp_x - xp_y)$, which is conserved between bounces but changes at reflection. Using complex notation, and equation (3.9) we can write

$$L = \text{Im}(z\bar{p}) = \text{Im}(z\dot{z}) - |z|^2. \quad (3.19)$$

Consider the first term:

$$\begin{aligned} \text{Im}(z\dot{z}) &= \text{Im}\left[\left(\frac{1}{\bar{z}-1} + 1\right)\dot{z}\right] \\ &= \text{Im}\left[(1-\bar{z})\dot{z}' + \dot{\bar{z}}\right] \\ &= \text{Im}(\dot{z}' + \dot{\bar{z}}) + \text{Im}(z\dot{\bar{z}}'). \end{aligned} \quad (3.20)$$

Hence the change in L at reflection is

$$\begin{aligned} \delta L &= L' - L = \text{Im}(z\dot{\bar{z}}' - z\dot{\bar{z}}) \\ &= -\text{Im}(\dot{z}' + \dot{\bar{z}}) \\ &= -v'_y + v_y, \end{aligned} \quad (3.21)$$

where v_y, v'_y are the y components of velocity in the rotating frame immediately before and after reflection, respectively. Because H is conserved, δL is balanced by an opposite but equal change in the linear momentum $\frac{1}{2}p^2$.

3.3 Periodic Cycles of the Rotating Circle

The fixed points and periodic cycles (p-cycles) of a Hamiltonian system reveal much about the dynamics of the system, and in particular the study of periodic cycles is relevant to the Gutzwiller trace formula [20], which relates these purely classical quantities to quantum mechanical quantities through a sum rule. In dissipative one-dimensional systems the bifurcation of periodic cycles by period doubling is well understood. In contrast, bifurcations in two-dimensional Hamiltonian systems are much richer and varied and are still not completely understood.

Consider the map

$$(\theta_{i+1}, \psi_{i+1}) = \mathbf{F}(\theta_i, \psi_i). \quad (3.22)$$

Then we define the set of points (θ_i, ψ_i) , for $i = 1, \dots, p$ which satisfy

$$\mathbf{F}^p(\theta_i, \psi_i) = (\theta_i, \psi_i) \quad (3.23)$$

to be an p-cycle of the map, and in particular the case $p = 1$ is a fixed point. A little thought using the symmetry of the circular billiard will show that there can be at most one fixed point and this must occur at $\theta = 0$.

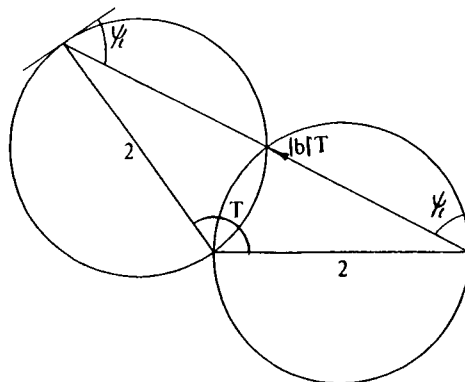


Figure 3.3.1. The fixed point viewed in the laboratory frame.

In the laboratory frame (see figure (3.3.1)), we have

$$2 \sin\left(\frac{T}{2}\right) = \frac{1}{2}|b|T, \quad (3.24)$$

where T is the time between bounces. Also, the angle of projection ψ_l in the laboratory frame (as defined in figure (3.3.1)) is simply

$$\psi_l = \frac{1}{2}T. \quad (3.25)$$

The angle ψ_l can also be expressed in terms of the angle and speed of projection in the rotating frame. Using $b = ivt e^{i\psi_l} = i(2 + ve^{i\psi})$ we find

$$\tan \psi_l = \frac{v \sin \psi}{v \cos \psi + 2}. \quad (3.26)$$

We can express T similarly using the equation of motion

$$z(t) = [2(1 + it) + ivte^{i\psi}] e^{-it}. \quad (3.27)$$

At $t = T$, the particle returns to its original position $z(T) = 2$, so taking the modulus of (3.27) gives

$$4 = |2(1 + iT) + ivTe^{i\psi}|^2, \quad (3.28)$$

and so

$$T = \frac{v \sin \psi}{1 + v \cos \psi + \frac{1}{4}v^2}. \quad (3.29)$$

Thus incorporating (3.25) and (3.26) with (3.29) gives ψ as an implicit function of v :

$$\tan\left(\frac{2v \sin \psi}{4 + 4v \cos \psi + v^2}\right) = \frac{v \sin \psi}{2 + v \cos \psi}. \quad (3.30)$$

It can be easily seen that the maximum v for which a fixed point exists occurs when the circle sweeps out an angle of π radians, *i.e.* when $T = \pi$. Then (3.30)

gives $v \cos \psi = -2$, and (3.29) gives

$$v \sin \psi = \pi(1 + v \cos \psi + \frac{1}{4}v^2). \quad (3.31)$$

Hence

$$v = 2(1 + 4/\pi^2)^{\frac{1}{2}} \approx 2.37089 \quad (3.32)$$

is the speed of projection above which the fixed point disappears, and occurs at the energy,

$$E = \frac{1}{2}v^2 = \frac{8}{\pi^2} \approx 0.810569. \quad (3.33)$$

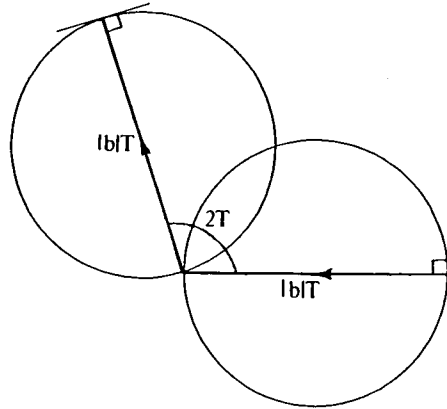


Figure 3.3.2. A two-cycle viewed in the laboratory frame.

A two-cycle is the next possibility. In the laboratory frame (see figure (3.3.2)) we see that a two-cycle occurs when the particle is projected directly at the axis of rotation, *at any speed* large enough to avoid hitting the circle before reaching the centre. In the rotating frame we have

$$b = -|b| = i(2 + ve^{i\psi}). \quad (3.34)$$

Therefore

$$\tan \psi = -\sqrt{\frac{1}{4}v^2 - 1} \quad (3.35)$$

and

$$T = \frac{2}{|b|} = -\frac{1}{\tan \psi} = \frac{1}{\sqrt{\frac{1}{4}v^2 - 1}}. \quad (3.36)$$

The minimum speed mentioned occurs when the particle hits the axis tangential

to the edge (in either the laboratory or the rotating frame). This occurs when the circle rotates through $\frac{\pi}{2}$ radians, so $T = \frac{\pi}{2}$. Then

$$v = 2(1 + 4/\pi^2)^{\frac{1}{2}} \approx 2.37089 \quad (3.37)$$

This is also the speed for which the fixed point disappears. Hence the fixed point bifurcates into a two-cycle here.

The stability of fixed points and p-cycles can be studied by linearising about one point in the cycle. Let $\mathbf{x} = (\theta, \psi)$ and let $\{\mathbf{X}_1, \mathbf{X}_2, \dots, \mathbf{X}_p\}$ be the p-cycle with

$$\mathbf{X}_i = \mathbf{F}^i(\mathbf{X}_1) \quad (3.38)$$

and

$$\mathbf{F}^p(\mathbf{X}_i) = \mathbf{X}_i. \quad (3.39)$$

Define the map $\mathbf{G} \equiv \mathbf{F}^p$, then $\{\mathbf{X}_1, \mathbf{X}_2, \dots, \mathbf{X}_p\}$ are fixed points of \mathbf{G} . Now regard a point close to \mathbf{X}_1 , say $\mathbf{x}_i = \mathbf{X}_1 + \delta_i$ and let

$$\mathbf{x}_{i+1} = \mathbf{G}(\mathbf{x}_i). \quad (3.40)$$

Then linearising about \mathbf{X}_1 gives

$$\begin{aligned} \mathbf{x}_{i+1} &= \mathbf{G}(\mathbf{X}_1) + J_G(\mathbf{X}_1)\delta_i \\ &= \mathbf{X}_1 + J_G(\mathbf{X}_1)\delta_i \\ \delta_{i+1} &= J_G(\mathbf{X}_1)\delta_i, \end{aligned} \quad (3.41)$$

where

$$J_G = \begin{pmatrix} \frac{\partial G_\theta}{\partial \theta} & \frac{\partial G_\psi}{\partial \theta} \\ \frac{\partial G_\theta}{\partial \psi} & \frac{\partial G_\psi}{\partial \psi} \end{pmatrix}. \quad (3.42)$$

Using the chain rule, we can express J_G in terms of J_F , so

$$\delta_{i+1} = J_F(\mathbf{X}_p)J_F(\mathbf{X}_{p-1})\dots J_F(\mathbf{X}_1)\delta_i. \quad (3.43)$$

J_F is called the tangent map of F . Now δ_1 can be written in terms of the

eigenvectors \mathbf{u} of J_G defined by $J_G \mathbf{u}_j = \sigma_j \mathbf{u}_j$, so

$$\delta_1 = \sum_{j=1}^2 c_j \mathbf{u}_j. \quad (3.44)$$

Hence

$$\delta_n = \sum_{j=1}^2 c_j \sigma_j^n \mathbf{u}_j. \quad (3.45)$$

So the condition for stability of the fixed point, *i.e.* that δ_n is bounded as $n \rightarrow \infty$, is that $|\sigma_j| \leq 1$ for all j . In particular, if $|\sigma_1| = 1$ and $|\sigma_2| = 1$, the fixed point is elliptic. In Appendix A, the Jacobian J_F is calculated in terms of θ, ψ, v and T , where T is calculated numerically for general (θ, ψ) or by using the above formulae for a fixed point or a two-cycle. Because the system is Hamiltonian, $|\sigma_1| = |\sigma_2| = 1$ for a stable p-cycle and hence all stable p-cycles of two-dimensional Hamiltonian systems are elliptic. The stabilities of the fixed point and the two-cycle were calculated for $-2 \leq E \leq 22.5$. It was found that the fixed point is stable for $-2 \leq E \leq -0.39$, and the two-cycle stable for $1.51 \leq E \leq \infty$. The positions and stabilities of these are summarised in figure (3.3.3), showing the bifurcation at $E = 8/\pi^2$. There is also another two-cycle which exists between the points of the first two-cycle, but it has been difficult to find this using methods similar to those above, and less fruitful methods such as Newton's method in two dimensions are required.

3.4 Approximate Solutions for Adiabatic Skipping

We have seen that there is a wide variety of types of motion in the rotating circle. There are fixed points and periodic orbits. There is also quasi-periodic motion where the trajectory is restricted to a two-dimensional surface of phase space. A subset of the latter occurs when the particle ‘skips’ in small steps along the boundary of the circle. It is then possible to find the invariant curve in (θ, ψ) space along which these steps lie, by approximating T to be small. We start by

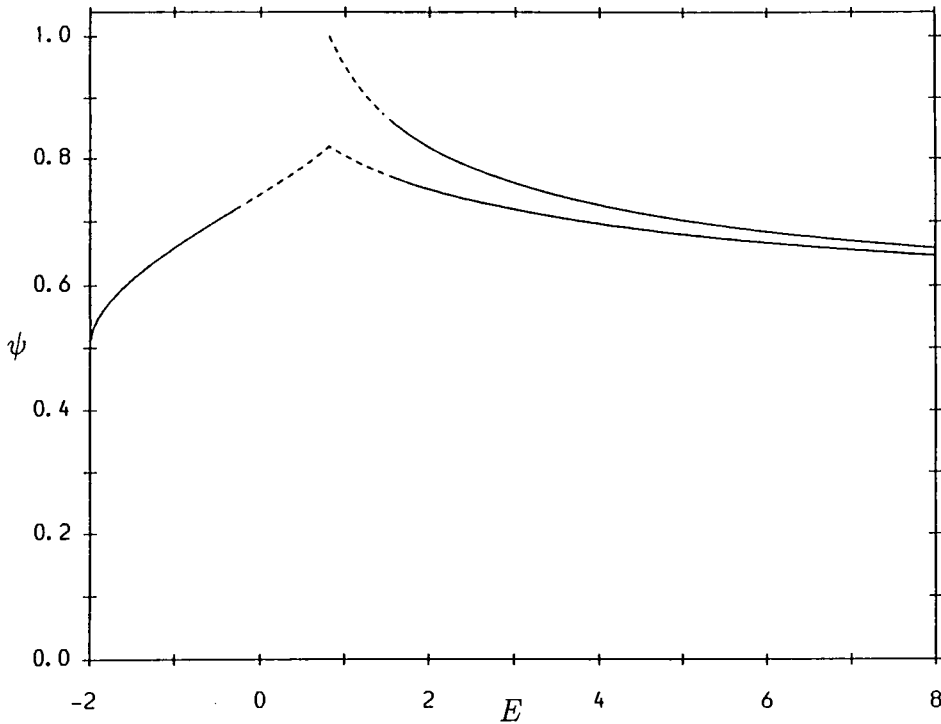


Figure 3.3.3. The angle of projection ψ for the fixed point and a two-cycle, versus the energy E . The full lines indicate that the periodic orbit is stable, broken lines that it is unstable.

expanding $z(T)$ as a power series in T to order T^2 to give

$$T \approx \frac{2v \sin \psi}{v^2 + 2v \cos \psi + \cos \theta + 1}. \quad (3.46)$$

Suppose that $\Delta\theta, \Delta\psi, \Delta v$ are the changes in θ, ψ, v respectively from one bounce to the next. Then using the equation of motion (3.12) and the boundary conditions (3.13) we obtain

$$U = (v + \Delta v)e^{i(\Delta\theta - \psi - \Delta\psi)} = [v(1 - iT)e^{i\psi} - iT(1 + e^{-i\theta})]e^{-iT} \quad (3.47)$$

and

$$e^{i\Delta\theta} = [(1 + e^{-i\theta})(1 + iT) + ivTe^{i\psi}]e^{-iT} - e^{-i\theta}. \quad (3.48)$$

Equations (3.47) and (3.48) are exact. From these and using (3.46) we obtain

$$\Delta\theta \approx vT \cos \psi. \quad (3.49)$$

But the calculation for $\Delta\psi$ gives $\Delta\psi \approx 0$, which indicates that we need to find the next term in T . These further calculations could not be pursued for arbitrary

ψ so we will restrict ourselves to small ψ and expand everything else to second order in ψ . Firstly we write

$$e^{-iT} \approx 1 - iT - \frac{1}{2}T^2 + \frac{1}{6}T^3 \quad (3.50)$$

so

$$z(T) \approx a + \dot{z}_0 T - i(\dot{z}_0 + \frac{1}{2}ia)T^2 - (\frac{1}{2}\dot{z}_0 + \frac{1}{3}ia)t^3, \quad (3.51)$$

where \dot{z}_0 is the velocity in the rotating frame at $t = 0$. This has one root greater than zero, namely

$$T = \frac{2v\psi}{(v+1)^2 + \cos\theta} + \frac{4v^2(v + \frac{2}{3})\sin\theta}{[(v+1)^2 + \cos\theta]^3}\psi^2 + \mathcal{O}(\psi^3). \quad (3.52)$$

We will write the first two terms as $A\psi$ and $B\psi^2$ respectively for convenience. As before we calculate $\Delta\theta$ and $\Delta\psi$. Equation (3.48) gives

$$\Delta\theta \approx vA\psi + (vB - \frac{1}{2}A^2\sin\theta)\psi^2 \quad (3.53)$$

and equation (3.47) gives

$$\begin{aligned} U &\approx [v - A\psi\sin\theta] \\ &+ i[v(1 - 2A) - A(1 + \cos\theta)]\psi + i[-B(1 + \cos\theta) + A^2\sin\theta - 2vB]\psi^2 \\ &= U_0^{(r)} + U_1^{(r)}\psi + iU_1^{(i)}\psi + U_2^{(i)}\psi^2. \end{aligned} \quad (3.54)$$

Hence

$$\begin{aligned} \arg U &\approx \left(\frac{U_1^{(r)}}{U_0^{(r)}}\right)\psi + \left(\frac{U_2^{(i)}}{U_0^{(r)}} - \frac{U_1^{(i)}U_1^{(r)}}{[U_1^{(r)}]^2}\right)\psi^2 \\ &= \left\{1 - A\left[2 + \frac{1+\cos\theta}{v}\right]\right\}\psi \\ &+ \left\{\frac{A\sin\theta}{v}\left[1 - A\left(1 + \frac{1+\cos\theta}{v}\right)\right] - B\left[2 + \frac{1+\cos\theta}{v}\right]\right\}\psi^2. \end{aligned} \quad (3.55)$$

So $\Delta\psi = \Delta\theta - \psi - \arg U$ gives

$$\Delta\psi \approx \frac{2(4v + 3\cos\theta + 3)\sin\theta}{3[(v+1)^2 + \cos\theta]^2}\psi^2. \quad (3.56)$$

Suppose $d\psi/d\theta$ is the tangent to the invariant curve. Then using the approxi-

mation

$$\frac{d\psi}{dv} = \frac{d\theta}{dv} \frac{d\psi}{d\theta} \approx -\frac{v}{\sin \theta} \frac{\Delta\psi}{\Delta\theta} \quad (3.57)$$

gives

$$\frac{d\psi}{dv} \approx -\frac{(3v^2 + 8v - 6E)}{3v(3v^2 + 4v - 2E)} \psi. \quad (3.58)$$

Hence

$$\psi \approx \text{const } (3v^2 + 4v - 2E)^{\frac{1}{3}}/v. \quad (3.59)$$

Equation (3.59) gives the shape of the invariant curves for small angle skipping motion in the anticlockwise sense. It is interesting to pursue these calculations for when $\psi \sim \pi$ and the motion is clockwise. We write $\psi = \pi - \varepsilon$ and again calculate terms to second order, this time in ε . By similar methods we find

$$T = \frac{2v\varepsilon}{(v-1)^2 + \cos \theta} + \frac{4v^2(-v + \frac{2}{3}) \sin \theta}{[(v-1)^2 + \cos \theta]^3} \varepsilon^2 + \mathcal{O}(\varepsilon^3). \quad (3.60)$$

Let us write these coefficients of ε and ε^2 as A' and B' respectively. Then

$$\Delta\theta \approx -vA'\varepsilon + (-vB' - \frac{1}{2}A'^2 \sin \theta)\varepsilon^2 \quad (3.61)$$

$$\Delta\varepsilon \approx \frac{2(4v - 3\cos \theta - 3) \sin \theta}{3[(v-1)^2 + \cos \theta]^2} \varepsilon^2, \quad (3.62)$$

which gives

$$\varepsilon \approx \text{const } (3v^2 - 4v - 2E)^{\frac{1}{3}}/v. \quad (3.63)$$

Equation (3.63) gives the invariant curves for small angle skipping motion in the clockwise sense.

Let us see when equations (3.59) and (3.63) are valid. Both equations fail as v approaches zero, because the respective angles ψ, ε become large. Physically, the particle is near the classically forbidden region, and is close to the point of reversing direction. We also expect difficulties when the expressions inside the cube roots become negative. This does not occur for equation (3.59) for any

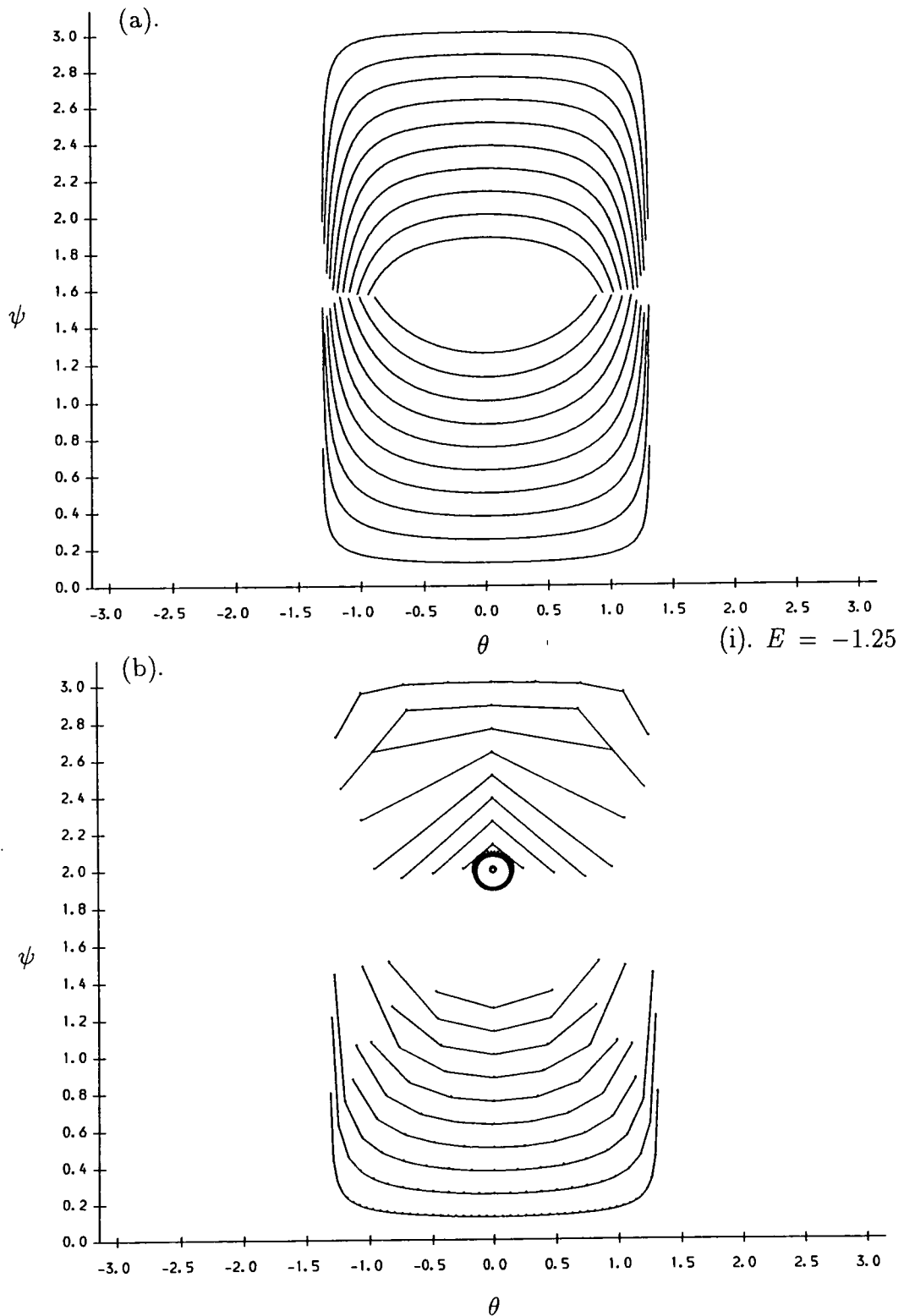


Figure 3.4.1. (a). Approximate invariant curves, (b). exact invariant curves for the rotating circle. (i). $E = -1.25$. (ii). $E = -\frac{2}{3}$. (iii). $E = -\frac{1}{2}$. (iv). $E = 0$. (v). $E = 1$. (vi). $E = 2$. (vii). $E = 3$. (viii). $E = 10$.

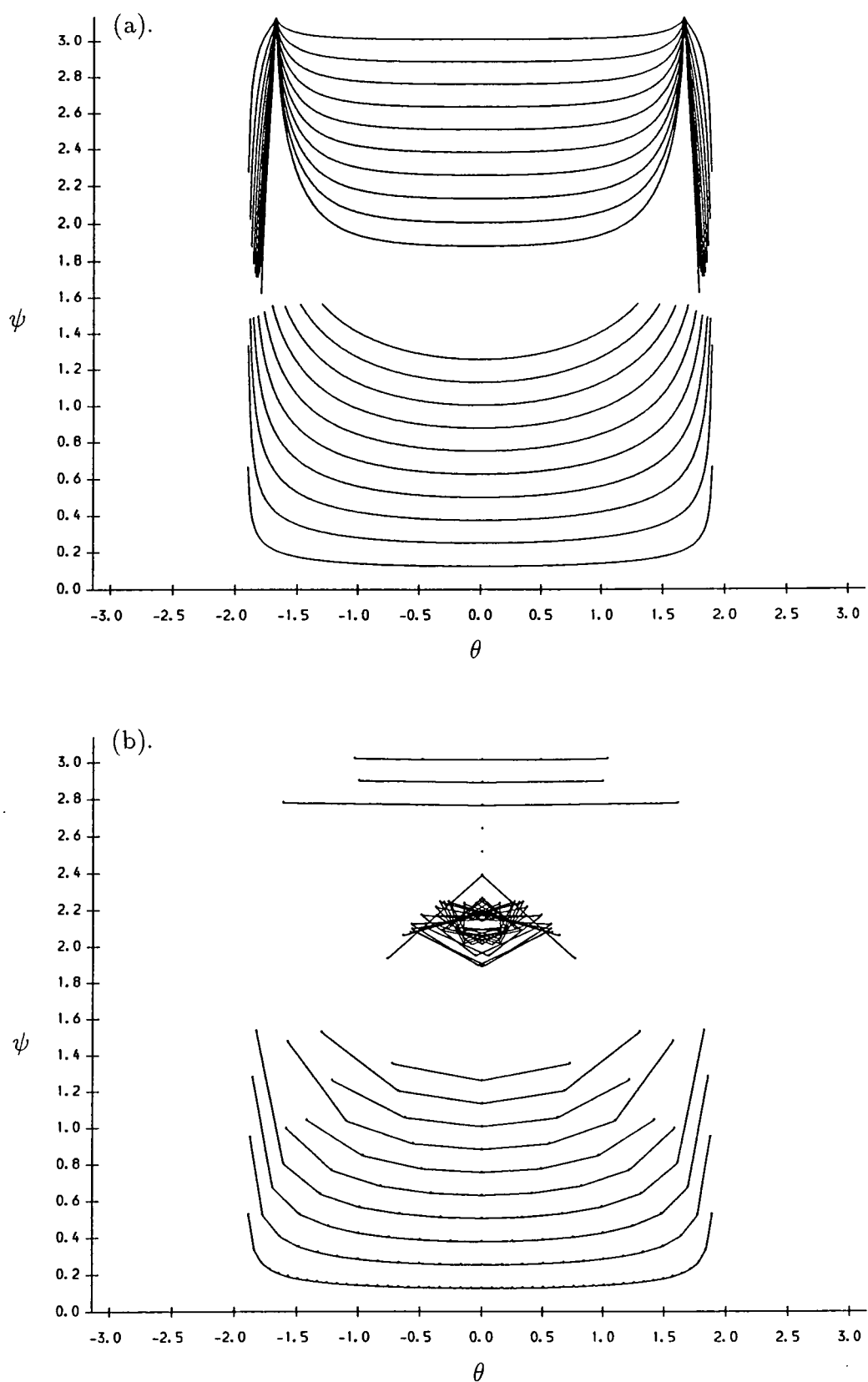


Figure 3.4.1. (continued) (ii). $E = -\frac{2}{3}$

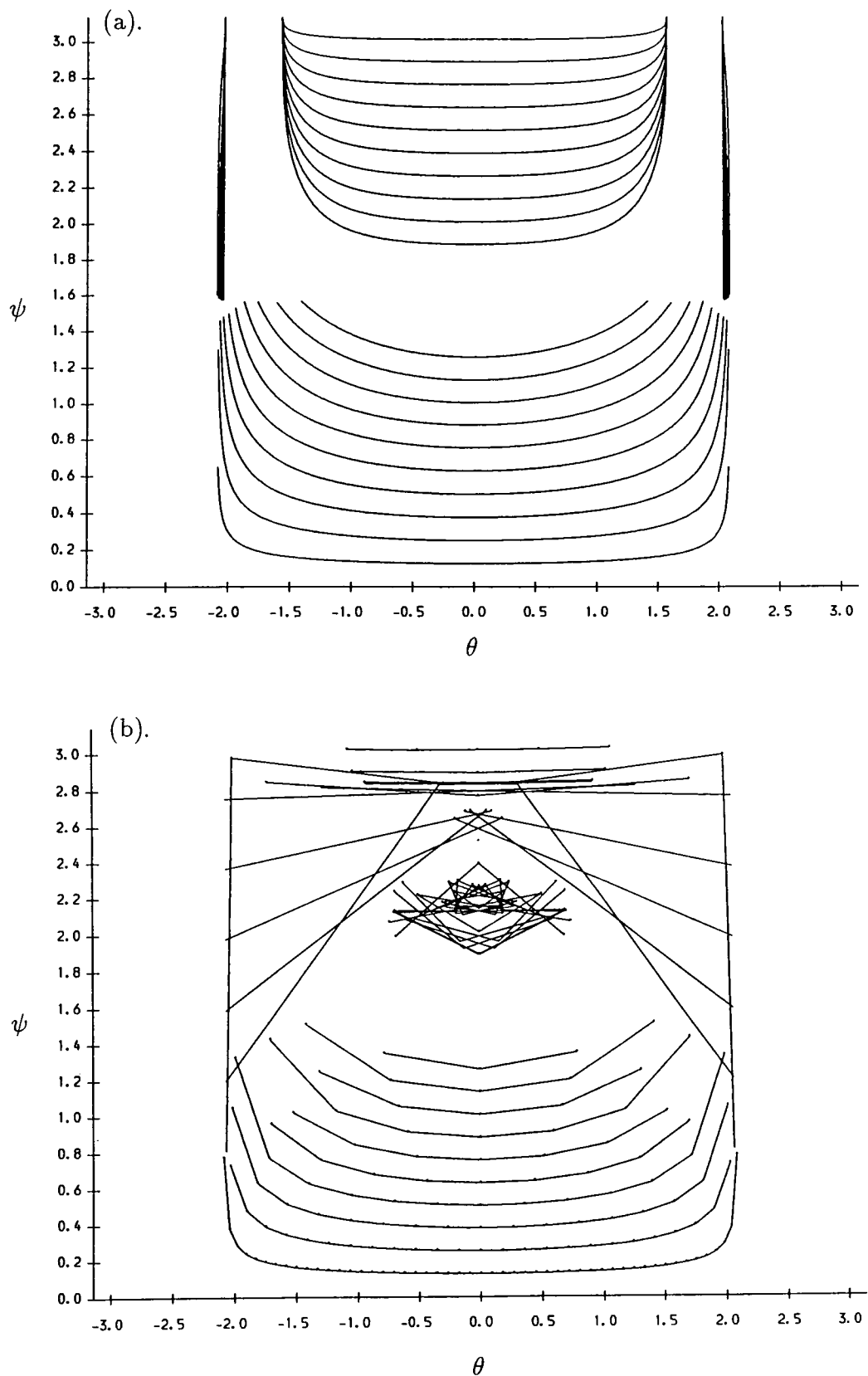
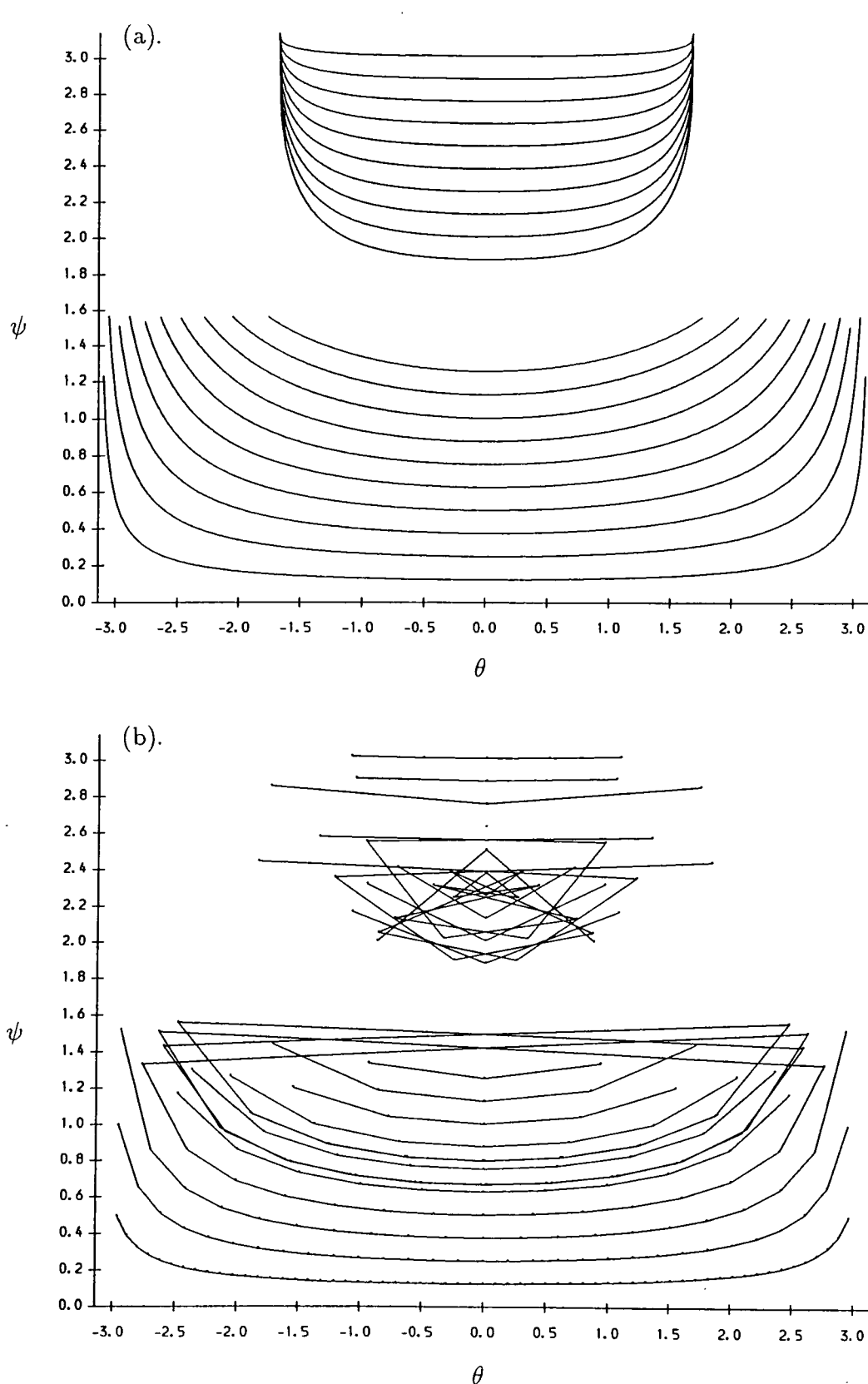
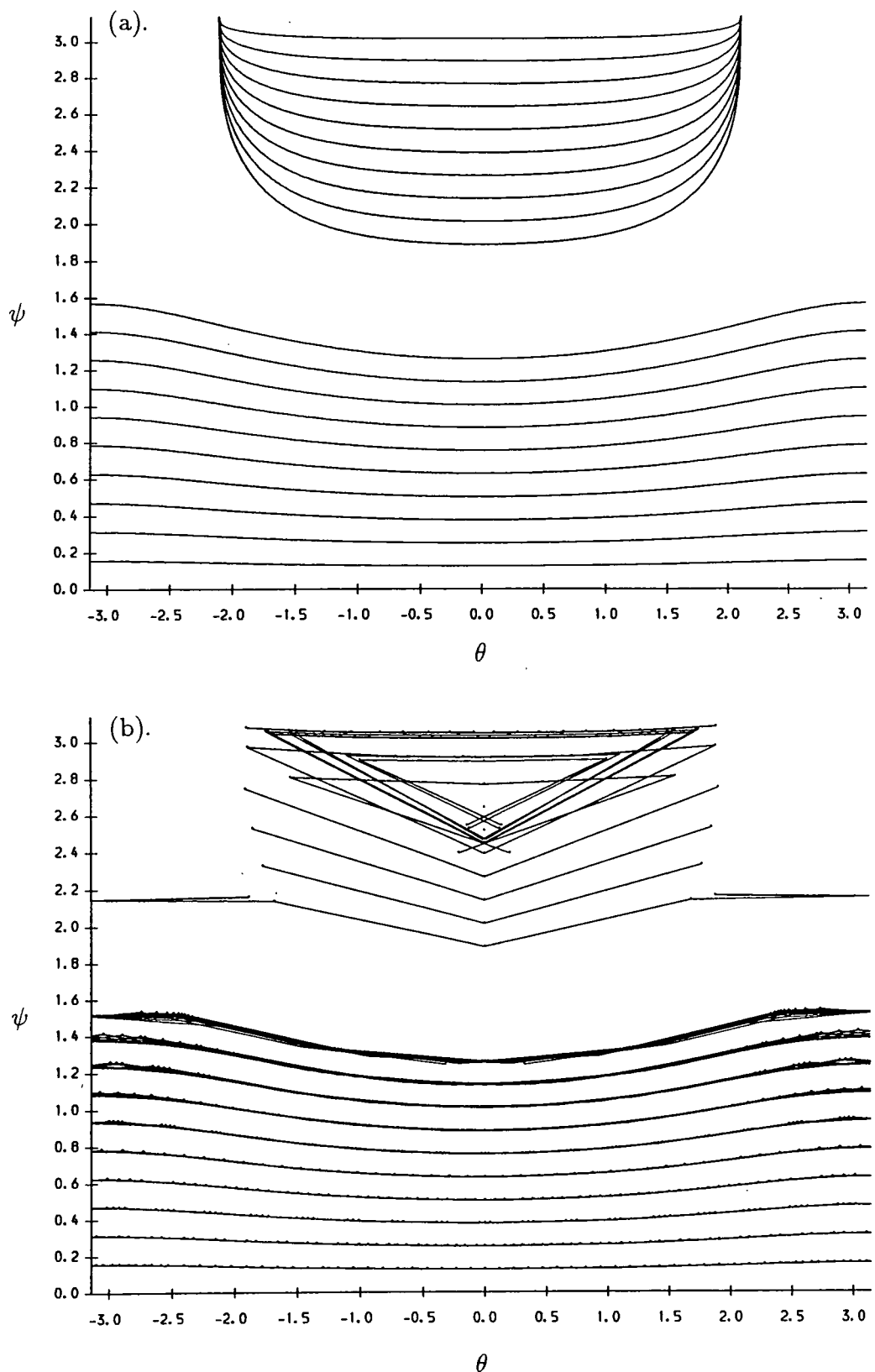
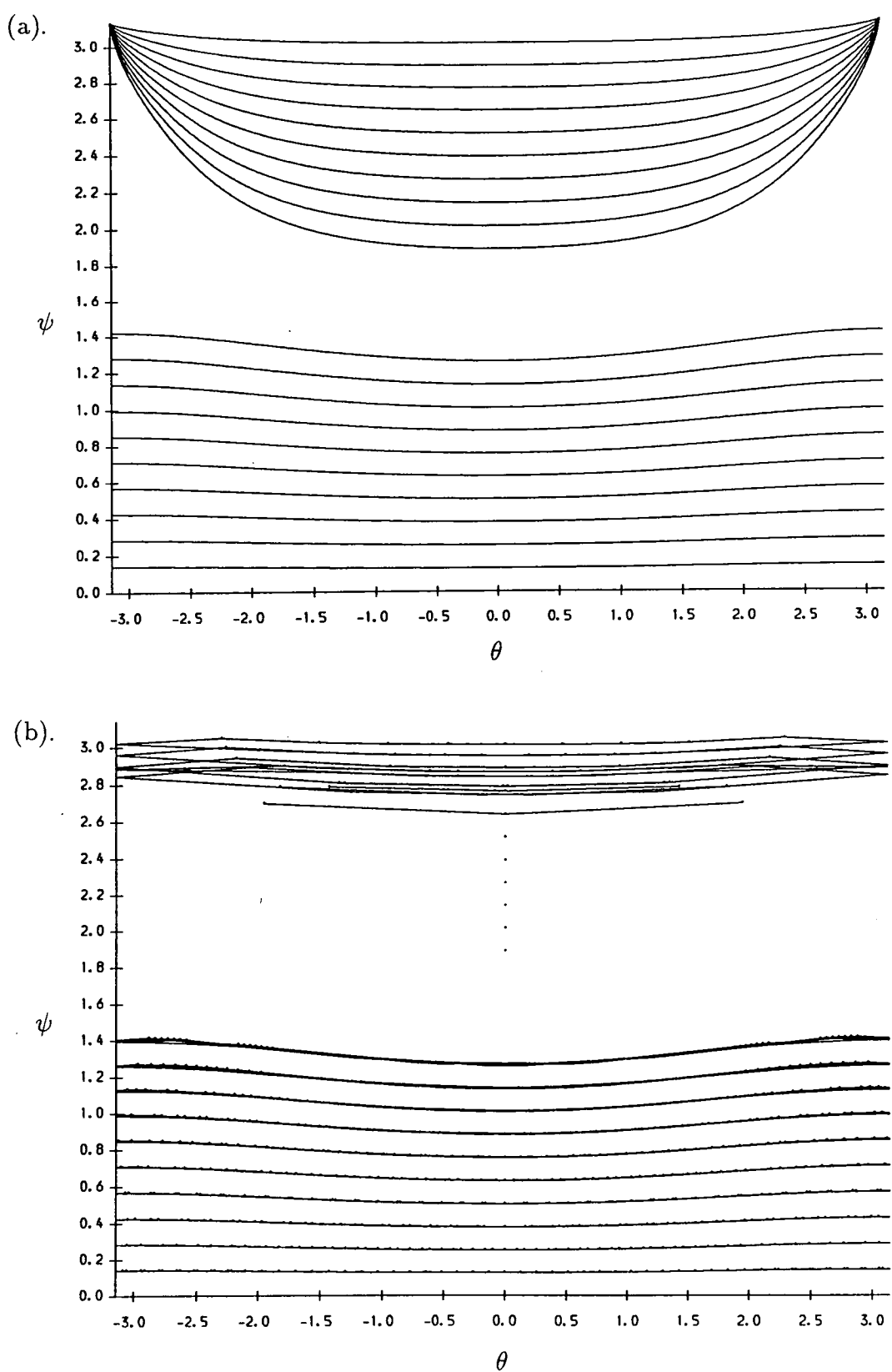


Figure 3.4.1. (continued) (iii). $E = -\frac{1}{2}$

Figure 3.4.1. (continued) (iv). $E = 0$

Figure 3.4.1. (continued) (v). $E = 1$

Figure 3.4.1. (continued) (vi). $E = 2$

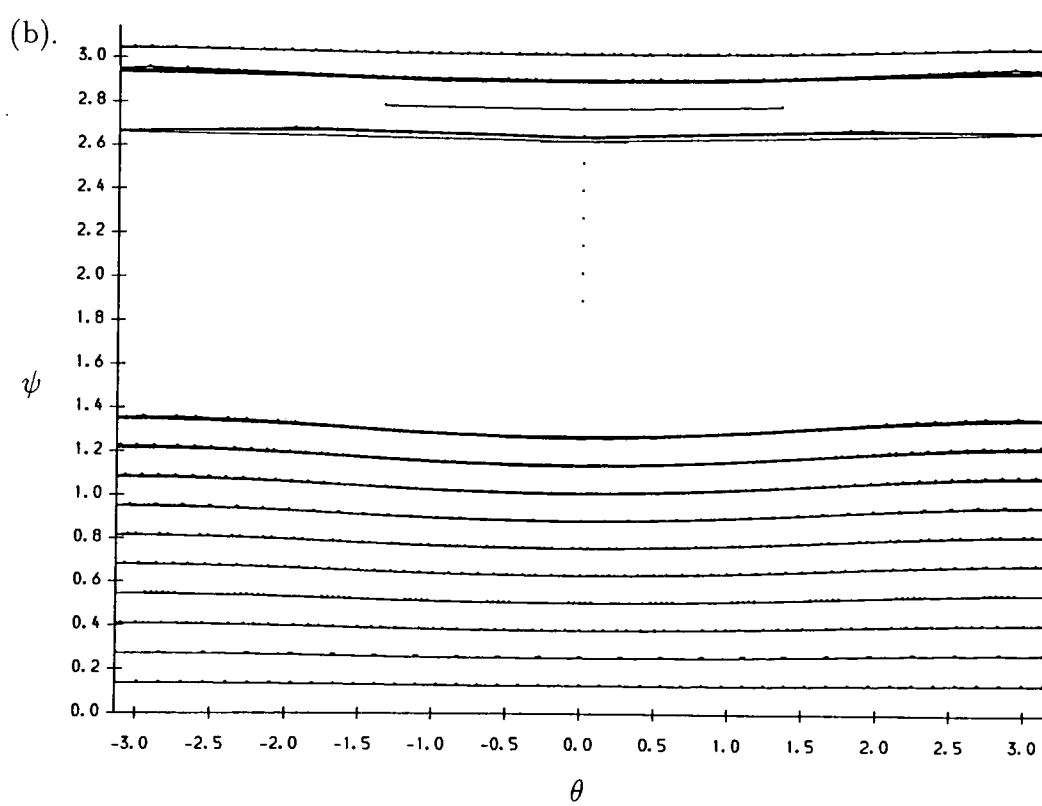
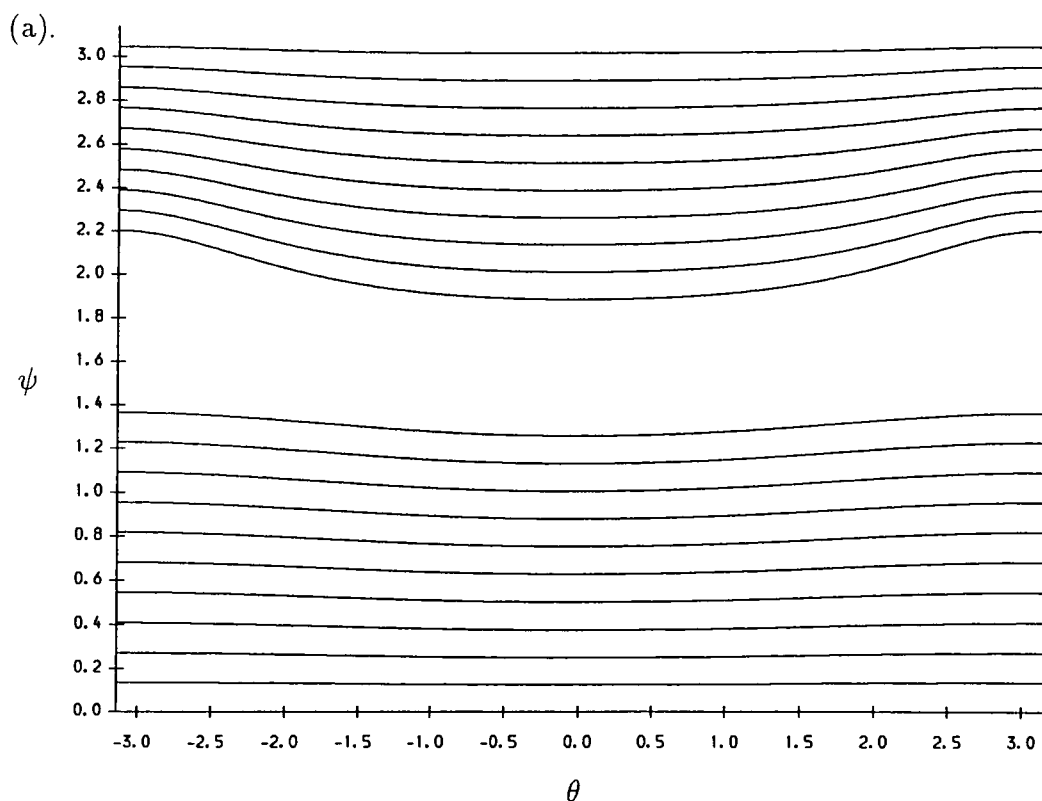


Figure 3.4.1. (continued) (vii). $E = 3$

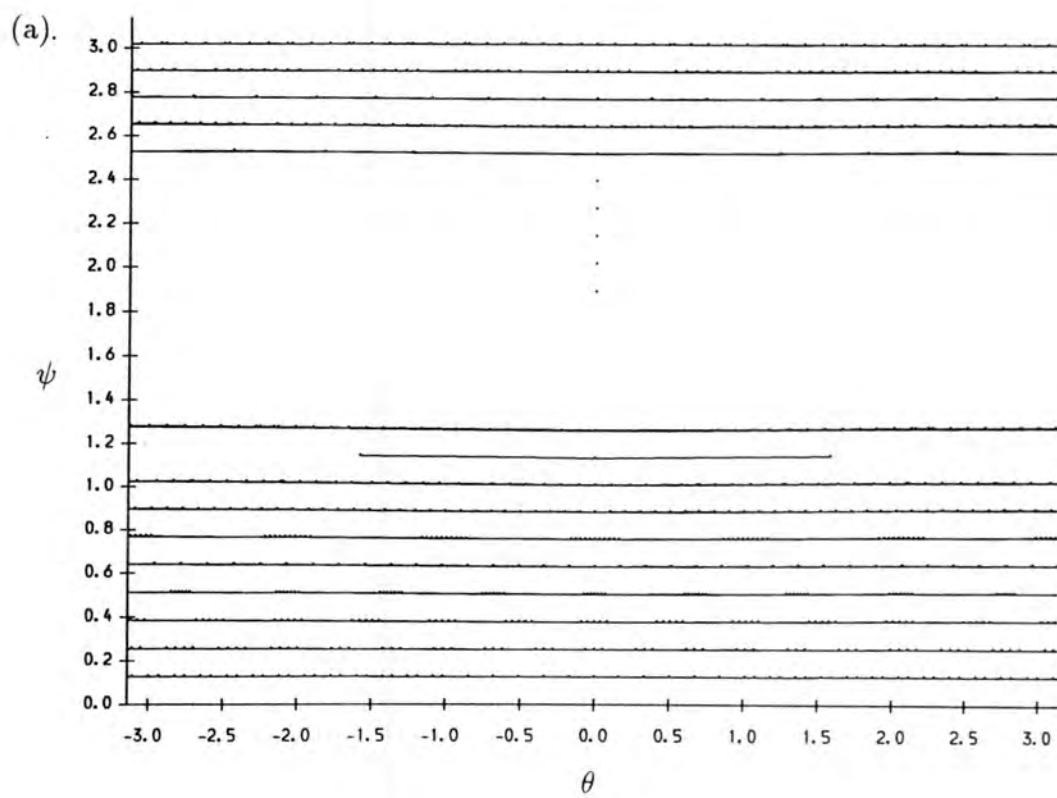
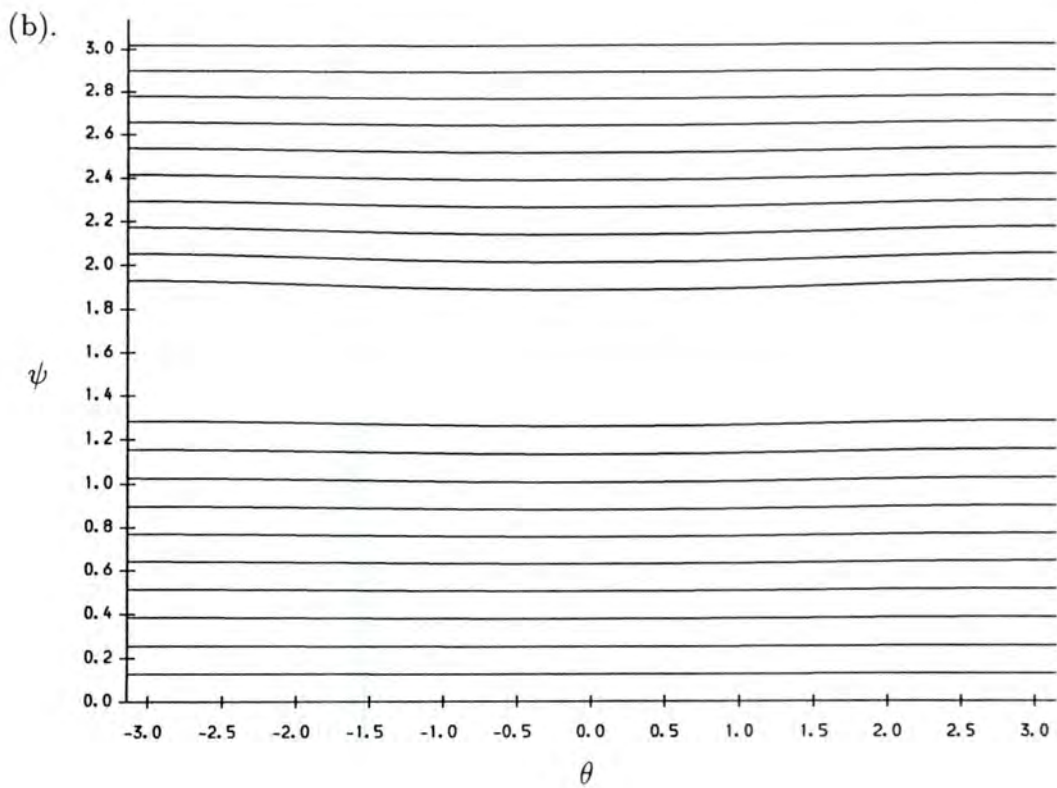


Figure 3.4.1. (continued) (viii). $E = 10$

value of E . However, for equation (3.63), the negative sign of the $4v$ term means that there is a singularity at $(v - 1)^2 + \cos \theta = 0$, so that the corresponding expression is negative for θ in the range,

$$-\frac{5}{9} - \frac{2}{3}E - \frac{2}{9}\sqrt{4+6E} < \cos \theta < -\frac{5}{9} - \frac{2}{3}E + \frac{2}{9}\sqrt{4+6E}. \quad (3.64)$$

with E in the range $(-\frac{2}{3}, 2)$. This is interesting, because it is also the range of θ, E for which glancing trajectories can occur, as we shall see in a later section. Here in the clockwise motion (we shall see later) there is no possibility of glancing, so invariant curves exist near $\psi = 0$. In the anti-clockwise direction, there can be glancing; these give discontinuities in the surface of section, and so invariant curves do not exist near $\psi = \pi$.

Examples of both types of adiabatic motion are shown in figure (3.4.1).

3.5 The Poincaré Map

For the rotating circle the surface of section is given in terms of the coordinates (θ, ψ) within the surface, as defined in section (3.2). The Poincaré map is symmetric about the axis $\theta = 0$ due to invariance of the Hamiltonian under time reversal and x -axis reflection combined (so-called TS_x symmetry).

The maps for various energies are shown in figure (3.5.1). One hundred trajectories are followed on a ten by ten lattice for 250 bounces each. The first energy $E = -1.25$ shows rings of island tori encircling the fixed point found in section (3.3). Between these tori are regions of chaos and from an examination of the order in which the dots build up on the terminal screen (which the figures cannot show), the chaotic trajectories do not pass from one region to another. The explanation for this is that large tori, each one encircling the fixed point, restrict these trajectories between them. Examples of these can be seen in the figure. At $E = -1$ there is no evidence for these large tori, and if we look at just one trajectory for a large number of iterations (figure (3.5.2)), we see that it covers most of the Poincaré section except the outermost region. The region of stability of the fixed point is much smaller than for $E = -1.25$ and the lack of influence of the fixed point accounts partly for the increase in chaos.

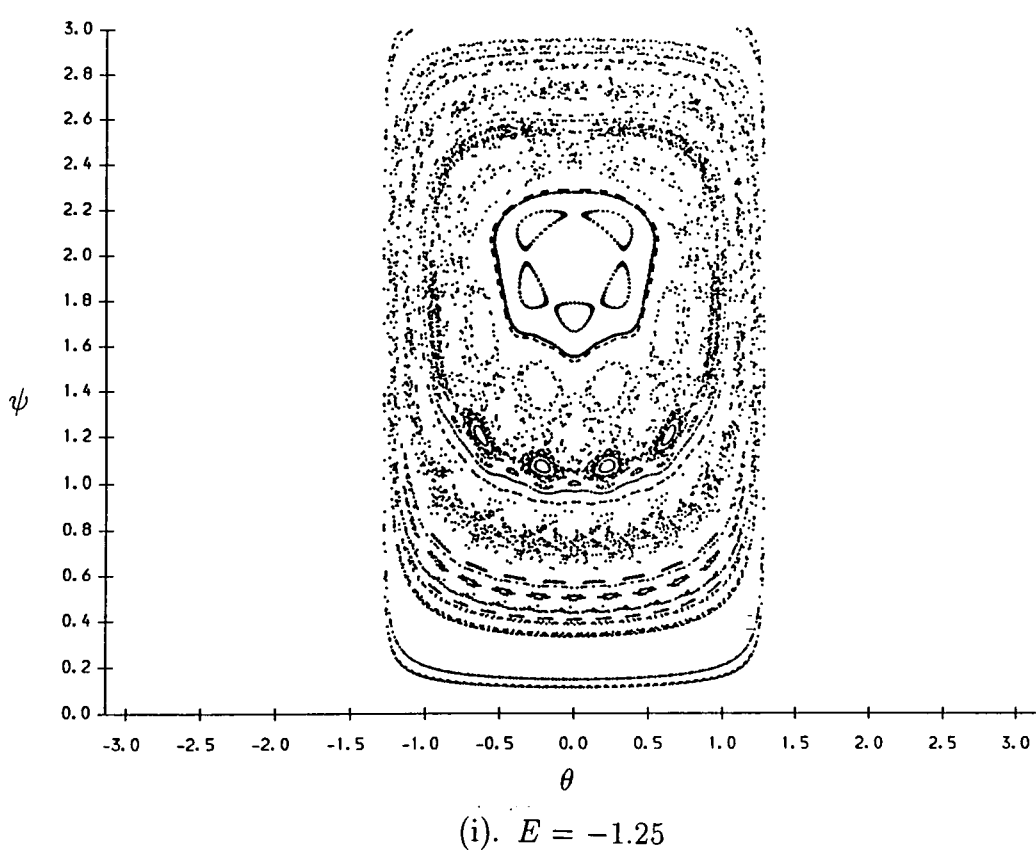


Figure 3.5.1. Poincaré maps for 100 traj., initially on a 10 by 10 grid, followed for 250 bounces. (i). $E = -1.25$, (ii). $E = -1$, (iii). $E = 1$, (iv). $E = 2$, (v). $E = 2.5$, (vi). $E = 3$, (vii). $E = 10$.

At $E = -0.38$ the 4-cycle which appeared at $E = -1$ has disappeared and the fixed point is again less stable. At $E = 0$ the fixed point cannot be seen; only the analysis of section (3.3) shows that it still exists but is unstable. The phase space appears completely ergodic here. At $E = 1$ a stable 3-cycle appears while the 2-cycle is still unstable. At $E = 2$ this has disappeared and the 2-cycle found in section (3.3) has become stable, and remains stable for all higher energies. The lower half of the maps have bands of invariant curves which increase in number and extend to higher ψ as E increases from $E = 1$ to $E = 3.0$. At the energy $E = 3.0$ there reappear invariant bands in the upper plane which separate chaotic regions. For very low E the Poincaré map becomes very regular consisting mainly of invariant rings around a fixed point, and for very high E the map is also very regular consisting mainly of almost horizontal invariant bands across the map.

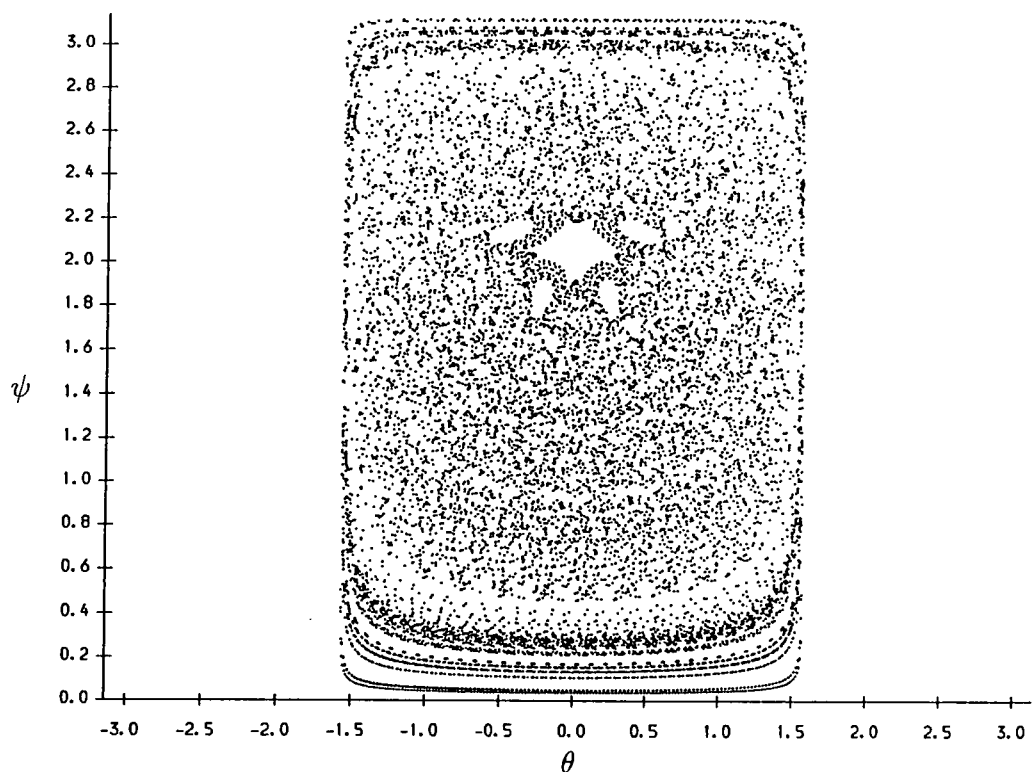
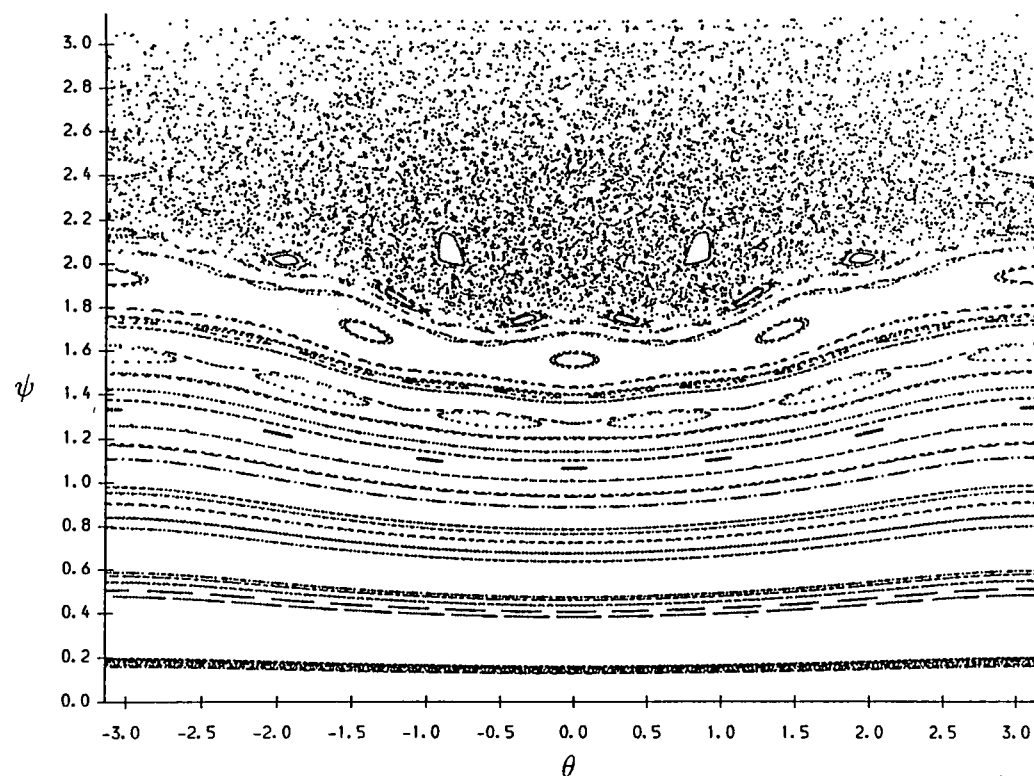
(ii). $E = -1$ (iii). $E = 1$

Figure 3.5.1. (continued)

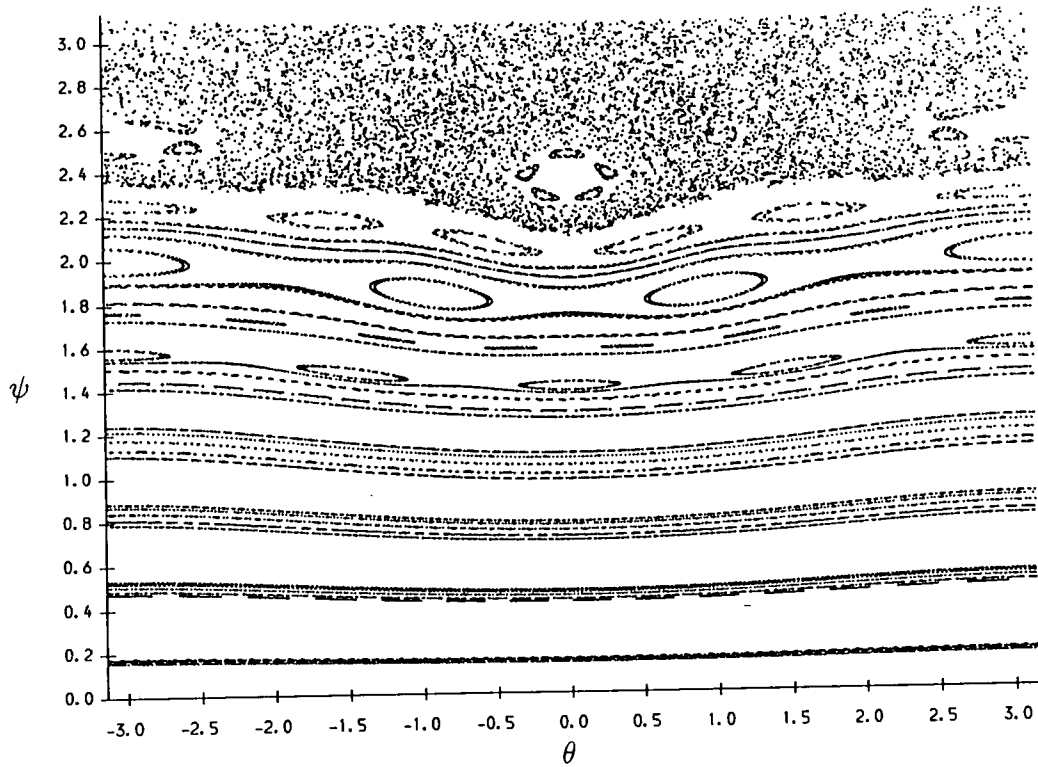
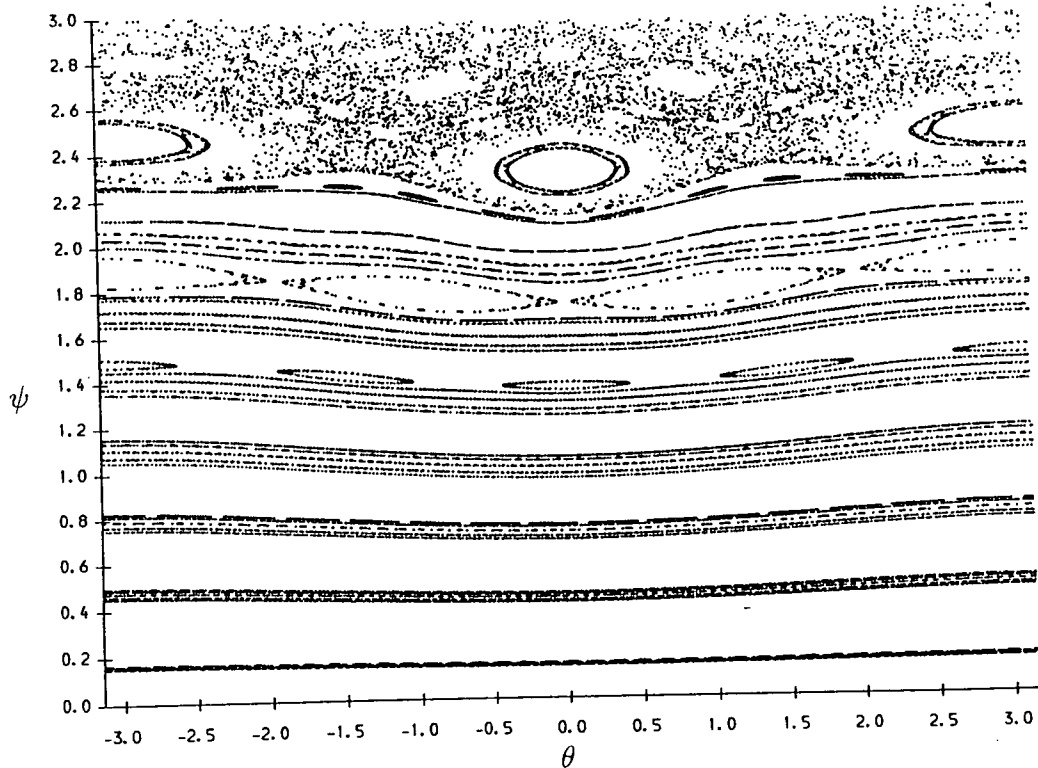
(iv). $E = 2$ 

Figure 3.5.1. (continued)

(v). $E = 2.5$

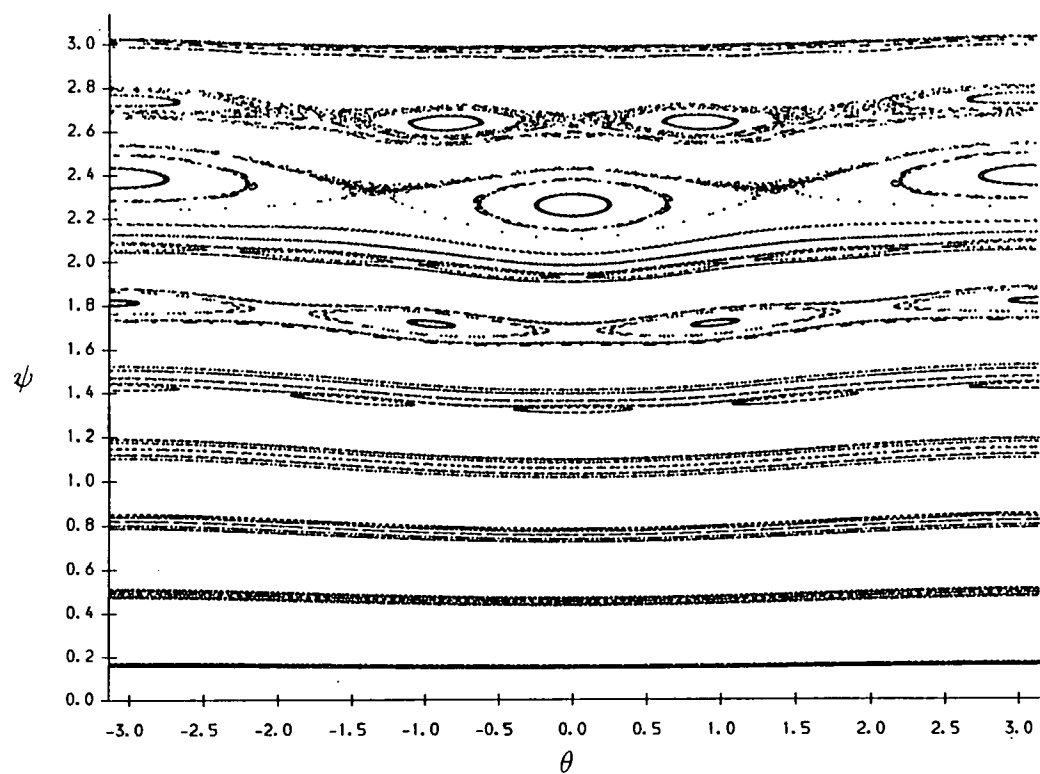
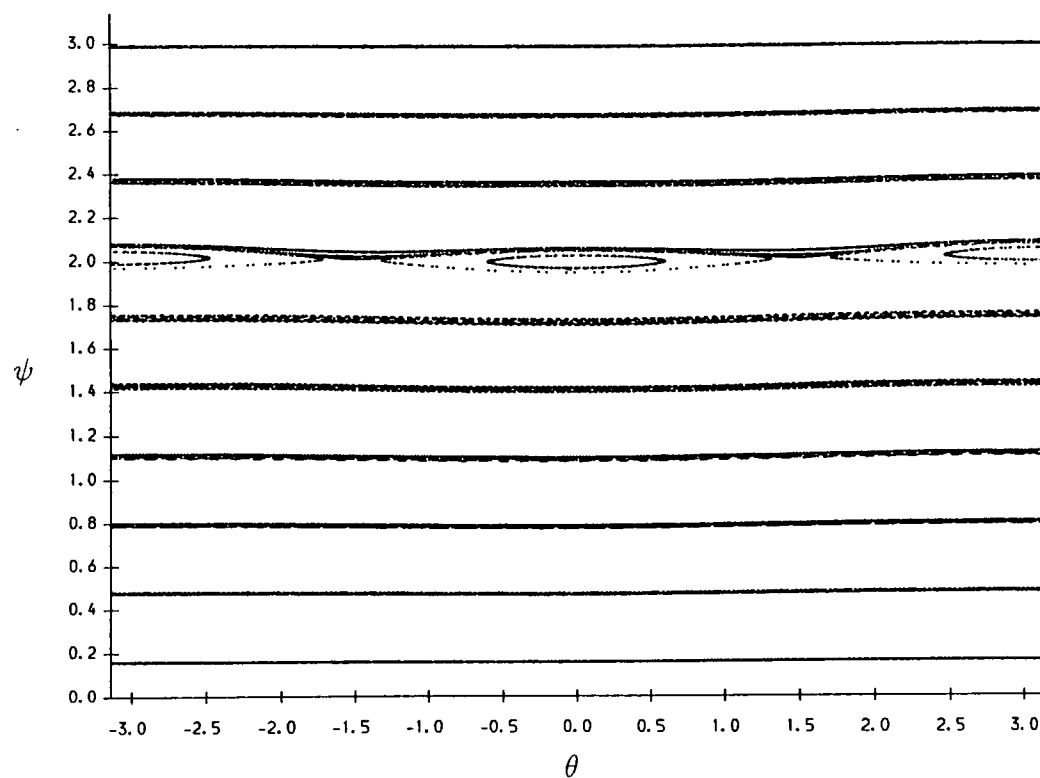
(vi). $E = 3$ (vii). $E = 10$

Figure 3.5.1. (continued)

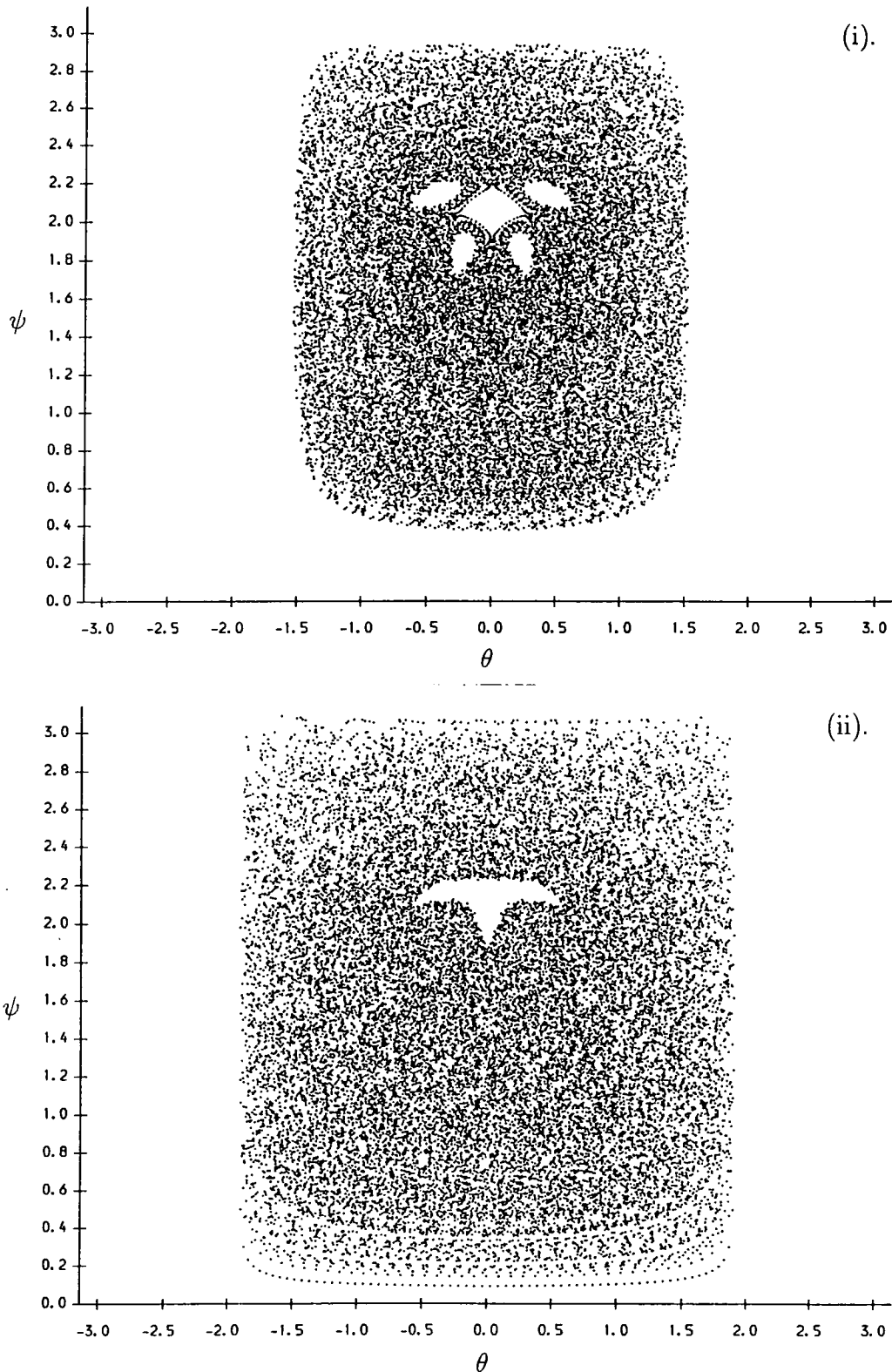


Figure 3.5.2. Poincaré maps for one trajectory followed for 25000 bounces. (i).

E = -1, (ii). E = $-\frac{2}{3}$, (iii). E = -0.38, (iv). E = 0.

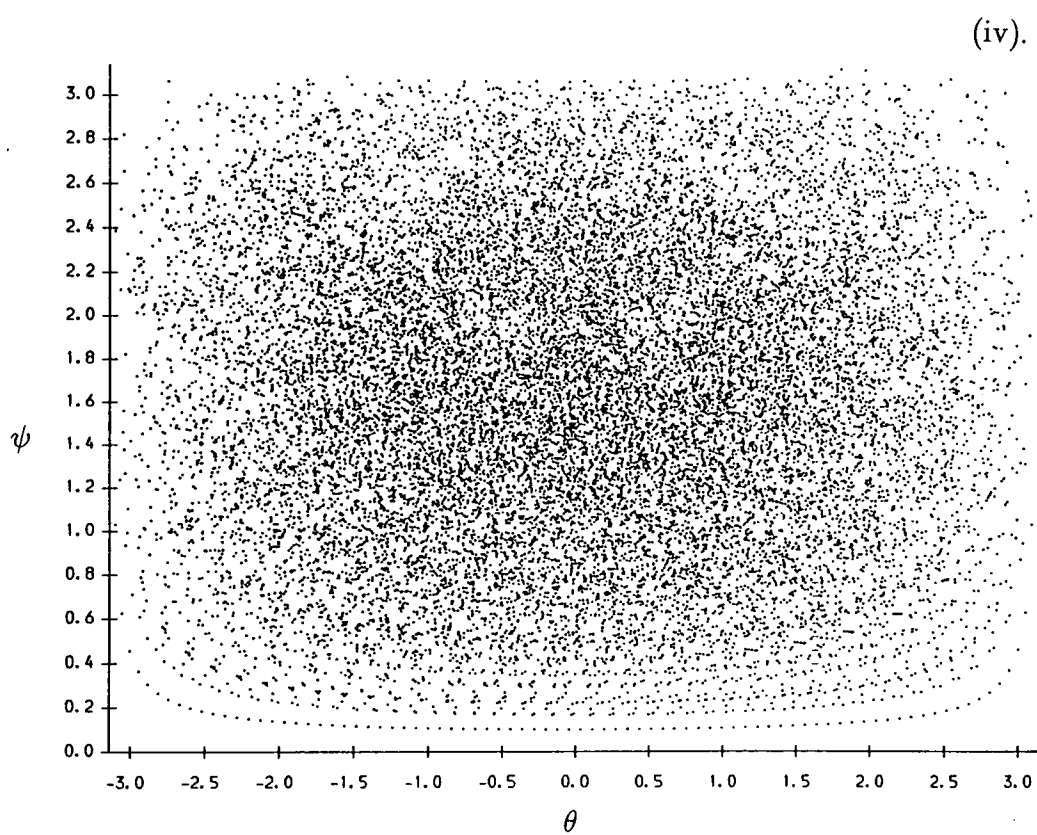
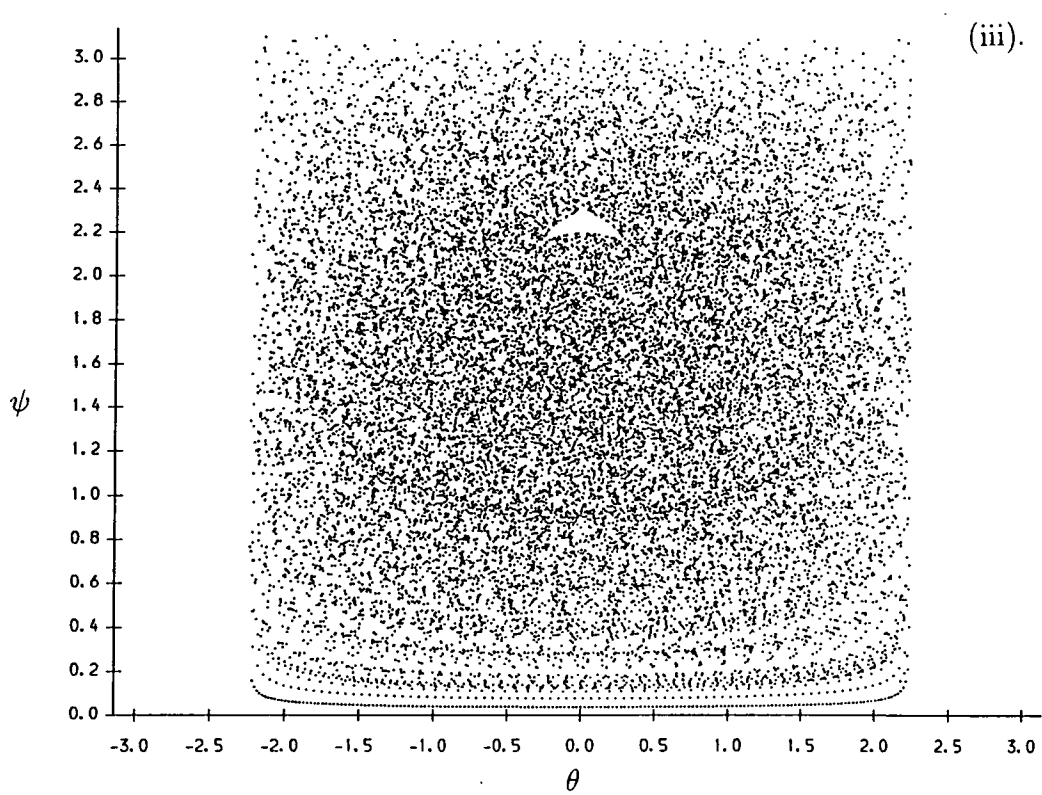


Figure 3.5.2. (continued)

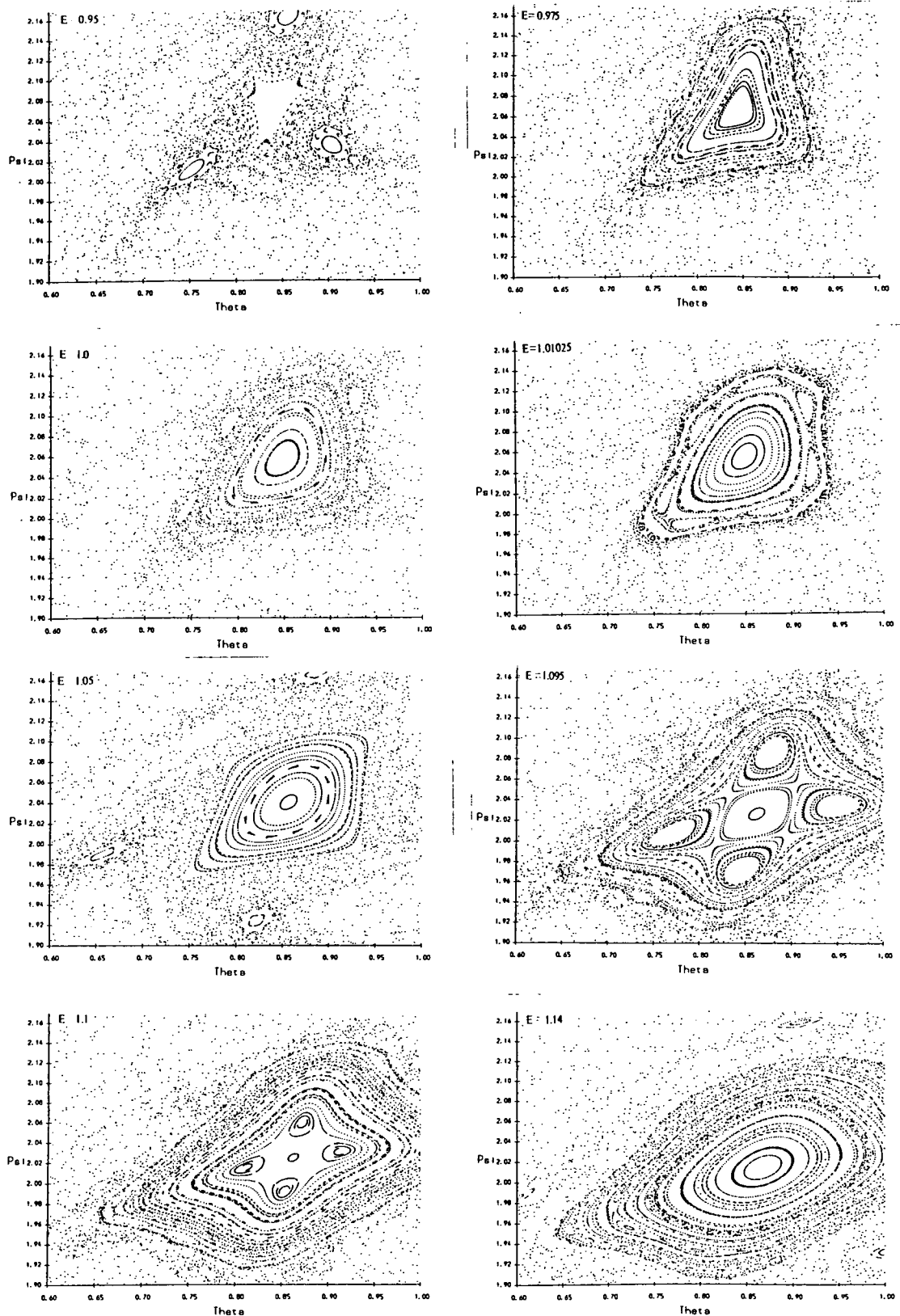


Figure 3.5.3. Enlargement of one point of the three-cycle (right of centre, figure 3.5.2(iii)), showing bifurcations for a succession of energies.

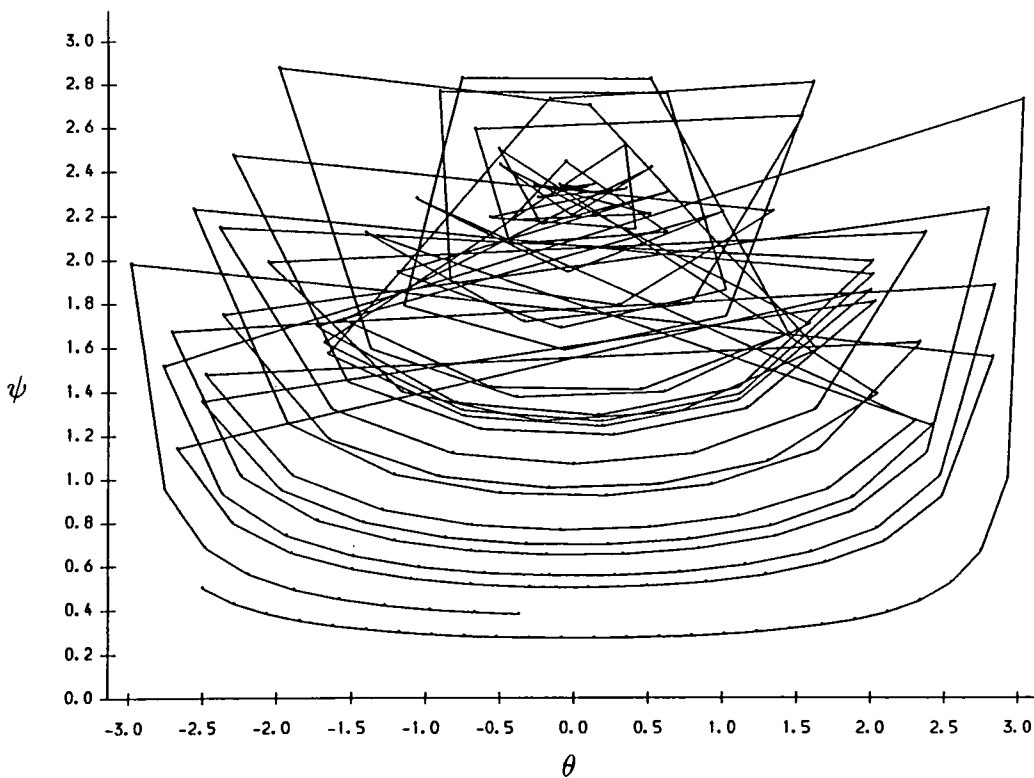
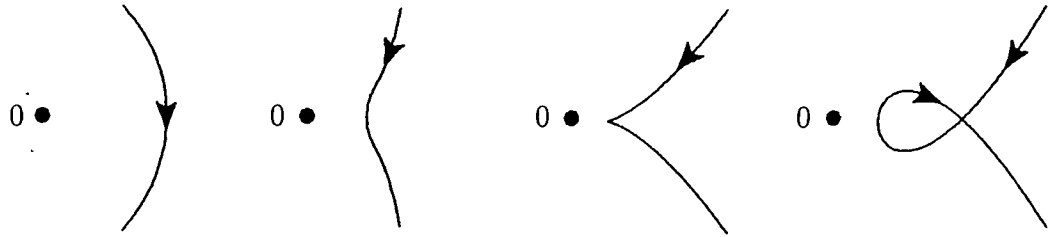


Figure 3.5.4. Joined Poincaré map for several bounces at $E = 0$ starting at $\theta_0 = 2.5$, $\phi_0 = 0.5$, showing mixture between chaotic motion and regular motion in one trajectory.

Some sections of the map are enlarged and a sequence at different energies displayed in figure (3.5.3), showing bifurcations of the periodic orbits into larger p -cycles. At $E = 0$, where the map is most chaotic, we have shown one trajectory drawn for many iterations with the dots in the Poincaré map joined by straight lines (figure (3.5.4)). The purpose of this was to show possible regular motion that would not be seen by just drawing dots. It can be seen that in the anti-clockwise motion the trajectory appears to be regular, but this is not so elsewhere. Thus the one trajectory appears to have both regular and chaotic components. This possibility is not considered in the usual definition of chaotic motion, where the Lyapunov exponent of instability is defined over infinite times so that the regular component is swamped out by the chaotic component. It may also explain why, in the computation of Lyapunov exponents, there still remains some fluctuations other than statistical.

3.6 Influence of Curvature of Trajectories



- (i). $F_{\text{Cor}} > F_{\text{cent}}$ (ii). $F_{\text{Cor}} < F_{\text{cent}}$ (iii). $F_{\text{Cor}} = 0$ (iv). $F_{\text{Cor}}, F_{\text{cent}} > 0$

Figure 3.6.1. Four types of trajectory possible for rotating billiards.

We shall see in this section that the changing curvature of the trajectories in the rotating frame is a significant source of chaos in the rotating billiard. All trajectories are arcs of four types of curve which were described by Frisk and Arvieu [60] (see figure (3.6.1)). These may be obtained by considering the forces acting at the point \mathbf{r}_0 when the particle is closest to the origin. From section (3.1) the Coriolis force \mathbf{F}_{Cor} and the centrifugal force \mathbf{F}_{cent} expressed in vector notation are

$$\mathbf{F}_{\text{Cor}} = -2(\text{Re}[i\dot{z}], \text{Im}[i\dot{z}]) = 2u\mathbf{n} \quad (3.65)$$

$$\mathbf{F}_{\text{cent}} = (\text{Re}z, \text{Im}z) = \mathbf{r} \quad (3.66)$$

where $u(\mathbf{r})$ is the speed of the particle at position \mathbf{r} and \mathbf{n} is the normal to the trajectory as shown in figure (3.6.2).

At \mathbf{r}_0 the two forces act in parallel. If the particle is moving clockwise at this point then the forces act in opposite directions and we have three cases:

- (i). $\mathbf{F}_{\text{Cor}} > \mathbf{F}_{\text{cent}}$ at \mathbf{r}_0 . Then the trajectory has the same sign of curvature for all motion, and the curve is always convex.
- (ii). $\mathbf{F}_{\text{Cor}} < \mathbf{F}_{\text{cent}}$ at \mathbf{r}_0 . Then the curvature changes sign near \mathbf{r}_0 and is negative (concave) at \mathbf{r}_0 .

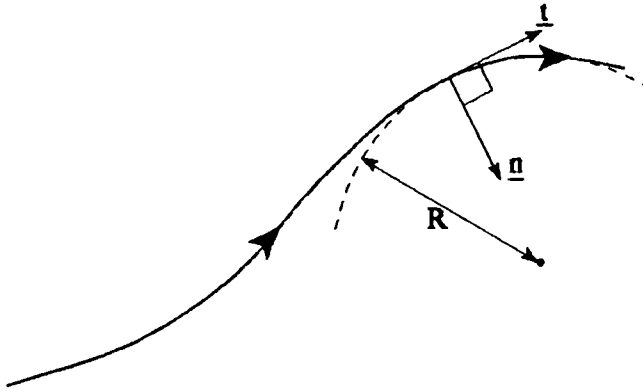


Figure 3.6.2. Trajectory showing unit tangent vector \mathbf{t} , unit normal vector \mathbf{n} , and radius of curvature R .

(iii). $\mathbf{F}_{\text{Cor}} = 0$ at \mathbf{r}_0 . There is a cusp at \mathbf{r}_0 which is also at the boundary of the energetically forbidden region.

If the particle is moving anti-clockwise the forces act in the same direction and there is just one case:

(iv). $\mathbf{F}_{\text{Cor}} \cdot \mathbf{F}_{\text{cent}} > 0$ at \mathbf{r}_0 . There exists a loop in the trajectory passing through \mathbf{r}_0 .

It is this fourth case with which we are interested in this section, as it leads to the possibility of trajectories which hit the edge of the circle tangentially, which we shall call glancing trajectories. In the rotating circle they can only occur when the impact is in the clockwise direction with $\psi = \pi$ and only when the radius of curvature of the trajectory is less than that of the boundary. For example consider a set of trajectories starting from the same point on the boundary, but at any angle ψ_0 between 0 and π . A typical set is shown in figure (3.6.3).

There are three groups of trajectories here. Some trajectories have ‘looped’ and split off from the main group and a third group breaks off after this. It can be seen that these groups are separated by trajectories which just glance the edge of the circle (at P and Q) and it is these which cause the discontinuities in the angle θ_1 . Figure (3.6.4) shows the group of trajectories as a vertical line in the (θ_0, ψ_0) plane which is mapped onto three disconnected curves in the (θ_1, ψ_1) plane.

Here we see that an important source of the chaotic motion is the set of

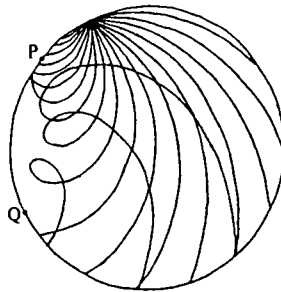


Figure 3.6.3. A set of trajectories originating from the one point with the same energy, illustrating the discontinuity in position of the next bounce due to the glancing points P and Q .

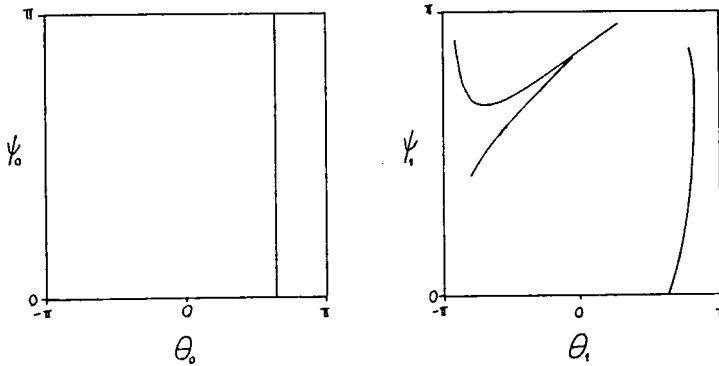


Figure 3.6.4. First iteration of the Poincaré map for the set of trajectories in figure (3.6.3).

discontinuities in the map F . The mechanism that produces it is purely the curvature of the trajectories, a feature previously studied only in the case of magnetic fields [28]. However, there the picture has other effects due to variations and discontinuities in the curvature of the boundary. These glancing trajectories are a major factor in determining whether the system exhibits chaos, because they mark the points where nearby trajectories diverge. In particular, the kind of chaos associated with them seems to be ergodic and mixing rather than the weaker ‘quasi-integrable’ (as defined by Berry in [24]). These special trajectories can only occur if the radius of curvature R of the trajectory at the boundary is less than the radius of the circle. We follow the same method as [60]. In terms

of the tangential component and the normal component the acceleration of the particle is given by

$$\ddot{\mathbf{r}} = \frac{dv}{dt} \mathbf{t} + \frac{v^2}{R} \mathbf{n} \quad (3.67)$$

where \mathbf{t} and \mathbf{n} are the unit vectors shown in figure (3.6.2). The normal component is also

$$(\mathbf{F}_{\text{Cor}} + \mathbf{F}_{\text{cent}}) \cdot \mathbf{n}.$$

Hence

$$R = \frac{v^2}{2v + \mathbf{r} \cdot \mathbf{n}}. \quad (3.68)$$

At the boundary of the circle \mathbf{n} is parallel with the outward normal to the circle but may be in the opposite direction. If they are in the same direction the trajectory would curve in the opposite direction to the boundary. So the particle must be travelling in the clockwise sense with \mathbf{n} acting inwards, giving $\mathbf{r} \cdot \mathbf{n} = 1 + \cos \theta = \frac{1}{2}r^2$. Also, from energy conservation $v^2 = 2E + r^2$ so

$$R = \frac{2E + r^2}{2\sqrt{2E + r^2 - \frac{1}{2}r^2}}. \quad (3.69)$$

For glancing trajectories to occur we require that $0 \leq R < 1$, giving

$$4E^2 + 4E\left(\frac{3}{2}r^2 - 2\right) + \frac{9}{4}r^4 - 4r^2 < 0. \quad (3.70)$$

Using $r^2 = 2(1 + \cos \theta)$, this gives the limits for $\cos \theta$ as follows

$$-\frac{5}{9} - \frac{2}{3}E - \frac{4}{9}\sqrt{1 + \frac{3}{2}E} < \cos \theta < -\frac{5}{9} - \frac{2}{3}E + \frac{4}{9}\sqrt{1 + \frac{3}{2}E}. \quad (3.71)$$

This requires that $E > -\frac{2}{3}$ because otherwise the LHS of equation (3.70) is positive definite. When the upper limit for $\cos \theta$ is -1 , the maximum value of the energy for glancing occurs at $E = 2$. Thus there are several regimes. For $-\frac{2}{3} < E < 0$ there are two intervals for θ in which glancing trajectories can occur, one below and one above the x axis. For $0 < E < 2$ there is just

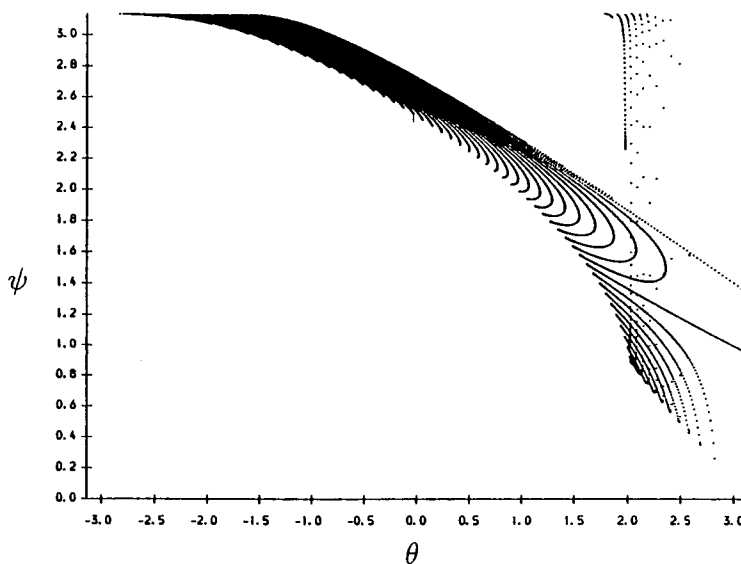


Figure 3.6.5. Pre-image of glancing trajectories in the energy range $-\frac{2}{3} < E < 2$.

one interval passing through $\cos \theta = -1$. This interval decreases in length and disappears at $E = 2$.

For the range of energies $-\frac{2}{3} < E < 2$ the pre-image of the glancing trajectories were plotted in figure (3.6.5), which shows the line discontinuities in the first iteration of the map. At $E = -\frac{2}{3}$ there are two points at $\theta = \pm(\pi - \cos^{-1}(\frac{1}{9}))$ from which the line discontinuities originate. As E increases these grow in length and join at $E = 0$; the single curve then decreases in length and disappears at $\theta = -\pi, \psi = \pi, E = 2$. For some of these energies we have also plotted in figure (3.6.6) the first iteration of the map for points on a hashed grid made up of horizontal and vertical lines in (θ, ψ) space. The image shows the effect of the discontinuities of the map. There is a large distortion near the discontinuities in the middle of the interval $-\frac{2}{3} < E < 2$. It can thus been seen how the glancing trajectories and the discontinuities they produce are an important source of chaotic motion.

Within the range $-\frac{2}{3} < E < 2$ we expect the number of disconnected chaotic regions to be less, but that these will be larger so that a chaotic trajectory will visit a larger region of phase space. We expect this because invariant curves, which normally separate chaotic regions by forming bands across the Poincaré surface or rings about the fixed point, will be broken by the discontinuities,

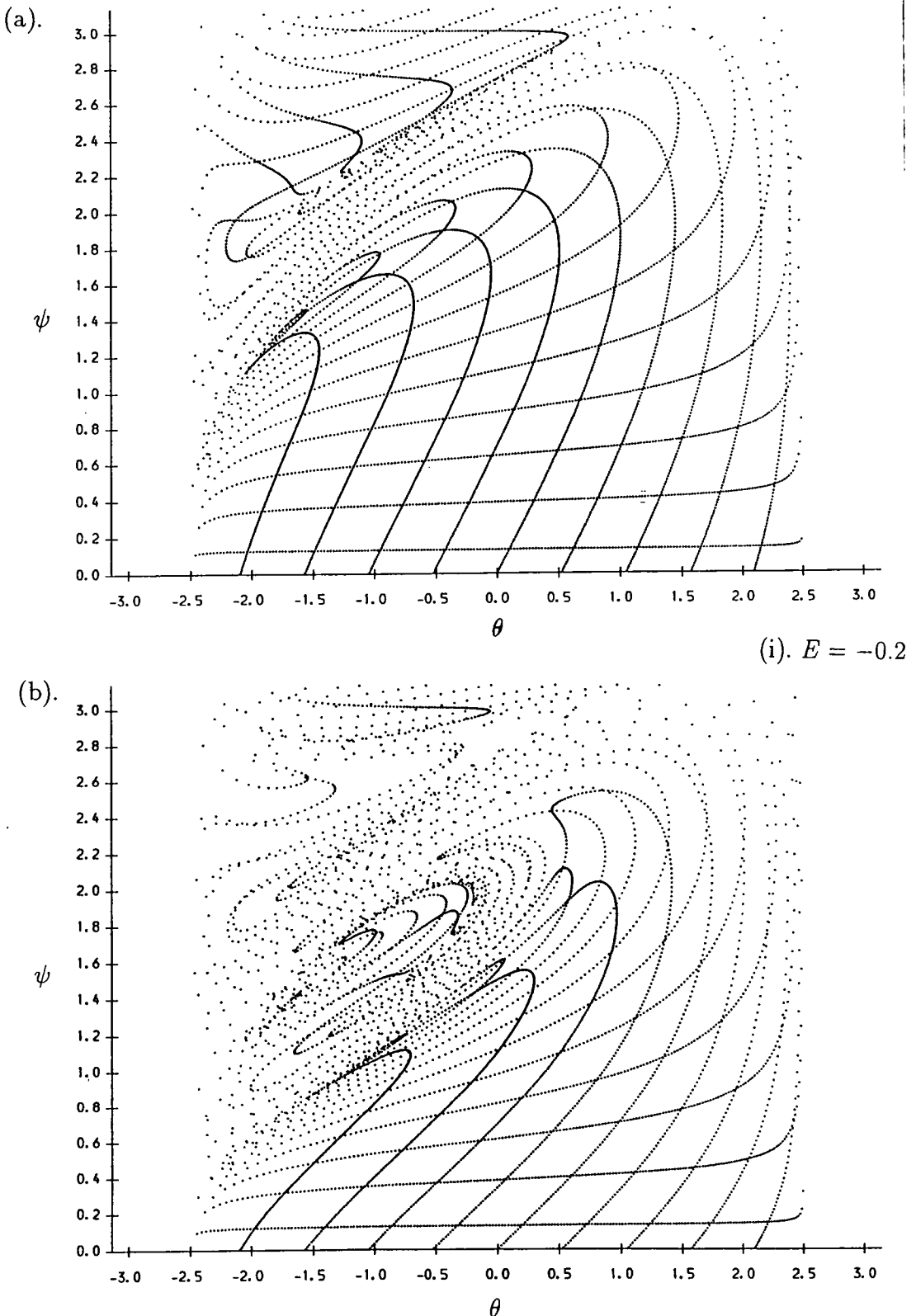


Figure 3.6.6. Poincaré map showing the effect of the discontinuities of figure (3.6.5) after (a) first iteration, (b) second iteration. (i). $E = -0.2$, (ii). $E = 0.1$. (iii). $E = 1$, (iv). $E = 2$.

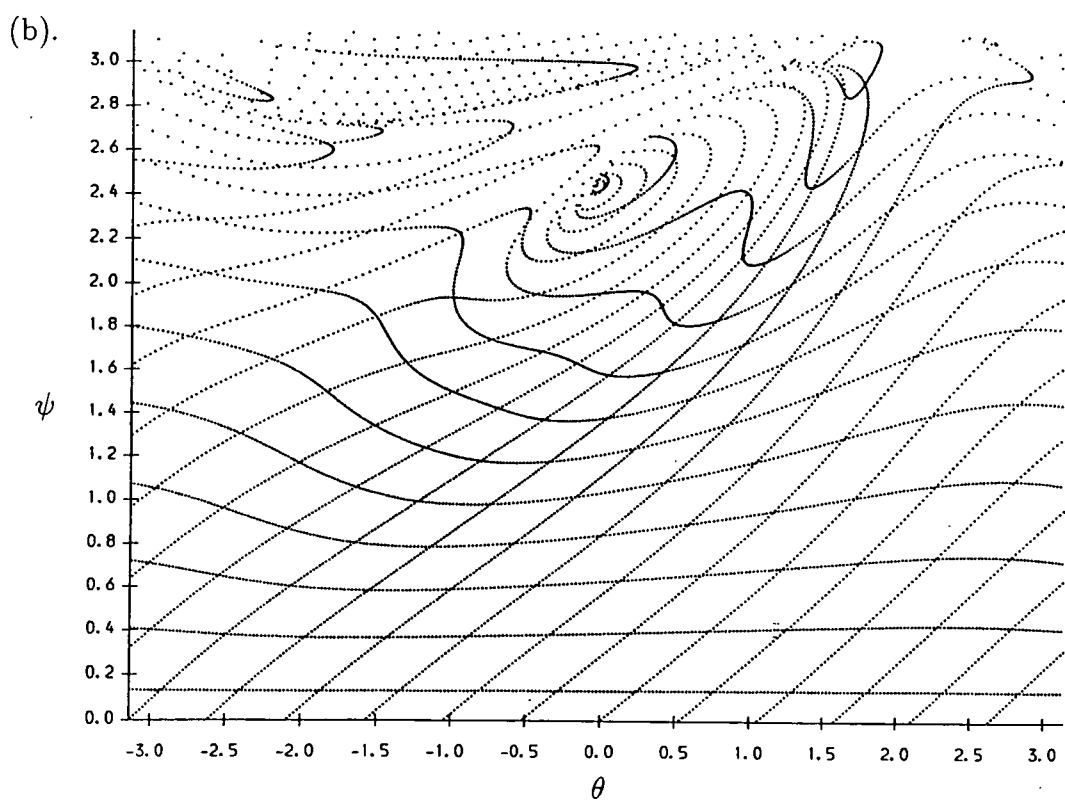
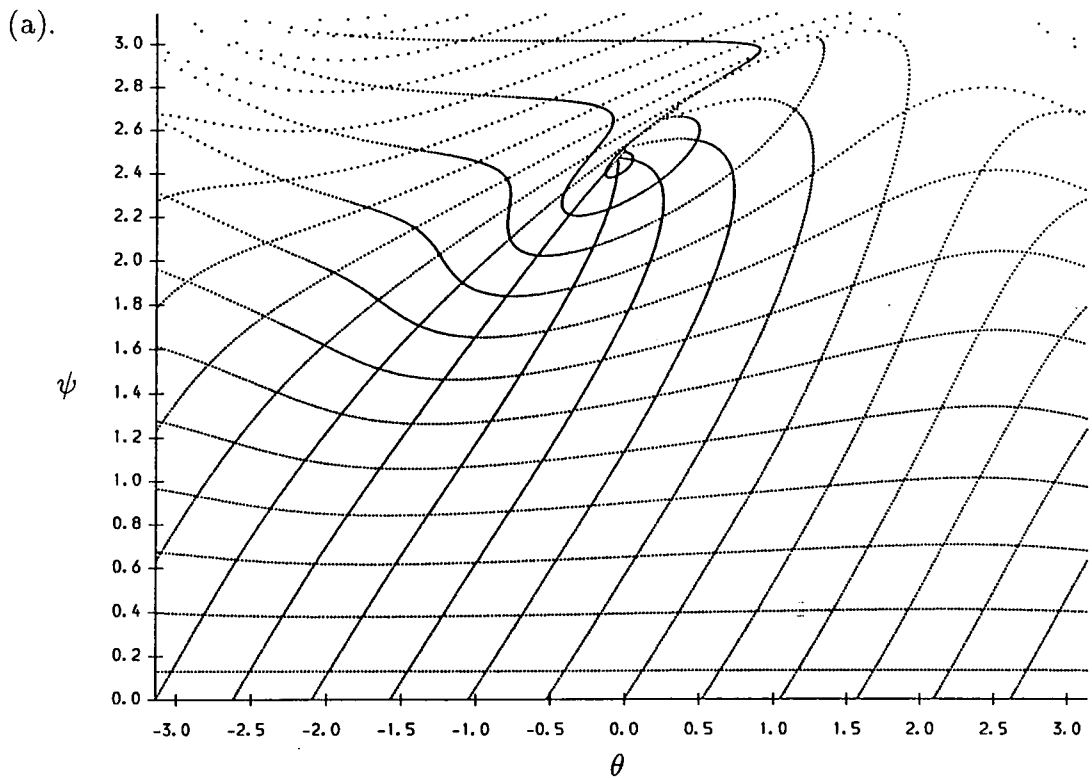


Figure 3.6.6. (continued) (ii). $E = 0.1$

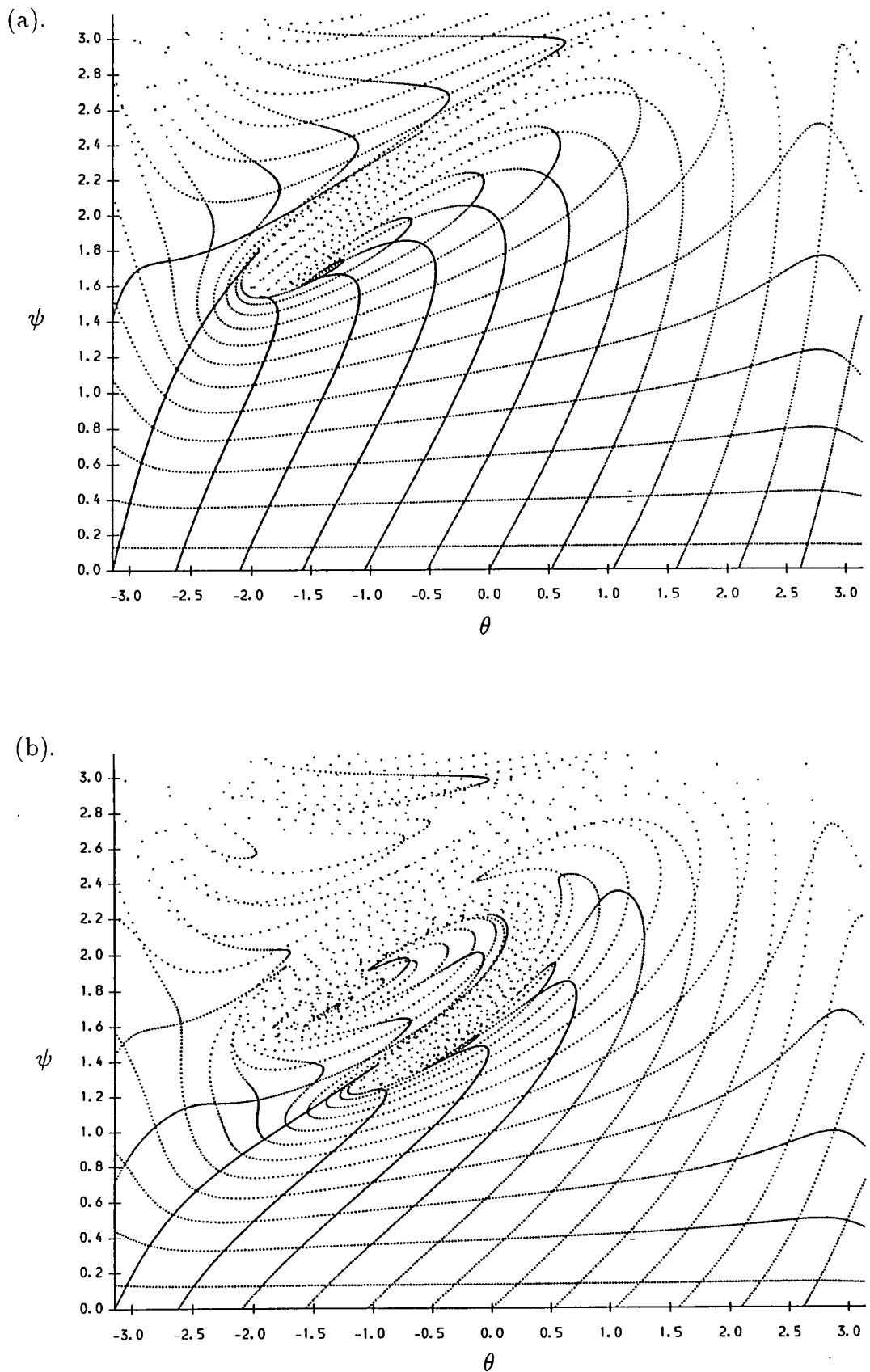


Figure 3.6.6. (continued) (iii). $E = 1$

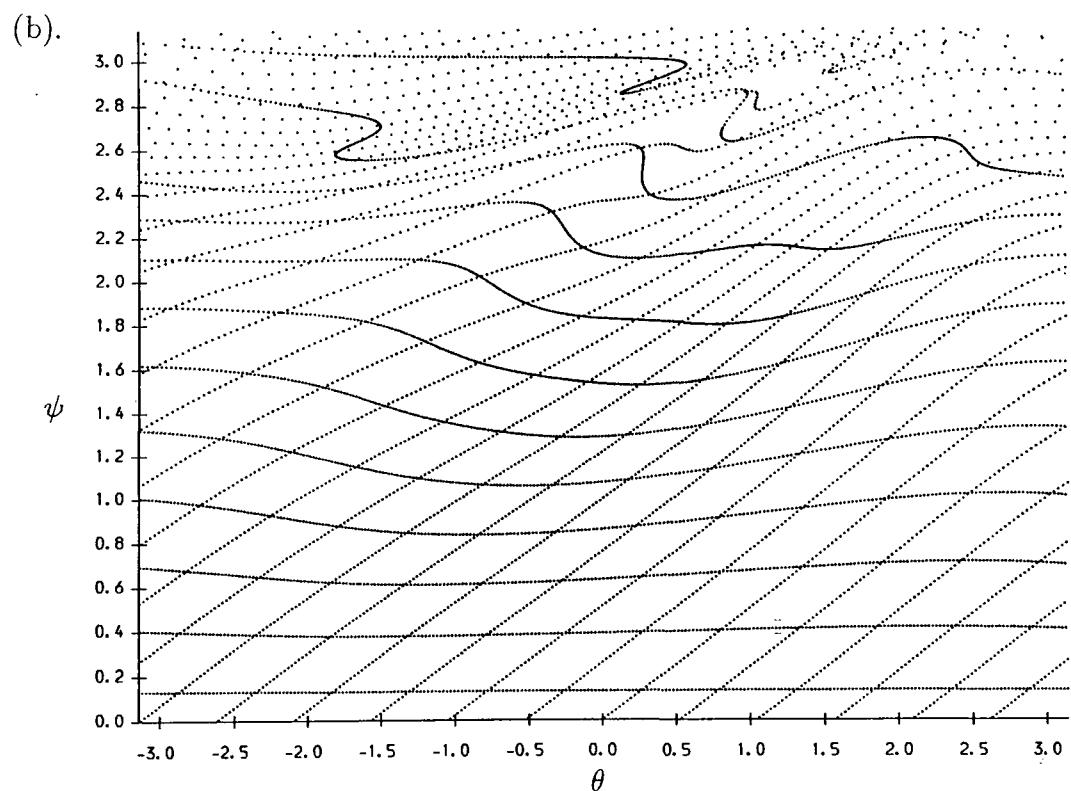
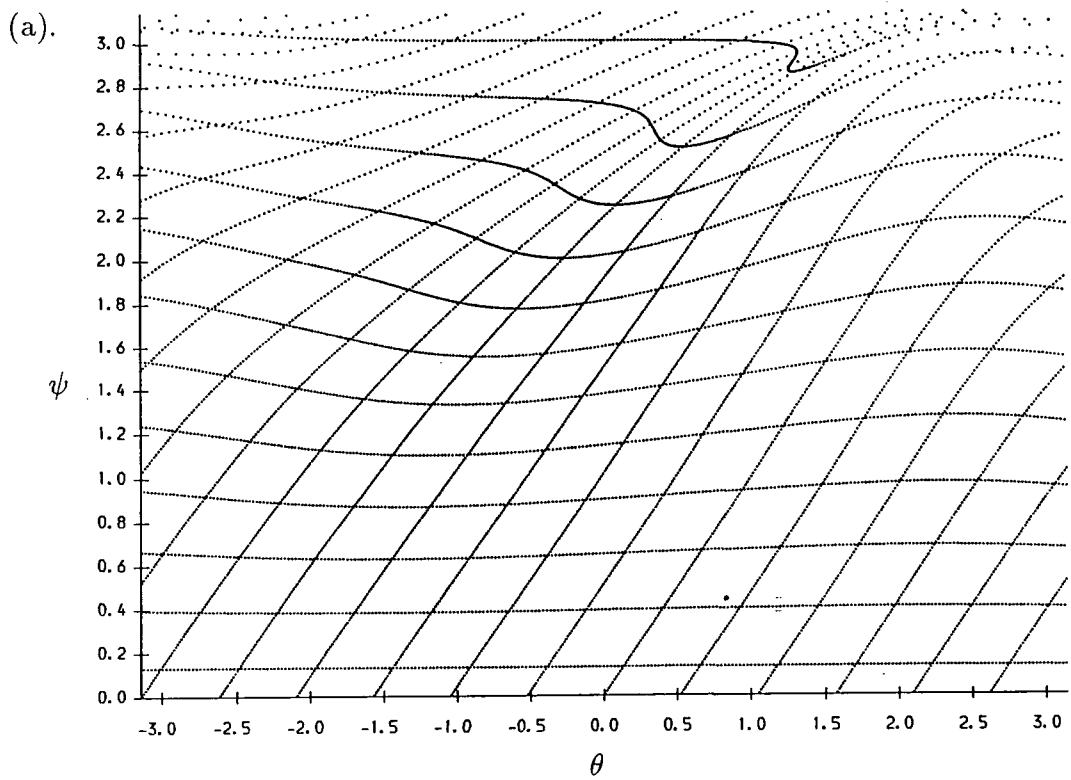


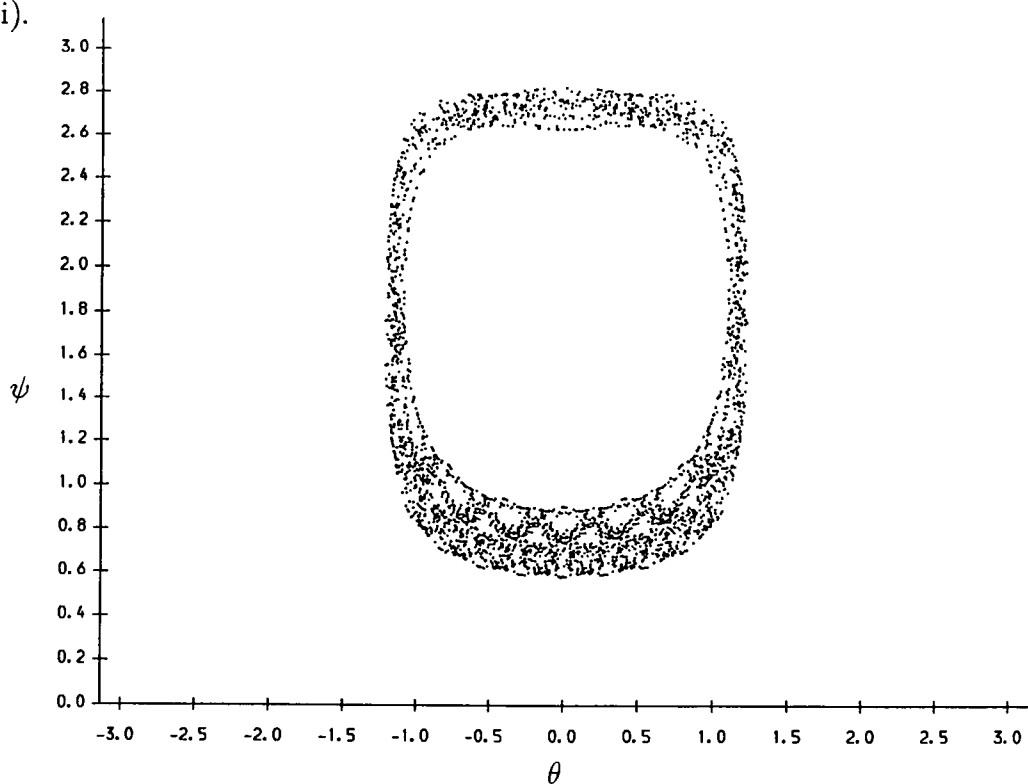
Figure 3.6.6. (continued) (iv). $E = 2$.

allowing the chaotic regions above and below these curves to merge. These invariant curves are indeed destroyed in this energy range, as shown by following one chaotic trajectory for many iterations and looking at the region in which it resides (figure (3.6.7), also figure (3.5.2)). However these curves are still found to be destroyed for energies just outside this range ($E = 2.5$ and $E = -0.75$), although for energies further outside ($E = 3.0$ and $E = -1.25$) they reappear. Thus there does not need to be discontinuities for these invariant curves to be broken. We still maintain that the discontinuities are the main factor in producing ergodicity for some values of the energy, but that there is still merging of chaotic regions when the Poincaré map is continuous (*i.e.* outside the range of energies for which there exist glancing trajectories).

There is another important set of trajectories which we have not discussed so far. These are the sliding trajectories which occur when the particle is travelling tangentially and cannot reflect off the edge, because the radius of curvature of the trajectory is greater than the radius of the circle or in the opp sense. This is exactly the opposite regime to the glancing trajectories. The possibilities are shown in figure (3.6.8). When $-2 < E < -\frac{2}{3}$ the particle slides in both directions for all allowable θ , but the motion is reversed at $\theta = \pm \cos^{-1}(-E-1)$. For $-\frac{2}{3} < E < 0$ the anti-clockwise motion is the same as before, but after reflection it leaves the edge at a special glancing point where $R = 1$, *i.e.* at $\theta = \cos^{-1}(-\frac{5}{9} - \frac{2}{3}E - \frac{4}{9}\sqrt{1 + \frac{3}{2}E})$. By TS_x symmetry it enters this trajectory at another special glancing point where $\theta = -\cos^{-1}(-\frac{5}{9} - \frac{2}{3}E - \frac{4}{9}\sqrt{1 + \frac{3}{2}E})$. For the clockwise motion the particle enters the sliding motion at $\theta = \cos^{-1}(-\frac{5}{9} - \frac{2}{3}E + \frac{4}{9}\sqrt{1 + \frac{3}{2}E})$ and leaves it at $\theta = -\cos^{-1}(-\frac{5}{9} - \frac{2}{3}E + \frac{4}{9}\sqrt{1 + \frac{3}{2}E})$. For $0 < E < 2$ the anticlockwise trajectory is a complete circle, and the clockwise motion is the same as for $-\frac{2}{3} < E < 0$. For $E > 2$ the trajectories are complete circles in both directions.

The sliding trajectories are special cases of periodic orbits. For $E > 2$ the sliding trajectories are two continuous bands at $\psi = 0$ and $\psi = \pi$. It is the influence of the stability of these orbits which give rise to the quasi-periodic bands seen between $\psi = 0$ and $\psi = \pi$. For $E < -\frac{2}{3}$ the back and forth sliding motion between $-\cos^{-1}(-E-1) < \theta < \cos^{-1}(-E-1)$ gives a rectangular orbit

(i).



(ii).

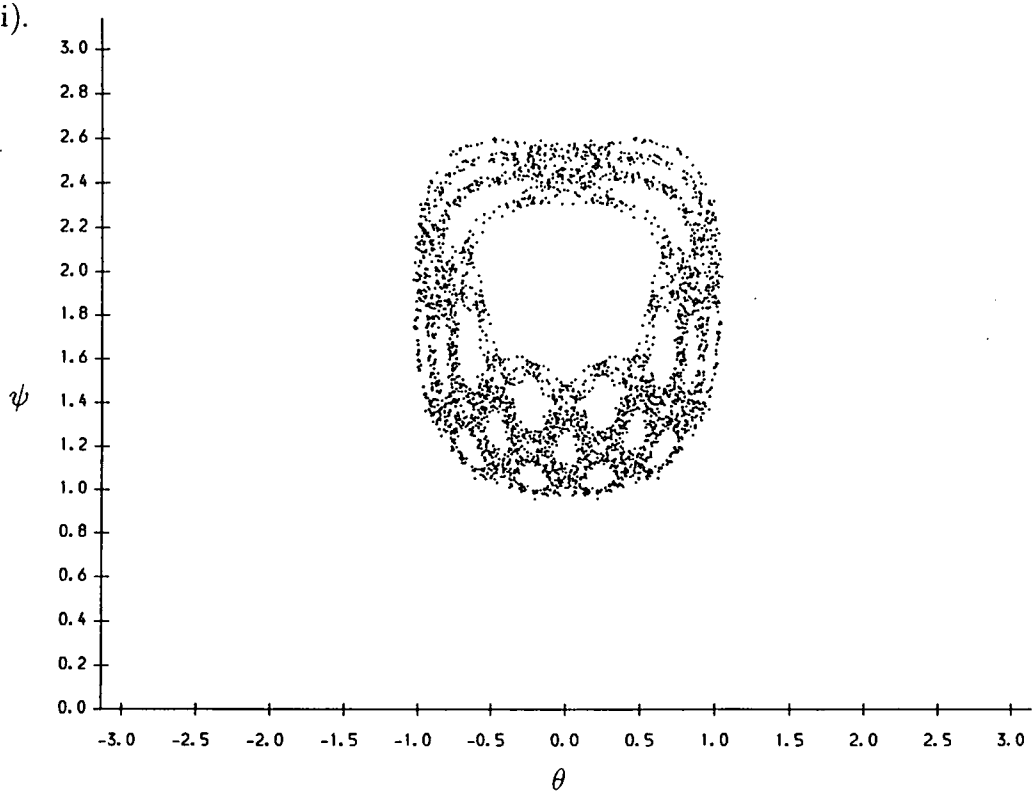
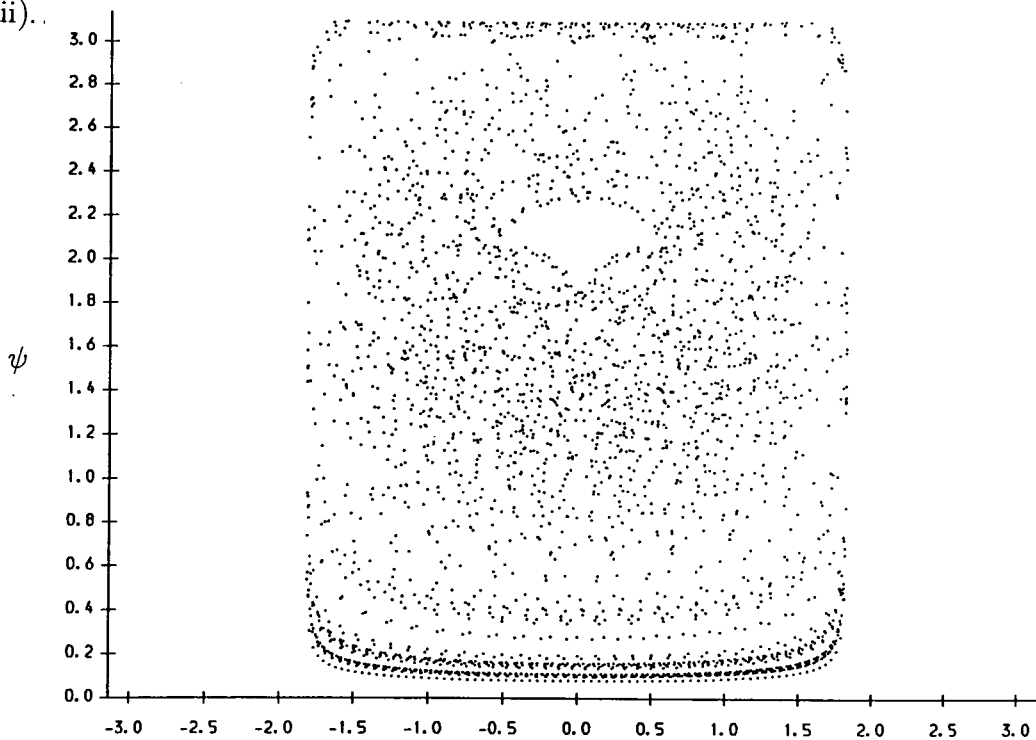


Figure 3.6.7. Poincaré maps for one trajectory followed for 3000 bounces. (i). $E = -1.25, \theta_0 = 0, \psi_0 = 0.7$, (ii). $E = -1.25, \theta_0 = 0, \psi_0 = 1.4$.

(iii).



(iv).

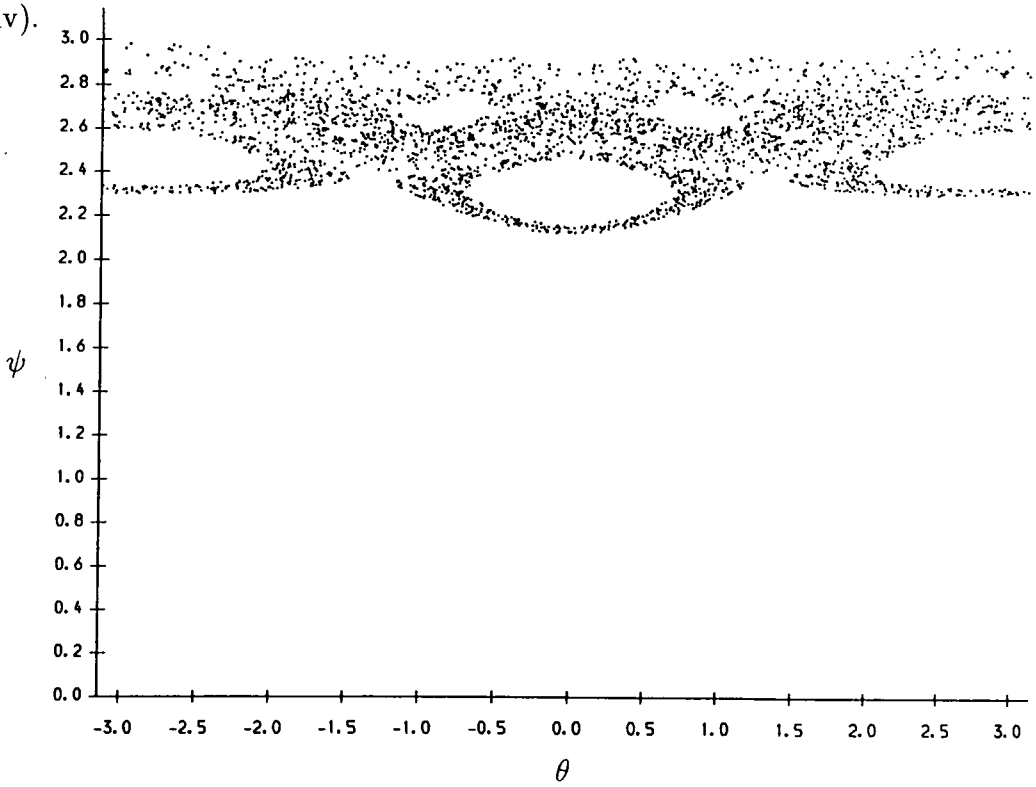


Figure 3.6.7. (continued) (iii). $E = -0.75$, $\theta_0 = 0$, $\psi_0 = 0.1$, (iv). $E = 2.5$, $\theta_0 = 1.5$, $\psi_0 = 2.7$,

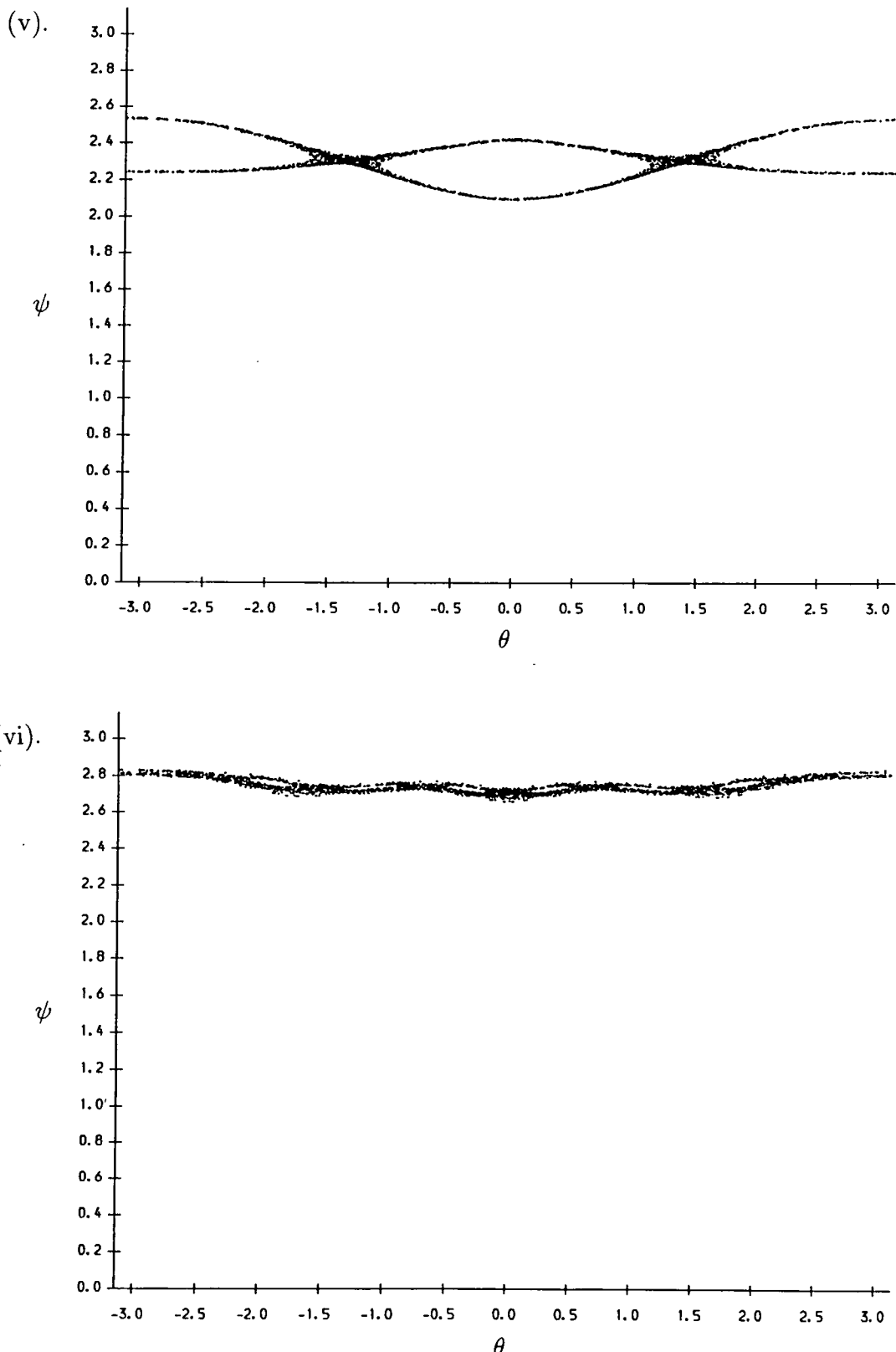


Figure 3.6.7. (continued) (v). $E = 3$, $\theta_0 = 1.5$, $\psi_0 = 2.3$, (vi). $E = 3$, $\theta_0 = 1.5$, $\psi_0 = 2.7$.

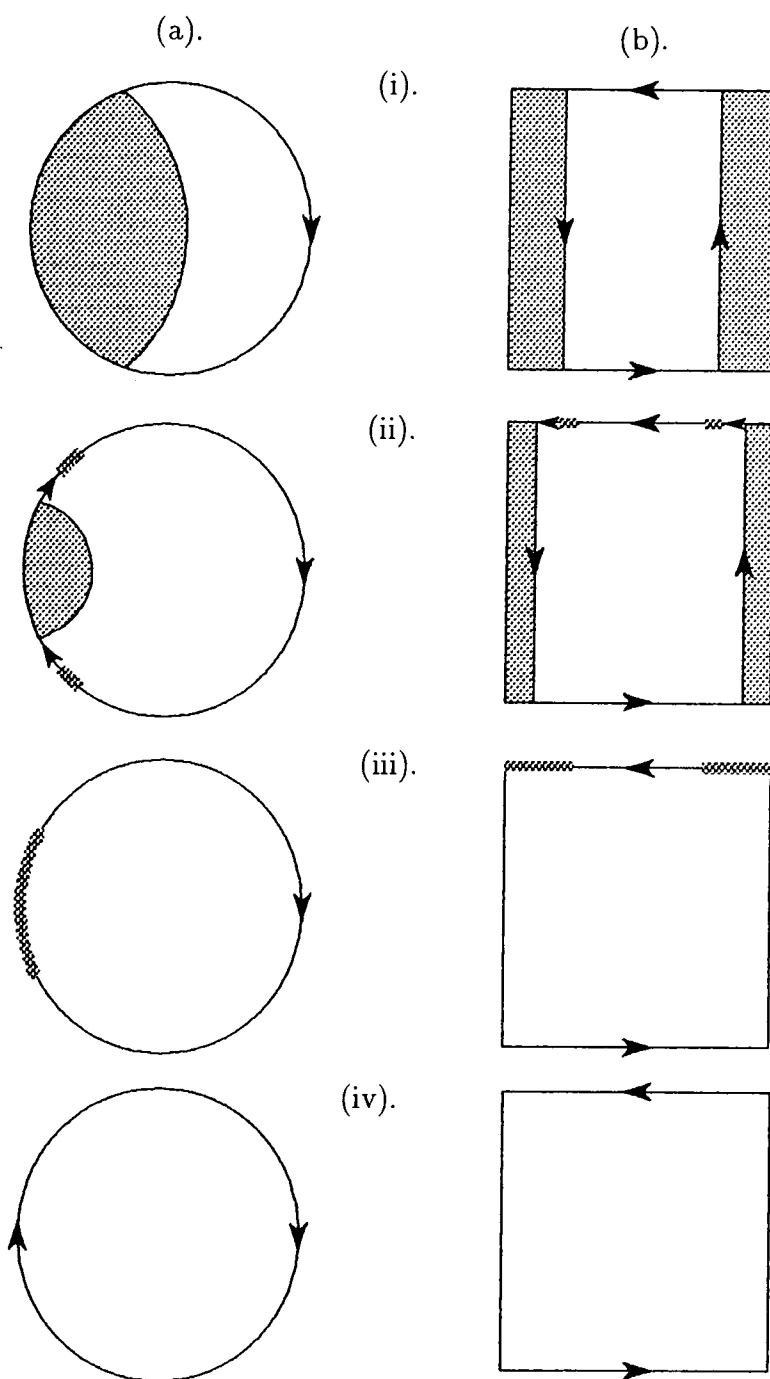


Figure 3.6.8. Sliding motion (a) in billiard plane, (b) in Poincaré section for (i).
 $E < -\frac{2}{3}$, (ii). $-\frac{2}{3} < E < 0$, (iii). $0 < E < 2$, (iv). $E > 2$. Shaded regions indicate forbidden zones; shaded curves indicate glancing regions of boundary.

in the Poincaré map, which surrounds the fixed point and is its counterpart. For $-\frac{2}{3} < E < 0$ the anticlockwise and clockwise sliding trajectories are parts of chaotic trajectories which enter into the midst of the phase space and seem to pass through all the chaotic region. For $0 < E < 2$ only the clockwise trajectory is still chaotic, and the stability of the anticlockwise trajectory accounts for chaotic motion being restricted to the upper half of the Poincaré map. As the energy approaches $E = -\frac{2}{3}$ from below and $E = 2$ from above we can see that the stability of the periodic motion of the sliding trajectories is reduced, and this accounts for the destruction of the quasi-periodic invariant bands and rings below and above these limits respectively. Thus although we do not require there to be discontinuities in the map for these invariant curves to be destroyed, it appears that an approach towards such maps is helpful, because they are associated with the stability of important periodic motion.

Thus an examination of glancing and sliding trajectories has accounted for some of the main features of the motion.

3.7 Lyapunov Exponents and Chaotic Volume

The Lyapunov exponent $\Lambda(x)$ is a convenient measure of the degree of chaos in the neighbourhood of a trajectory $x(t)$ (here $x = (\mathbf{p}, \mathbf{r})$). It measures the local divergence of nearby trajectories. For a system with N degrees of freedom in $2N$ -dimensional phase space, we consider a volume element on the $(2N - 1)$ -dimensional energy hypersurface. At a small time δt later this volume element will be translated and deformed. The eigenvalues σ_i of the linearised deformation tensor (the tangent map) give how much the volume element shrinks or stretches along each of its principal axes, the growth factor being locally $\sigma_i = \exp(\lambda_i \delta t)$ for the i th axis. For a conservative system the volume element is unchanged in volume, so $\sum \lambda_i = 0$. Over a period of time, the volume element will either remain compact, because growth and contraction in each direction averages to zero over a long period of time, or the deformity will grow exponentially along some of the principal axes and shrink exponentially along the others. The former case is regular motion and the latter is chaotic motion, where the maximal exponent of the growth in the limit $t \rightarrow \infty$ is defined to be the Lyapunov

exponent. That is, suppose D_t is the maximum diameter of the volume element $\delta V(t)$ at time t and D_0 is this diameter at $t = 0$, then we define the Lyapunov exponent of the trajectory $x(t)$ in the centre of δV to be

$$\Lambda(x) = \lim_{t \rightarrow \infty} \lim_{\delta V \rightarrow 0} \frac{1}{t} \log \left(\frac{D_t}{D_0} \right) \quad (3.72)$$

It is not necessary in practice to know a priori in which direction D_0 is; the smaller exponential growths in other directions will be negligible compared to the maximal growth, and hence the initial diameter can be taken in almost any direction.

We use the standard method of Bennetin and Strelcyn [61] for calculating $\Lambda(x)$, which is better for discrete maps. We consider two nearby trajectories distance D_0 apart, and measure their separation D_1 after the first bounce. Rather than continuing with these two trajectories we change the second for one which is a distance D_0 from the first, but whose separation vector is in the same direction. We then measure their separation D_2 at the second bounce, replace this by D_0 and keep on going for several bounces. Suppose D_i is the separation after the i th bounce, then $\Lambda(x)$ can be written as

$$\Lambda(x) = \lim_{n \rightarrow \infty} \frac{1}{n} \sum_{i=1}^n \log(D_i/D_0). \quad (3.73)$$

Let $\Lambda_n(x)$ be the value of Λ before the limit is taken. We have found numerically that $\Lambda_n(x)$ is independent of the length (for $10^{-12} < D_0 < 10^{-6}$) and direction of the initial separation vector, but that small fluctuations in Λ are observed (of approximately 3%) as it approaches its limiting value even after 10000 reflections. This is in agreement with the work of Bennetin and Strelcyn.

For the rotating billiard problem, the trajectory $x(t)$ is given in terms of its polar position (r, θ) from the centre of the circle, and the speed and direction of its motion. Conservation of energy restricts the trajectory to three dimensions, and so at each bounce v is a function of theta only:

$$v^2(\theta) = 2(\cos \theta + E + 1). \quad (3.74)$$

The length ds of a line segment in phase space is thus given by

$$ds^2 = \left(1 + \frac{\sin^2 \theta}{v^2}\right) d\theta^2 + v^2 d\psi^2. \quad (3.75)$$

The Lyapunov exponent measures very clearly whether a trajectory belongs to a regular region or a chaotic one, and how chaotic that region is. If the limiting value is zero (numerically set to some cut-off point) then the region is regular, otherwise it is chaotic. Negative Λ 's are never found for Hamiltonian systems because the sum of the characteristic exponents is always zero, so the maximal exponent is always positive.

The chaotic volume $\chi(E)$ is defined as the proportion of classically accessible phase space M which is chaotic; mathematically,

$$\chi(E) = \frac{\int_M \Theta(\Lambda(\theta, \psi)) d\mu}{\int_M d\mu}, \quad (3.76)$$

where Θ is the Heaviside step function and μ is the Liouville measure of the flow. Using equation (3.75) we find

$$d\mu = (v^2 + \sin^2 \theta)^{\frac{1}{2}} d\theta d\psi. \quad (3.77)$$

To calculate χ , a Monte-Carlo method is used. A uniform distribution of random points in (θ, ψ) space is chosen. The Lyapunov exponent is calculated for each trajectory starting at these points, and if $\Lambda > 0.05$ it is accepted as chaotic. The Monte-Carlo estimate is

$$\int_M f(\theta, \psi) d\theta d\psi \approx \text{Vol}(M) \left(\langle f \rangle \pm \sqrt{\frac{\langle f^2 \rangle - \langle f \rangle^2}{N_{MC}}} \right), \quad (3.78)$$

where N_{MC} is the number of Lyapunov exponents sampled, and $\langle f \rangle$ denotes the mean value of f . The numerator of (3.76) was calculated using this. The denominator was found by the same method, and it was also calculated by a quadrature method in order to test the Monte-Carlo method for accuracy.

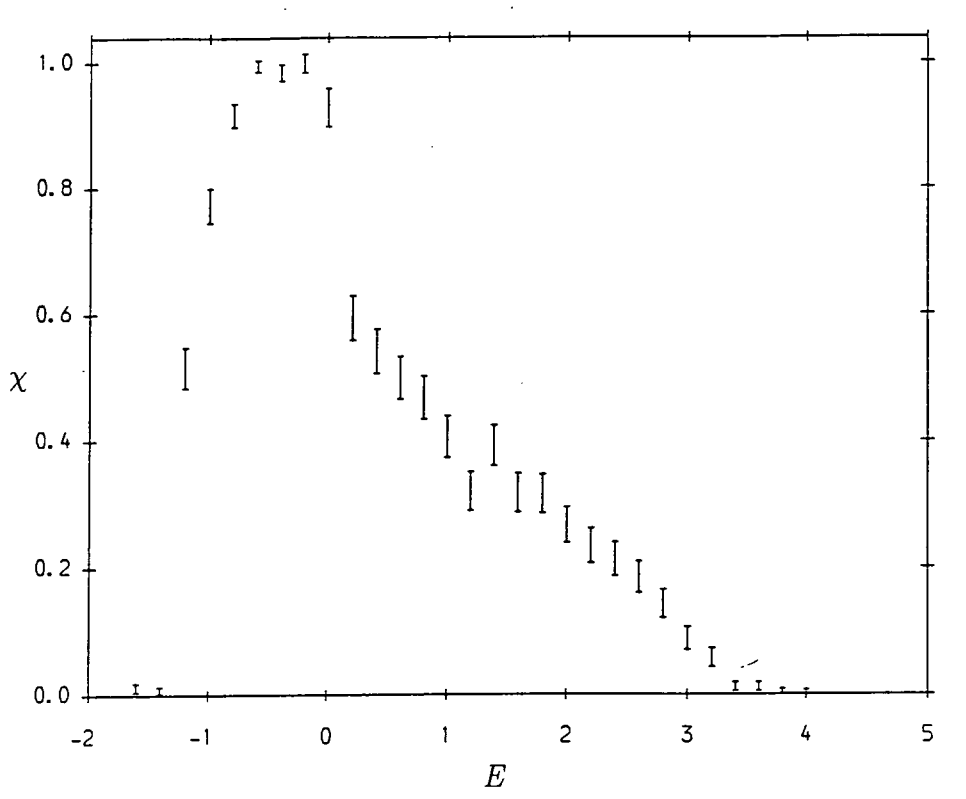


Figure 3.7.1. Chaotic volume χ versus energy E for the rotating circle.

For each energy E , Lyapunov exponents for 250 orbits were calculated using 300 bounces for each orbit. The resulting graph is plotted in figure (3.7.1). The statistical error from the Monte-Carlo integration is much larger than the systematic error due to evaluating $\Lambda(x)$ for this number of bounces, so the error bars are two standard deviations thick as evaluated by the Monte-Carlo method.

The graph shows clearly the approach to integrable motion in the limits $E \rightarrow -2$ and $E \rightarrow \infty$, and the ergodic motion near $-\frac{2}{3} < E < 0$. The chaotic volume does have the disadvantage that it does not give any indication of the number of separate chaotic regions. It would perhaps be better to calculate the chaotic volume for each chaotic region. For this one would have to either use the fact that the Lyapunov exponent is the same throughout a single chaotic region and different between regions, or use several trajectories to separate the phase space into several regions before calculating Lyapunov exponents. The advantage of the latter method would be that then only one Lyapunov exponent need be calculated, and the chaotic volume for the region could then be calculated from this and the size of the chaotic region.

In this section we have not described the Kolmogorov entropy. This is because the level statistics for the quantum mechanical problem of a classical completely chaotic system do not depend on the strength of mixing, but only that there is mixing. Thus the simplest assumption is that when there are some regular and some chaotic regions there will again be no dependence on the Kolmogorov entropy. The chaotic volume appears to be the most natural alternative.

4. Quantum Billiards in a Rotating Boundary

4.1 General Rotating Billiards

There are many reasons why rotating billiards are good systems to study quantum mechanically. Firstly, the classical mechanics show strong chaotic motion for a good range of energies, and almost integrable motion for very small and very large energies, making the study of the transition from integrability to chaos possible. Secondly, the boundary can be simple, because the chaotic motion is due purely to the rotation, so computations are easier to implement than, for example, the stadium billiard. Thirdly, if the boundary does not have reflectional symmetry, the system is time-reversal breaking, and the relation to random matrix theory for GUE statistics can be tested. Fourthly, rotating systems are relevant to nuclear physics—they are two-dimensional examples of the model of Inglis [62], which was used to analyse the nucleonic response to the rotation of the nuclear field.

We will be considering conservative systems with the Schrödinger equation

$$\hat{H}\Psi = i\hbar \frac{\partial\Psi}{\partial t}, \quad (4.1)$$

whose solutions are $\Psi = \sum_i a_i \psi_i(x) \exp(iE_i t)$, where

$$\hat{H}\psi_i = E_i\psi_i. \quad (4.2)$$

The technique we use to solve equation (4.2) is the Rayleigh-Ritz variational method, using a truncated set of orthonormal basis functions ϕ_i satisfying

$$\int \phi_i^* \phi_j d^N q = \delta_{ij} \quad (4.3)$$

$\phi_i(q) = 0 \quad \text{on boundary.}$

In the Rayleigh-Ritz method, a functional $I(\psi_i^M) = I(\sum_{r=1}^M c_r^{(i)} \phi_r)$ is minimised over ϕ_r , where ψ_i^M is an approximation to the true ψ_i using the truncated basis ϕ_i for $i = 1, \dots, M$ and M is the size of the truncated basis. . The

minimalisation is the solution of the eigenvalue problem,

$$H_{ij}^M \psi_j^M = E_i^M \psi_i^M, \quad (4.4)$$

where

$$H_{ij}^M = \int \phi_j^* \nabla^2 \phi_i d^N q \quad \text{for } i, j = 1, \dots, M. \quad (4.5)$$

The matrices which diagonalise H_{ij} being the coefficients $c_r^{(i)}$. The eigenvalues E_i^M satisfy

$$E_i^M \geq E_i, \quad (4.6)$$

and are the best upper bound on E_i using the truncated basis. This is an extension of the variational method used to obtain the ground state of a system, often found in undergraduate texts on quantum mechanics.

The Hamiltonian operator corresponding to equation (3.4) is

$$\hat{H} = -\frac{\hbar^2}{2m} \nabla^2 + i\omega\hbar\partial_\theta + U(x, y), \quad (4.7)$$

where $\mathbf{r} = (x, y) = (r \cos \theta, r \sin \theta)$, and $U(x, y)$ is the infinite potential well. This can be written as

$$\hat{H} = \frac{1}{2m} (-i\hbar\nabla - \mathbf{A})^2 + V(x, y) + U(x, y), \quad (4.8)$$

where

$$\mathbf{A} = \omega(-y, x), \quad (4.9)$$

$$V = -\frac{1}{2}m\omega^2(x^2 + y^2). \quad (4.10)$$

As before, we introduce some length scale ρ (which determines the size of the billiard) and rescale the problem $\mathbf{r} \mapsto \mathbf{r}/\rho$, $t \mapsto \omega t$, $H \mapsto H/m\rho^2\omega^2$, $\hbar \mapsto \hbar/m\rho^2\omega$ to obtain

$$\hat{H} = -\frac{\hbar^2}{2} \nabla^2 + i\hbar\partial_\theta + U(x, y). \quad (4.11)$$

Thus we see that \hat{H} depends on one parameter, \hbar for a particular choice of boundary. Unlike stationary billiards, we cannot scale \hat{H} to remove \hbar , because



the mechanics depend on the energy. We must therefore choose particular values of \hbar and find the energy eigenvalues, some of which may be in the chaotic energy range, and some in the integrable range. The problem with this technique is that we do not obtain eigenvalues which are associated with constant classical energy, and hence with the same phase space behaviour. One modification, suggested by Berry and used by Delande [63] is to find the eigenvalues of \hbar ; *i.e.* to regard the energy E as a parameter which we fix, and $\hat{\hbar}$ (not \hat{H}) as an operator whose eigenvalues we find from

$$\hat{\hbar}\psi_i = \hbar_i\psi_i. \quad (4.12)$$

This is a better method, we will shall discuss in a later chapter. Now we shall continue with solving equation (4.2). First, we rescale \hat{H} again to obtain

$$\hat{\mathcal{H}} = -\nabla^2 + 2i\alpha\partial_\theta + U(x, y), \quad (4.13)$$

where $\hat{\mathcal{H}} = 2\alpha^2\hat{H}$, $\alpha = 1/\hbar$. Equation (4.13) has the eigenvalues,

$$\hat{\mathcal{H}}\psi_i = \mathcal{E}_i\psi_i. \quad (4.14)$$

There are several boundaries that appear to be suitable for study. We shall only consider in detail one of these—the circular billiard, but other models are the rectangular billiard, and the circular sector.

(i). The Rectangular Billiard

We consider a rectangular billiard with sides of length 1 and a . The normalised basis functions to use are

$$\phi_i(x, y) = \frac{2}{\sqrt{a}} \sin\left(\frac{\pi mx}{a}\right) \sin(\pi ny), \quad (4.15)$$

which give matrix elements,

$$\begin{aligned}
\mathcal{H}_{ij} &= \langle j | \hat{\mathcal{H}} | i \rangle \\
&= \pi^2 \left(\frac{m^2}{a^2} + n^2 \right) \delta_{mm'} \delta_{nn'} \\
&+ \begin{cases} \frac{16i\alpha}{\pi^2} \frac{mm'nn'(1 - (-1)^{m+m'})(1 - (-1)^{n+n'})}{(m^2 - m'^2)(n^2 - n'^2)} \\ \times \left[\frac{a}{(m^2 - m'^2)} - \frac{1}{a(n^2 - n'^2)} \right] & \text{for } \begin{matrix} m \neq m' \\ n \neq n' \end{matrix} \\ -2i\alpha \frac{ann'}{(n^2 - n'^2)} \left(1 - (-1)^{n+n'} \right) & \text{for } \begin{matrix} m = m' \\ n \neq n' \end{matrix} \\ 2i\alpha \frac{mm'}{a(m^2 - m'^2)} \left(1 - (-1)^{m+m'} \right). & \text{for } \begin{matrix} m \neq m' \\ n = n' \end{matrix}. \end{cases} \quad (4.16)
\end{aligned}$$

This has been diagonalised numerically, but the convergence of the eigenvalues is bad as the size of the matrix was increased. We can see why this is by considering the off-diagonal terms and Gerschgorin's theorem:

Theorem. Let $A \in \mathbb{C}^n \times \mathbb{C}^n$. Then each eigenvalue of A lies in one of the Gerschgorin disks \mathcal{D}_i in the complex plane, defined by

$$\mathcal{D}_i = \left\{ \lambda : |\lambda - A_{ii}| \leq \sum_{j \neq i} |A_{ij}| \right\}, \quad i = 1, \dots, n.$$

Consider, for example, the elements \mathcal{H}_{ij} for $m = m'$, $n + n' = 2p + 1$ where p is a positive integer. Then

$$\left| \lambda - \pi^2 \left(\frac{m^2}{a^2} + n^2 \right) \right| \leq \mathcal{S}_{mn}^{(1)} + \mathcal{S}_{mn}^{(2)} + \sum_{\substack{n'=2p+1-n \\ p=0}}^{\infty} -4\alpha a \frac{nn'}{n^2 - n'^2}, \quad (4.17)$$

where $\mathcal{S}_{mn}^{(1)}$, $\mathcal{S}_{mn}^{(2)}$ are other sums which we are not interested in. Just consider the last sum, with n fixed and n' very large; then it is always greater than

$$\sum_{\substack{n'=2p+1-n \\ p=0}}^{\infty} -\frac{4\alpha an}{n'}, \quad (4.18)$$

which is divergent. Hence there is no guarantee that the method of diagonalising the matrix at any size will give the true eigenvalues to any accuracy. Thus with

this limitation, and without more promising basis functions, we will study the quantum mechanics of this example no further.

A preliminary investigation of the classical mechanics has been made. From the studies of the rotating circle, the rotating rectangle is expected to be more chaotic (because, with straight walls, the possibility of glancing trajectories is greater), and this is the case. There are however algorithmic difficulties with the rectangle: for the circle, the distance function $d(t) = 1 - |z - 1|$ was very simple—it has at most two zeros. But for the rectangle, there are four distance functions, one for each wall, and each one can have many zeros. We thus have to be very careful to find the first zero, testing for shallow minima, maxima of both the function and its derivative in order to correctly bracket the root for each wall, before taking the lowest t over all the walls. Secondly, the phase space is more complex—the sharp corners mean that it is a patchwork of pieces joined in a jagged fashion. If the particle hits the corner exactly, it is reflected straight back.

(b). The Rotating Sector

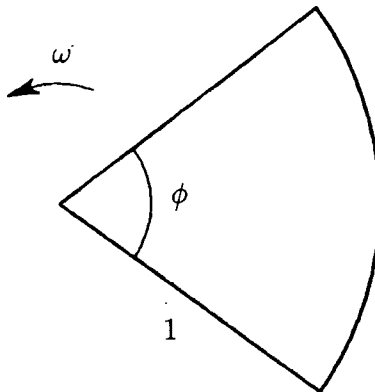


Figure 4.1.1. The rotating sector billiard.

This is a sector of a circle of radius 1, angle ϕ subtended at the centre, rotating about the point of the wedge (figure (4.1.1)). The rotating sector uses the rotational symmetry of the $2i\alpha\partial_\theta$ term to advantage. The symmetry of the circle, of which the sector is a part, is centred at the same point as the $2i\alpha\partial_\theta$ term, so this simplifies the Hamiltonian matrix.

Using the basis functions

$$\phi_{ml} = N_{ml} J_m(\lambda_{ml} r) \sin(m\theta), \quad (4.19)$$

where $m = p\pi/\phi$ (integer p), and λ_{ml} is the l^{th} zero of the m^{th} Bessel function, and

$$N_{ml} = \frac{2}{|J'_m(\lambda_{ml})|\sqrt{\phi}} \quad \text{for } m > 0, \quad (4.20)$$

gives

$$\begin{aligned} \mathcal{H}_{ij} &= \lambda_{ml}^2 \delta_{mm'} \delta_{ll'} + \\ &= + \begin{cases} -\frac{16i\alpha mm'}{\phi(m^2 - m'^2)} \frac{1}{J'_m(\lambda_{ml}) J'_{m'}(\lambda_{m'l'})} \\ \times \int_0^1 dr r J_m(\lambda_{ml} r) J_{m'}(\lambda_{m'l'} r) & \text{for } (m + m')\phi/\pi \text{ odd integer;} \\ 0 & \text{elsewhere.} \end{cases} \end{aligned} \quad (4.21)$$

We have used only integer Bessel functions above, and this restricts ϕ to be $\pi/\text{integer}$.

Note that in the classical mechanics, the arc wall does not act any differently from the stationary case. Thus all the chaotic motion is due to the straight walls. We would like to study the behaviour of the off-diagonal terms in order to study convergence. Unfortunately, it was not possible to find asymptotic expressions for the integral of two Bessel functions above, so this could not be done.

(c). Rotating Ellipses [60]

Of particular interest is the elliptical billiard, rotating about its centre. In the liquid drop model of nuclear physics, one may regard the nucleus as a bag of liquid distorted into an oblate ellipsoid by rotation, and may to a first approximation be modelled using a single particle wavefunction [62]. This is simply the three-dimensional version of the rotating ellipse studied by Frisk and Arvieu. They study the classical mechanics of the system, and show that (similar to the rotating circle), it shows regular motion for very low and very high energies, and chaotic motion for intermediate energies. It would be interesting to study the quantum mechanics of this system.

4.2 Energy Levels of the Rotating Circular Billiard

It is more appropriate to use polar co-ordinates whose origin is the centre of the circular billiard. The Schrödinger equation becomes,

$$\mathcal{H}\psi = -\nabla^2\psi + 2i\alpha \left\{ \left(1 + \frac{\cos\theta}{r} \right) \frac{\partial}{\partial\theta} + \sin\theta \frac{\partial}{\partial r} \right\} \psi = \mathcal{E}\psi \quad (4.22)$$

Now using the orthonormal basis functions

$$\phi_{ml} = N_{ml} J_m(\lambda_{ml} r) e^{im\theta}, \quad (4.23)$$

where λ_{ml} are the zeros of the Bessel functions, and

$$N_{ml} = [\sqrt{\pi} J'_m(\lambda_{ml})]^{-1} \quad (4.24)$$

we obtain the matrix elements of \mathcal{H}

$$\begin{aligned} \mathcal{H}_{mlm'l'} &= \langle m'l' | \mathcal{H} | ml \rangle \\ &= \begin{cases} \lambda_{ml}^2 - 2\alpha m, & \text{for } l' = l, m' = m; \\ -2\pi\alpha\lambda_{ml}N_{ml}N_{m'l'} \int_0^1 dr r J_m(\lambda_{ml}r) J_m(\lambda_{m'l'}r), & \text{for } m' = m \pm 1; \\ 0, & \text{elsewhere.} \end{cases} \end{aligned} \quad (4.25)$$

The Bessel functions were computed to 14 figure accuracy using NAG routines for $J_0(x)$ and $J_1(x)$ and calculating $J_n(x)$ from these by upward recursion for large x ($x > n$), and downward recursion for small x . The zeros were found by bracketing the root using McMahon's formula and the asymptotic formula for large orders [54] then using Newton-Raphson and bisection methods, and were sorted in ascending order. The integrations were computed to 10 figures using an adaptive Gauss 30-point and Kronrod 61-point NAG routine. This is particularly good for oscillating integrands. Diagonalisation was performed using another NAG routine which reduces matrices to real symmetric tridiagonal form, and then uses the QL algorithm. [64] was a very useful source for many of these routines.

The eigenvalues are the diagonal elements of the diagonalised Hamiltonian matrix. When $\alpha = 0$ the matrix is already diagonal; the basis functions are also eigenfunctions. But the diagonal elements λ_{ml}^2 are not in ascending order. We expect the high-lying levels to be most affected as α increases, so the matrix was re-ordered so that the low-lying levels are the first to be calculated. This will increase the reliability of the computed eigenvalues. We thus sort the zeros λ_{ml} in ascending order, using the mapping obtained $[m, l] \mapsto i$ to re-order the Hamiltonian matrix,

$$\mathcal{H}_{ij} = \mathcal{H}_{m(i)l(i)n(j)k(j)}. \quad (4.26)$$

In order to diagonalise this matrix numerically we need to truncate it to a finite size. The difficulty is knowing when the truncated matrix is a good approximation for the infinite one, and how well the eigenvalues converge to their true values as the size of the matrix is increased. Unfortunately, because we cannot find asymptotic formulae for the Bessel integral, $\int_0^1 dr r J_m(\lambda_{ml}r) J_m(\lambda_{m'l'}r)$, we cannot use Gershgorin's theorem to set a theoretical bound. Resorting the matrix elements as above must help, because we expect that the eigenvalues for $\alpha \neq 0$ are similar to those at $\alpha = 0$, at least for small α . But as $\alpha \rightarrow \infty$ (the semiclassical limit $\hbar \rightarrow 0$) high-lying elements of the matrix are likely to affect the low-lying elements significantly. It is even hard to tell whether the limiting matrix is even diagonalisable. Presumably it is, because otherwise a semiclassical limit would not be possible. My own solution to this problem was to always diagonalise two size matrices (in this case 300×300 and 380×380) and to then compare their eigenvalues. If the relative error of eigenvalues is greater than 10%, that value is rejected. By this criterion it was possible to diagonalise matrices in the range $0 \leq \alpha \leq 15$. Seventy five matrices of each size were diagonalised within this range. Only the first sixty gave enough accurate eigenvalues to be used.

At the time of these calculations, I did not have a theoretical expression for the asymptotic number of modes. So the staircase function $\mathcal{N}(E)$ was fitted numerically. The semiclassical Weyl rule with corrections for a stationary billiard, reviewed in section (2.9), gives terms in $\sqrt{\mathcal{E}}$ and \mathcal{E} , and a constant. We assume

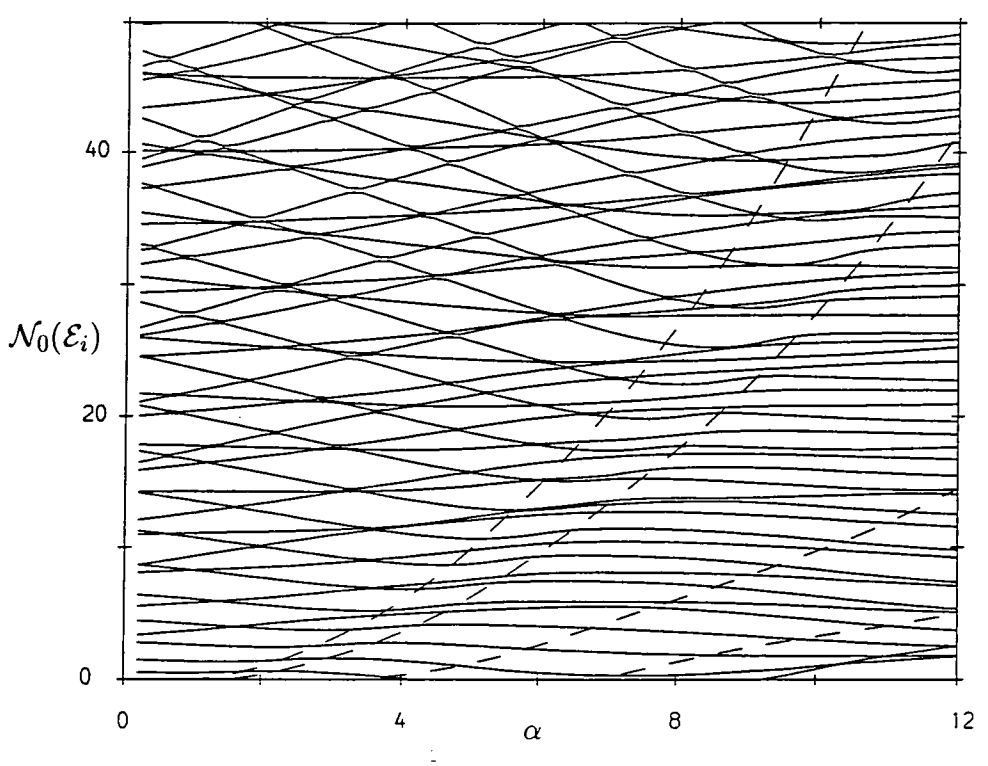


Figure 4.2.1. The unfolded energy level spectrum $\mathcal{N}_0(\mathcal{E}_i)$ for the rotating circle versus $\alpha = 1/\hbar$. The broken lines denote curves of constant classical energy at (from bottom to top) $E = -1, -\frac{2}{3}, 0, 0.5$.

that the rotation causes a deviation from this. We tried several fits, the best one occurred when adding a quadratic term, giving

$$\mathcal{N}_0(\mathcal{E}) = a + b\mathcal{E} + c\sqrt{\mathcal{E}} + d\mathcal{E}^2 \quad (4.27)$$

where a, b, c, d are constants. So

$$\langle \Delta\mathcal{E}(\mathcal{E}) \rangle = \left[\frac{d\mathcal{N}_0}{d\mathcal{E}}(\mathcal{E}) \right]^{-1}. \quad (4.28)$$

The ratio of the spacing to the local mean spacing is

$$S_i = \frac{\mathcal{E}_{i+1} - \mathcal{E}_i}{\langle \Delta\mathcal{E}(\mathcal{E}) \rangle} = \frac{d\mathcal{N}_0}{d\mathcal{E}}(\mathcal{E}_{i+1} - \mathcal{E}_i) \approx \mathcal{N}_0(\mathcal{E}_{i+1}) - \mathcal{N}_0(\mathcal{E}_i). \quad (4.29)$$

Thus we can use the ‘unfolded’ spectrum $e_i \equiv \mathcal{N}_0(\mathcal{E}_i)$, with $S_i = e_{i+1} - e_i$.

The lowest fifty eigenvalues $e_i(\alpha)$ of each matrix are plotted against the parameter α in figure (4.2.1) For small α and high energy there are a large number of apparent crossings, but the resolution of the graph is not good enough to distinguish whether these are real or not. Upon closer inspection some appear to be real, but they are more likely to be avoided crossings with exceedingly narrow separations of the order $\exp(-\text{constant}/\hbar)$. This is predicted by Berry [24] for integrable systems from consideration of tunnelling between neighbouring tori (which is disregarded in the semiclassical torus quantisation). Thus much of the spectrum for low α appears to be ‘regular’. However for large α and low energies the pattern of the spectrum changes. There are less level crossings, and those which do exist are actually avoided crossings. The energy levels are also much more evenly distributed. This is the transition of the regular spectrum where there is a large probability of near degeneracies ($P(S) \rightarrow \text{constant}$ as $S \rightarrow 0$) to a chaotic spectrum where there is level repulsion and hence little probability of degeneracies ($P(S) \rightarrow 0$ as $S \rightarrow 0$). Each near crossing shows strong mixing between states, and wavefunctions appear to exchange quantum numbers. This is manifested by the exchange of their slopes $dE_i/d\alpha$. Such mixing is required many times if we expect regular (in fact separable) energy levels at $\alpha = 0$ to be continuously deformed to the ‘random’ energy levels in the chaotic region. Also on figure (4.2.1) has been plotted curves of constant classical energy at $E = -1$, $E = 0.5$, between which the classical motion is mainly chaotic, and $E = -\frac{2}{3}$, $E = 0$ between which the motion is almost completely chaotic. The figure clearly shows that between these curves there is little level crossing, but outside them there is much level crossing.

4.3 Energy Level Spacing Statistics

The energy level spacing distribution is not a very useful property to plot directly. $P(S)$ can only be computed averaged over an interval, and in order to have enough eigenvalues in each interval (or bin) a large size bin is required which reduces the resolution of the graph. It is more natural to use the integral

distribution:

$$I(S) = \int_0^S P(x) dx = \lim_{M \rightarrow \infty} \frac{1}{M} \sum_{i=1}^M \Theta(S - S_i) \quad (4.30)$$

and then the spacing values are used fully. $I(S)$ is approximated by the empirical distribution function (EDF),

$$I_M(S) = \frac{1}{M} \sum_{i=1}^M \Theta(S - S_i) \quad (4.31)$$

We would like to investigate the spectrum around a particular energy E to see whether its statistics are related to the degree of chaos in the classical phase space. Thus $I_M(S)$ was computed for several ranges of the quantum label i of the energy level e_i . There are two properties we wish to maximise; we wish there to be a large number of eigenvalues in order to distinguish between different statistics, but opposing this we wish the energy range to be small enough in order that the classical phase space does not change significantly over the energy range. To be able to do this well we require \hbar to be small (α large). Ranges $i = 1$ to 50, $i = 50$ to 100, $i = 100$ to 150 were chosen. The classical energy ranges to which these correspond are shown in table (4.3.1). The combined ranges $i = 1$ to 100 and $i = 1$ to 150 were also used.

To each distribution the Kolmogorov-Smirnov and the W^2 EDF statistics tests were made [65], to determine the goodness of fit to either a Poisson or a GOE distribution. The W^2 test seemed to be the most powerful test in this case. The results for the W^2 test are shown in table (4.3.2). Let us consider the lowest 50 eigenvalues. For low α the test accepts both distributions, so we cannot say which distribution the data fits. For α in the range 3.2 to 3.8 and 5.8 to 6.6 the data fits only the Poisson, and for α in the range 4.0 to 5.4 and 6.8 to 12.0 the data fits only the GOE. Above $\alpha = 12.0$ the energy levels lose accuracy. The results show that the spectrum does behave as expected for large α . However there is not a smooth transition from Poisson to GOE statistics as we might have expected, but an intermittent one. At one point the spectrum becomes extremely regular, where we might have expected it to be quite chaotic.

Table 4.3.1. The first, fiftieth, one hundredth, and one hundred and fiftieth energy levels of the rotating circle, scaled to correspond to the classical energy E. It shows that the energy range condenses onto the most chaotic strata of hyperenergy surfaces in phase space.

α	\hbar	E_1	E_{50}	E_{100}	E_{150}
0.400	2.5000	17.8	1274.9	2547.9	3808.3
0.800	1.2500	4.2	314.6	625.2	938.6
1.200	0.8333	1.7	137.9	272.3	411.0
1.600	0.6250	0.7	76.3	150.4	229.5
2.000	0.5000	0.2	47.1	95.3	145.1
2.400	0.4167	-0.1	32.0	65.6	99.8
2.800	0.3571	-0.3	22.8	47.7	72.3
3.200	0.3125	-0.5	17.0	36.1	55.0
3.600	0.2778	-0.6	13.2	28.2	42.8
4.000	0.2500	-0.7	10.5	22.5	34.4
4.400	0.2273	-0.8	8.3	18.1	28.1
4.800	0.2083	-0.9	6.6	14.8	23.1
5.200	0.1923	-0.9	5.4	12.3	19.4
5.600	0.1786	-1.0	4.5	10.3	16.5
6.000	0.1667	-1.0	3.9	8.8	14.2
6.400	0.1563	-1.1	3.3	7.5	12.2
6.800	0.1471	-1.1	2.7	6.5	10.6
7.200	0.1389	-1.2	2.3	5.7	9.3
7.600	0.1316	-1.2	2.0	4.9	8.2
8.000	0.1250	-1.2	1.7	4.4	7.3
8.400	0.1190	-1.2	1.4	3.9	6.4
8.800	0.1136	-1.3	1.2	3.4	5.7
9.200	0.1087	-1.3	1.0	3.0	5.1
9.600	0.1042	-1.3	0.8	2.7	4.5
10.000	0.1000	-1.3	0.7	2.4	4.1
10.400	0.0962	-1.3	0.5	2.2	3.7
10.800	0.0926	-1.4	0.4	1.9	3.4
11.200	0.0893	-1.4	0.3	1.6	3.0
11.600	0.0862	-1.4	0.2	1.4	2.8
12.000	0.0833	-1.4	0.2	1.3	2.5

The next range of eigenvalues from $i = 50$ to 100 has an energy range which does not enter the chaotic region until α is about 8 or 9. There is some evidence for a transition in the spectrum near $\alpha = 8.8$, but above this eigenvalues are unreliable, and there is again evidence for GOE statistics for small α (near 3.8). The spectrum for $i = 100$ to 150 shows little evidence for GOE statistics in the range of $\alpha = 0.0$ to 5.0 which could be tested. This is expected, because none of the energies enter the chaotic region. For $i = 1$ to 100 and $i = 1$ to 150 the

Table 4.3.2. The W^2 statistic W_{n_1, n_2}^2 for the n_1^{th} eigenvalue to the n_2^{th} eigenvalue. Table (4.3.1) gives the corresponding energy ranges. The rejection of the fit is at a significance level of 5% (critical $W_{cr}^2 = 0.460$). The A or R after the statistic denotes acceptance or rejection respectively of the fit.

W^2 Statistic for Wigner Distribution				W^2 Statistic for Poisson Distribution		
α	$W_{1,50}^2$	$W_{50,100}^2$	$W_{100,150}^2$	$W_{1,50}^2$	$W_{50,100}^2$	$W_{100,150}^2$
0.4	0.300 A	0.604 R	0.507 R	0.257 A	0.124 A	0.101 A
0.8	0.257 A	0.441 A	0.546 R	0.294 A	0.162 A	0.074 A
1.2	0.228 A	0.578 R	0.576 R	0.400 A	0.081 A	0.084 A
1.6	0.267 A	0.770 R	0.785 R	0.416 A	0.063 A	0.066 A
2.0	0.320 A	0.624 R	0.390 A	0.235 A	0.045 A	0.144 A
2.4	0.166 A	0.552 R	0.272 A	0.328 A	0.140 A	0.232 A
2.8	0.300 A	0.392 A	0.703 R	0.293 A	0.176 A	0.135 A
3.2	0.523 R	0.284 A	1.068 R	0.100 A	0.338 A	0.040 A
3.6	0.478 R	0.279 A	0.941 R	0.161 A	0.299 A	0.043 A
4.0	0.219 A	0.333 A	1.003 R	0.508 R	0.179 A	0.035 A
4.4	0.237 A	0.479 R	0.972 R	0.482 R	0.112 A	0.087 A
4.8	0.185 A	0.912 R	1.277 R	0.822 R	0.043 A	0.048 A
5.2	0.131 A	1.854 R	0.742 R	0.695 R	0.174 A	0.051 A
5.6	0.302 A	1.413 R	0.638 R	0.229 A	0.056 A	0.056 A
6.0	0.852 R	1.086 R	0.780 R	0.113 A	0.039 A	0.041 A
6.4	0.809 R	0.857 R	1.317 R	0.115 A	0.073 A	0.051 A
6.8	0.179 A	0.656 R	1.086 R	0.500 R	0.058 A	0.062 A
7.2	0.270 A	0.701 R	0.903 R	0.630 R	0.062 A	0.353 A
7.6	0.113 A	0.812 R	1.025 R	1.236 R	0.026 A	0.066 A
8.0	0.071 A	0.646 R	1.254 R	0.659 R	0.065 A	0.136 A
8.4	0.055 A	0.533 R	2.038 R	0.894 R	0.150 A	0.281 A
8.8	0.071 A	0.317 A	1.850 R	0.826 R	0.247 A	0.310 A
9.2	0.112 A	0.695 R	1.846 R	0.685 R	0.058 A	0.345 A
9.6	0.074 A	0.739 R	3.115 R	0.968 R	0.114 A	0.671 R
10.0	0.097 A	0.958 R	3.906 R	1.182 R	0.102 A	0.940 R
10.4	0.080 A	1.353 R	3.904 R	1.026 R	0.078 A	0.927 R
10.8	0.128 A	0.764 R	1.867 R	1.232 R	0.028 A	0.362 A
11.2	0.129 A	0.503 R	1.027 R	1.509 R	0.202 A	0.147 A
11.6	0.159 A	0.178 A	0.782 R	1.836 R	0.609 R	0.196 A
12.0	0.196 A	0.138 A	1.455 R	2.281 R	0.436 A	0.161 A

larger number of eigenvalues will make the statistical tests more powerful, but the energy range is too large to expect uniform statistics except at very low α where we expect Poissonian statistics almost everywhere.

Typical members of these sets of distributions are shown in figure (4.3.1).

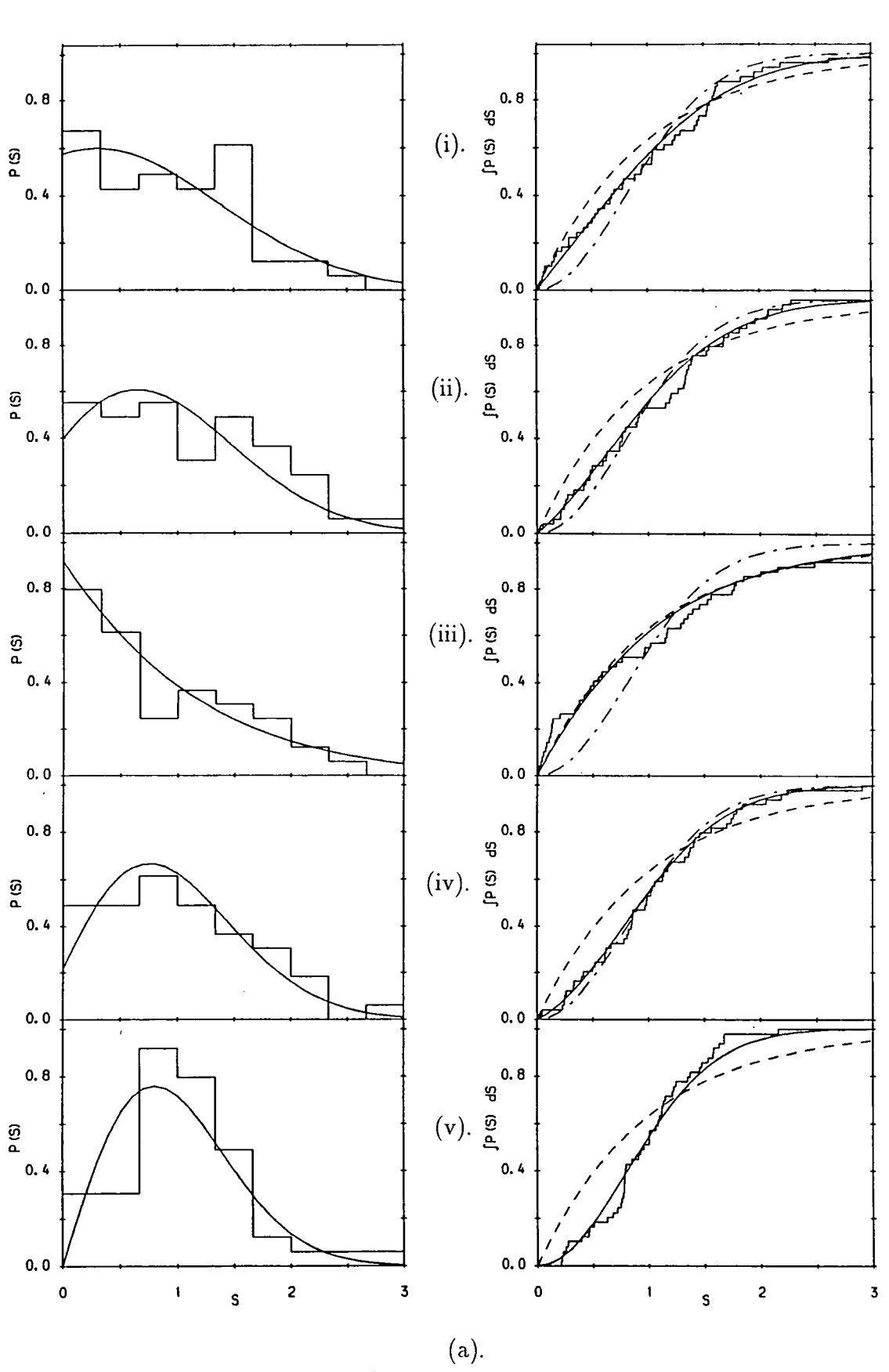


Figure 4.3.1. (caption overleaf)

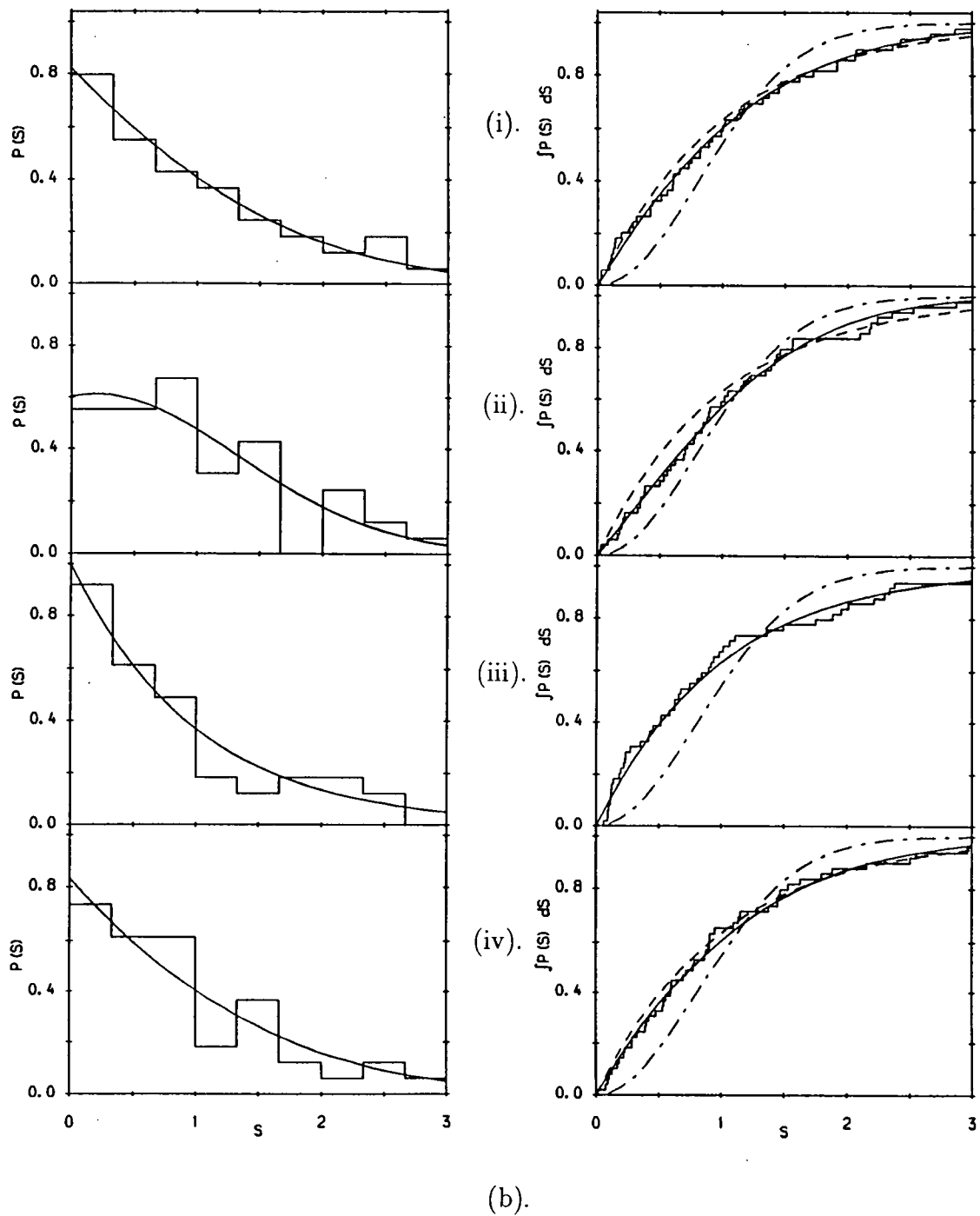


Figure 4.3.1. (caption overleaf)

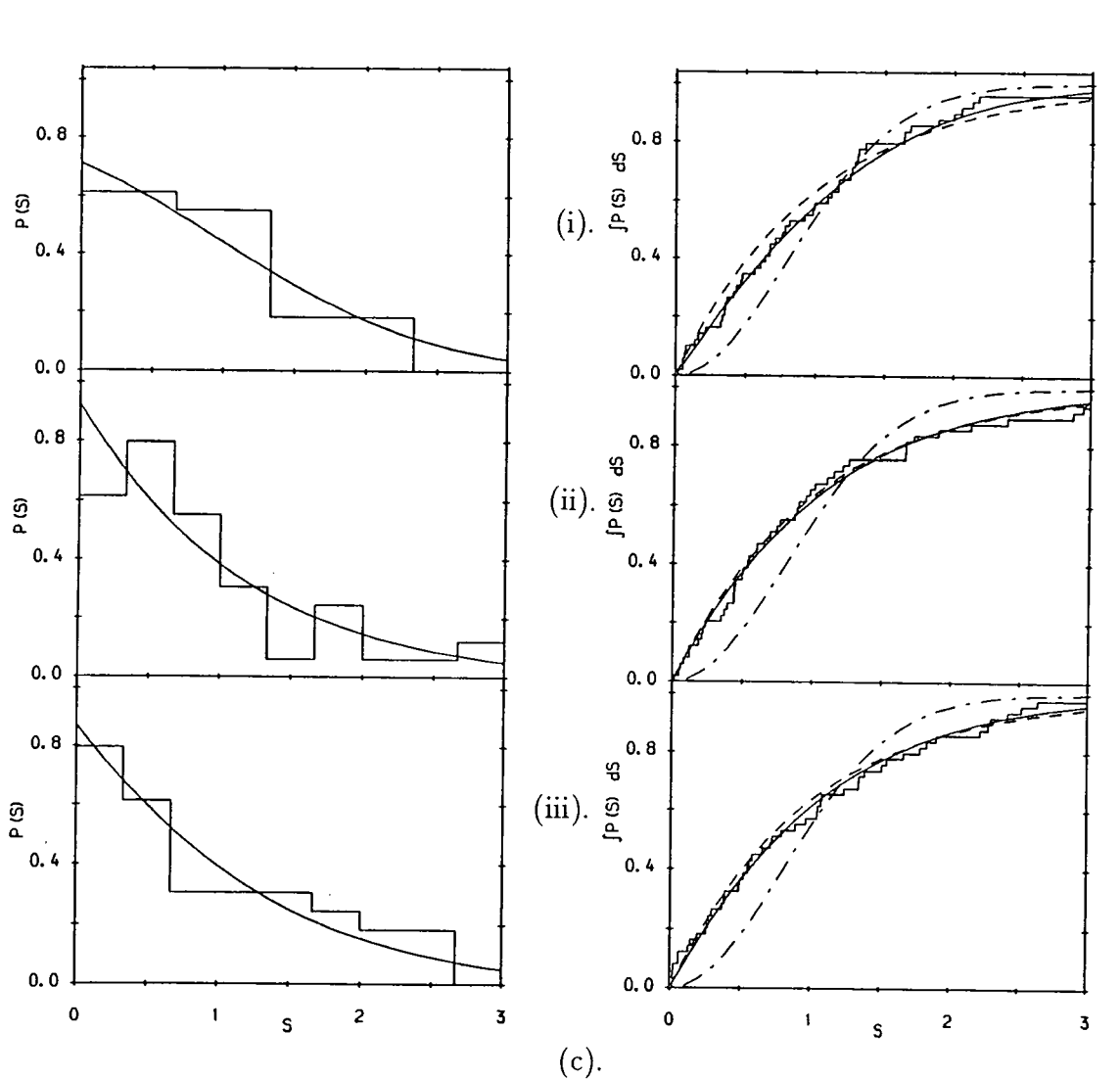


Figure 4.3.1. The level spacing distribution (left) and the integral (cumulative) distribution (right) for the rotating circle. The broken curve is the Poisson distribution, the chain curve is the Wigner distribution and the full curve is the distribution found by fitting the data by least squares to equation (4.33). The figures (i)-(v) correspond to $\alpha = 2, 4, 6, 8, 10$ respectively, and are drawn for (a) the first 50 levels (b) the next fifty levels (c) the levels \mathcal{E}_{100} to \mathcal{E}_{150} .

4.4 Spacing Distributions for Mixed Systems

We consider here a model, first described by Berry and Robnik [66] for systems that have both regular and chaotic regions in phase space. This is a simple model that assumes:

- (i). each disconnected regular region in phase space gives a level sequence whose statistics are Poissonian.
- (ii). each disconnected chaotic region in phase space gives a level sequence whose statistics are GOE, GUE (depending on the time-reversibility).
- (iii). the proportion of the total level sequence due to the i^{th} region is equal to the Liouville measure μ_i of that region (with $\sum_i \mu_i = 1$).
- (iv). the level sequences are superposed to give the total sequence of levels.

The reasoning behind (i) and (ii) is that regular regions will give regular levels, and chaotic regions give irregular levels. We can justify (iii) because each level ‘occupies’ a volume h^N in phase space, so we expect the number of levels due to a region of phase space to be proportional to the volume of that region (except for boundary corrections). Assumption (iv) means we assume that the two types of region do not classically communicate, and they can be treated as separate quantum mechanically. An argument against this is that they are not easily decomposed from each other, and the detail of their entanglement may be significant when it is no longer semiclassical. That is quantum tunnelling may be important. Item (iv) is the same as assuming that the Hamiltonian matrix is block diagonal, with no coupling terms between each block (which represents a disconnected region). Within a block there may be strong coupling, due to the ergodicity of chaotic motion, or no coupling, due to the non-mixing nature of regular motion.

From these assumptions Berry and Robnik show that the probability density

function is,

$$P(S) = \frac{d^2}{dS^2} \left[e^{-\mu_1 S} \prod_{i=2}^M \operatorname{erfc} \left(\frac{\sqrt{\pi}}{2} \mu_i S \right) \right], \quad (4.32)$$

where μ_1 is the sum of all the Liouville measures for the regular regions, and $\mu_i, i = 2, \dots, M$ is the Liouville measure for each chaotic region. So $P(0)$ is $1 - \sum_i^M \mu_i^2$. If there are many chaotic regions of equal weight, say $\bar{\mu} = (1 - \mu_1)/(M - 1)$ then $P(0) \rightarrow 1$ as $M \rightarrow \infty$, showing that there can be level clustering, even if there is strong chaotic motion. Even if there is only one large chaotic region, with say $\mu_2 = \frac{1}{2}$, $P(0)$ is $\frac{3}{4}$. Thus to expect detectable level repulsion, with few energy levels, we need to look at the most chaotic energies of our rotating circle.

Before doing so, we should mention that this simple model has been challenged by Bohigas, Tomsovic and Ullmo [67]. They realised that important contributions are present when the diffusion of a trajectory in a chaotic region is hindered by partial barriers of the motion due to cantori and their associated invariant stable and unstable manifolds. These partial barriers reduce the classical flux transfer between parts of the chaotic region. This introduces long time scales for the trajectory to visit both sides of the barrier. Quantum mechanically, this time scale may be longer than the break time beyond which quantum chaos is suppressed by the h^N graininess of phase space. Thus the partial barrier may be a true barrier quantum mechanically, so that the two chaotic regions should be regarded as disconnected.

From figure (4.2.1) it can be seen that for small α there are few levels that are in the chaotic energy range, and so it is not possible to display level statistics for such a small number of levels. As we have seen earlier, if we take the first fifty levels for low α ($4.0 \leq \alpha \leq 5.4$) we see what seems to be level repulsion. But from figure (4.2.1) it can be seen that this is due to the non-random hash pattern of the level, giving a statistically small number of crossings at some α 's. We would expect better results with many more levels.

We would like to choose energy levels from the most chaotic region; however, at low α there would not be enough levels. Hence we use the first fifty energy

levels. These are mostly in the integrable region for small α , and mostly in the chaotic region for large α . The Berry-Robnik model does not apply for small α , because:

- (i). it is not semiclassical in this region, since $\hbar = 1/\alpha$ is large.
- (ii). it is not for a particular energy surface—the energy range is too large—and so subsequences are not superposed randomly (there may be a Poisson sequence adjacent to a GOE sequence).

However, we will still use the model, because it shows the transition from Poisson to GOE, and we expect it to be a good model for large α . Also, for simplification we suppose that there is only one large chaotic region of chaotic volume μ , and that the rest of phase space is regular of measure ν , so $\mu + \nu = 1$. The Berry-Robnik formula then gives

$$I(S; \mu) = 1 - \mu \exp(-\nu S) \exp\left(-\frac{1}{4}\pi(\mu S)^2\right) - \nu x \operatorname{erfc}\left(\frac{1}{2}\sqrt{\pi}\mu S\right), \quad (4.33)$$

where $I(S; \mu)$ is the integral distribution.

For each distribution at each α and each of the three energy ranges, we find μ by numerically fitting $I(S; \mu)$ to the data. The resulting fitting parameter μ is plotted against α for the three energy ranges in figure (4.4.1). Clearly, there is a sharp change in statistics at $\alpha \approx 6$ for the lowest fifty levels, and similarly for $\alpha \approx 3.5$ which reflect the non-randomness of the levels described earlier (they correspond to the vertical bands of high clustering in figure (4.2.1)). There are similar changes for the higher level sequences. The lower eigenvalues fit an almost pure GOE distribution for $\alpha \geq 9.6$. This agrees well with the classical prediction from figure (4.2.1). Only the first sixty eigenvalues are accurate enough at $\alpha = 12$, so we cannot consider the levels higher than this. Above $\alpha = 11.4$ there is some tailing off of μ , which may be due to the small regular regions still remaining on the borders of the energy range, particularly $-2 \leq E \leq -1$, which is becoming large enough to affect some of the lowest levels.

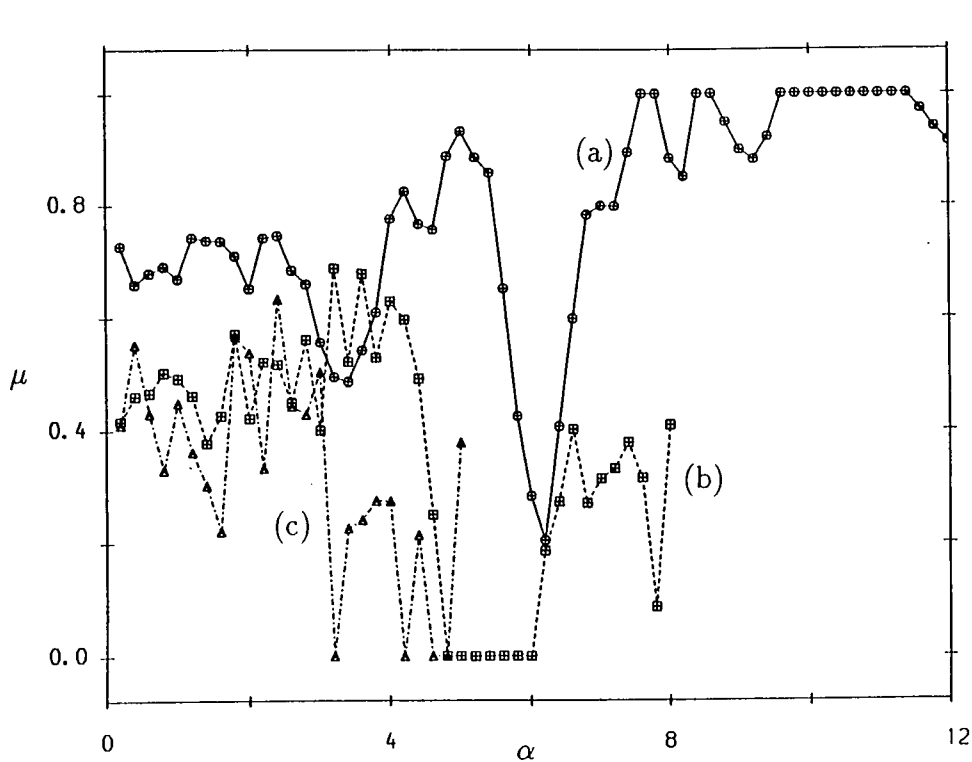


Figure 4.4.1. The fitting parameter μ of the cumulative mixed distribution (4.33) versus α .

4.5 The Asymptotic Level Density for Rotating Billiards

We derive, using Balian and Bloch's method reviewed in section (2.9), the asymptotic mean level density for rotating billiards. The following calculation generalises rotating billiards to billiards in the presence of a uniform magnetic field and a scalar potential. Firstly, we need the Green function for the unbounded case of a free particle in such fields:

$$(E - \hat{H}_0)G_0(q - q') = \delta(q - q'), \quad (4.34)$$

where

$$\hat{H}_0 = \frac{1}{2m} (-i\hbar\nabla - \mathbf{A}(q))^2 + V(q), \quad (4.35)$$

with \mathbf{A} , V defined by equations (4.9) and (4.10) (here we drop the bold notation

for convenience). The Fourier transform of $G_0(q)$ defined by

$$G_0(q) = \frac{1}{(2\pi)^2} \int_{\text{all } p} \tilde{G}_0(p) e^{ip \cdot q} d^2 p \quad (4.36)$$

is

$$\tilde{G}_0(p) = \frac{1}{E - V - \frac{1}{2m}(\hbar p - A)^2}. \quad (4.37)$$

Hence

$$\begin{aligned} G_0(q - q') &= \frac{1}{(2\pi)^2} \int \frac{e^{ip \cdot (q-q')} d^2 p}{E - V - \frac{1}{2M}(\hbar p - A)^2} \\ &= e^{iA \cdot (q-q')/\hbar} \cdot \frac{-im}{2\hbar^2} H_0^{(1)} \left(\frac{\sqrt{2m(E-V)}}{\hbar} \cdot |q - q'| \right) \end{aligned} \quad (4.38)$$

after shifting p by $A(q)/\hbar$. Balian and Bloch show that

$$\rho_0(E) \sim -\frac{\text{Im}}{\pi} \left\{ \left[\int_{\mathcal{B}} d^2 q G_0(q - q') \right]_{q \rightarrow q'} - \frac{\hbar^2}{2m} \int_{\partial \mathcal{B}} d\alpha \left[\frac{\partial}{\partial n_\alpha} F(\alpha, \beta) \right]_{\alpha=\beta} \right\}, \quad (4.39)$$

where n_α is the normal at a point α on the boundary $\partial \mathcal{B}$ of the classically accessible billiard \mathcal{B} , and

$$F(\alpha, \beta) = \int d^2 q G_0(\alpha - q) G_0(q - \beta). \quad (4.40)$$

Greek letters are used to denote points on the boundary. Balian and Bloch also include a convergence factor, which we have left out of the formula for clarity, but it should be taken into account.

To calculate $\partial F / \partial n_\alpha$, we use a one-dimensional Fourier transform on the boundary defined by

$$G_0(q - q') = \int \frac{dv}{2\pi} \hat{G}_0(vz) e^{iv(\gamma-\gamma')}, \quad (4.41)$$

where $z, \gamma - \gamma'$ are the local normal and tangential co-ordinates respectively, such that $q = (z, \gamma)$, $q' = (z, \gamma')$ with $z = 0$ on the boundary. From the

previous Fourier transform (equation (4.37)) written in the variable $w = (u, v) = p - (A/\hbar)$, we find

$$\tilde{G}_0(w) = \frac{e^{iA \cdot (q-q')/\hbar}}{E - V - \frac{\hbar^2}{2m}w^2}. \quad (4.42)$$

Thus

$$\hat{G}_0(v, z) = \int_{-\infty}^{\infty} \frac{du}{2\pi} \tilde{G}_0(w) e^{iuz}. \quad (4.43)$$

Hence

$$\begin{aligned} \hat{G}_0(v) \equiv G_0(v, 0) &= -\frac{2m}{\hbar^2} \int_{-\infty}^{\infty} \frac{du}{2\pi} \frac{e^{iA_\gamma(\gamma-\gamma')/\hbar}}{(u^2 + a^2)} \\ &= -\frac{2m}{\hbar^2} \frac{e^{iA_\gamma(\gamma-\gamma')/\hbar}}{2a(v)}, \end{aligned} \quad (4.44)$$

where $a^2 \equiv v^2 - \frac{2m}{\hbar^2}(E - V)$, and A_γ is the component of A parallel to $\gamma - \gamma'$.

It can be shown that

$$\frac{\partial F}{\partial n_\alpha} = -\frac{\partial F}{\partial z} = -\frac{1}{2} \int d\gamma G_0(\alpha - \gamma) G_0(\gamma - \beta). \quad (4.45)$$

So that

$$\begin{aligned} \frac{\partial F}{\partial n_\alpha} &= -\frac{1}{2} \int d\gamma \int \frac{dv dv'}{(2\pi)^2} \hat{G}_0(v) \hat{G}_0(v') e^{i(v-v')\gamma} e^{v\alpha - v'\beta} \\ &= -\frac{1}{2} \left(\frac{2m}{\hbar^2} \right)^2 \int \frac{dv}{2\pi} \frac{1}{4[a(v)]^2} \exp \left\{ i \left(v + \frac{A_\gamma}{\hbar} \right) (\alpha - \beta) \right\}. \end{aligned} \quad (4.46)$$

This gives

$$\left\{ \frac{\partial F}{\partial n_\alpha} \right\}_{\alpha=\beta} = -\frac{im^2}{4\hbar^4 k(\alpha)}, \quad (4.47)$$

where $k(\alpha)$ is defined by

$$k(\alpha) \equiv \frac{\sqrt{2m(E - V(\alpha))}}{\hbar}. \quad (4.48)$$

The first term of $\rho_0(E)$ is easily shown, from the pole in the Hankel function, to

be

$$\frac{m}{2\pi\hbar^2} \int_{\mathcal{B}} d^2q \Theta(E - V). \quad (4.49)$$

The second term of $\rho_0(E)$ is

$$\frac{\text{Im}}{\pi} \frac{\hbar^2}{2m} 2 \int d\alpha \frac{-im^2}{4\hbar^4 k(\alpha)} = -\frac{m}{4\pi\hbar^2} \int_{\partial\mathcal{B}} \frac{d\alpha}{k(\alpha)}. \quad (4.50)$$

So the result is

$$\rho_0(E) \sim \frac{m}{2\pi\hbar^2} \int_{\mathcal{B}} d^2q \Theta(E - V) - \frac{m}{4\pi\hbar^2} \int_{\partial\mathcal{B}} \frac{d\alpha}{k(\alpha)}. \quad (4.51)$$

Integrating this give the number of modes

$$\mathcal{N}_0(E) \sim \int_{\mathcal{B}} d^2q \frac{k^2(q)}{4\pi} - \int_{\partial\mathcal{B}} d\alpha \frac{k(\alpha)}{4\pi} + \text{const.} \quad (4.52)$$

When k is a constant this reduces to the result for stationary billiards, $\mathcal{N}_0(E) \sim \frac{\mathcal{A}k^2}{4\pi} - \frac{\mathcal{L}k}{4\pi}$, where \mathcal{A} , \mathcal{L} are the area and perimeter of the billiard.

We shall now calculate $\mathcal{N}_0(E)$ for the rotating circle. Here we consider the Hamiltonian with $m = 1$, $\omega = 1$ giving $k^2 = E + \frac{1}{2}q^2$. The first integral is over the classically allowed region, *i.e.* for $\frac{1}{2}q^2 > -E$. For $-2 < E < 0$, this is a region between two circles, as shown in figure (4.5.1). The second integral is over the boundary of the billiard, which is touching the shaded region.

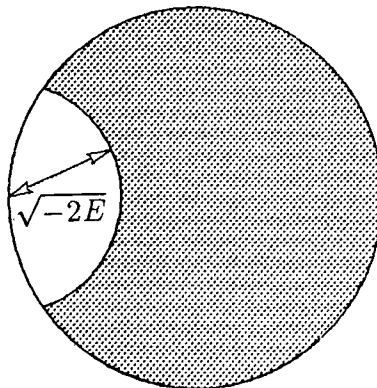


Figure 4.5.1. The classically allowed region of the rotating circular billiard.

The integrals are easily evaluated using polar co-ordinates at the point of rotation, giving

$$\mathcal{N}_0(E) = \begin{cases} \frac{1}{4\pi\hbar^2}(2\pi E + \frac{3}{2}\pi) - \frac{\sqrt{2E+4}}{\pi\hbar} E_{\text{el}}(m_{\text{el}}) & \text{for } E \geq 0; \\ \frac{1}{4\pi\hbar^2} [\beta(2 + \cos 4\beta) - \frac{3}{4} \sin 4\beta] - \frac{\sqrt{2E+4}}{\pi\hbar} \\ \times \left[m_{\text{el}}^{\frac{1}{2}} E_{\text{el}}(m_{\text{el}}^{-1}) - \left(m_{\text{el}}^{\frac{1}{2}} - m_{\text{el}}^{-\frac{1}{2}} \right) K_{\text{el}}(m_{\text{el}}^{-1}) \right] & \text{for } E \leq 0, \end{cases} \quad (4.53)$$

where $K_{\text{el}}(m_{\text{el}})$, $E_{\text{el}}(m_{\text{el}})$ are the first and second complete elliptic integral [54] and

$$\begin{aligned} \beta &= \cos^{-1} \left(\sqrt{-E/2} \right), \\ m_{\text{el}} &= 1/(1+E/2). \end{aligned} \quad (4.54)$$

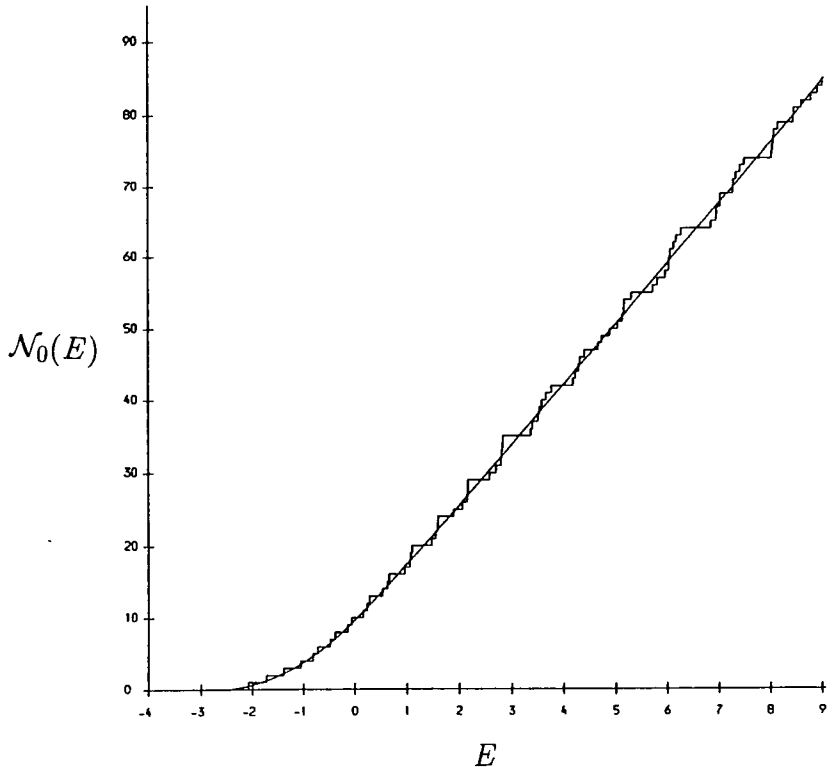


Figure 4.5.2 The spectral staircase $\mathcal{N}_0(E)$ for the rotating circular billiard at $\alpha = 6$. The curve shows the theoretical asymptotic mean number of modes.

The result for $\mathcal{N}_0(E)$ cannot be compared directly with the numerically determined spectrum. The reason for this is that not all the levels were calculated but only those with positive angular momentum m . These levels are slightly inaccurate due to a coupling between the $m = 0$ states and the $m = \pm 1$ states, but this is unlikely to be significant. The positive and negative m states do not contribute equally to $\mathcal{N}_0(E)$ due to the asymmetry introduced by rotation, hence we cannot simply halve $\mathcal{N}_0(E)$ to compare with the positive m results. Instead I diagonalised a 380 by 380 matrix with elements of positive and negative m at some values of α , and compared the eigenvalues of this with $\mathcal{N}_0(E)$. The result for $\alpha = 6$ is shown in figure (4.5.2). This shows excellent agreement with the theoretical curve, and gives credibility to the accuracy and completeness of the spectrum, at least above the scale of the mean level spacing.

5. Discussion

The classical rotating circular billiard is seen to have the usual structures of KAM tori, mixed with chaotic motion. It is seen to approach integrability when the energy E is very high or very low, and to be almost completely ergodic and mixing for some intermediate energies.

A study of the periodic cycles has revealed the usual bifurcations, and period multiplying as the system becomes more chaotic. We have found the main fixed point and its bifurcation into a two-cycle. We have seen that these periodic orbits are unstable in the most chaotic energy range, and that the bifurcation also lies in this range, and happens when the trajectory from the fixed point glances the boundary.

This association between the glancing trajectory and chaotic motion has been seen to be due to a more general rôle of glancing trajectories: they cause discontinuities in the Poincaré map, and lead to stronger chaos than would be associated with the usual folding and stretching of the Hamiltonian flow. The range of energies for which glancing trajectories occur has been found theoretically, and is shown to correspond to the range for which the system is most chaotic.

Approximate invariant curves have been found, which agree well for anti-clockwise motion, but not so well for clockwise motion. The clockwise type fail particularly badly for those energies where there are glancing trajectories, which occur only for clockwise motion. We note that a special type of periodic orbit—the set of sliding trajectories, with infinite bounces in a finite time—has an important influence on the behaviour of much of the motion. These sliding trajectories become chaotic when there are glancing trajectories, again accounting for the ergodicity of the system at these energies.

A more detailed analysis of the system, calculating Lyapunov exponents and chaotic volume has shown exactly when the system becomes most chaotic and when it becomes most integrable.

Studying the rotating circular billiard quantum mechanically, we have seen that where the classical mechanics is completely integrable, the spectrum of

energy levels shows considerable clustering and level crossing, and that where the classical mechanics is completely chaotic, the spectrum shows much rigidity and level repulsion. We have seen that these results appear to be good, in spite of the lack of a good test for the accuracy of the eigenvalues at the fluctuation scale, although they agree well with the theoretical asymptotic mean level density. We have seen that as \hbar is reduced, the size of matrix required to obtain the same number of accurate eigenvalues is increased dramatically. This may be related to questions of quantum algorithmic complexity to be discussed later. We find good agreement between the range of energies for chaotic motion implied by the study of energy levels, and the range implied by the study of the classical motion. Studying the levels statistically has shown the usual Poisson and Wigner results, but this more detailed analysis has not revealed more than has been learnt from simply seeing the levels graphically against \hbar . There are two reasons. Firstly, the statistics use only one value of \hbar at a time, whereas the eye distinguishes the pattern over a range of \hbar . Secondly, there are really too few levels for good statistics.

In conclusion, the classical rotating circular billiard exemplifies a typical non-integrable conservative bound system, and the energy spectrum of the quantum rotating circular billiard show level crossing or level repulsion, corresponding well to the system being respectively classically integrable or classically chaotic. This is an example of quantum chaology [68] which though interesting does not tell us that the quantum system is chaotic. To do this requires the study of the time behaviour of quantum wavepackets, which we have not considered in this thesis.

We have by no means exhausted the work that can be done on rotating billiards. It would be interesting, using symbol sequences and an appropriate partition, to code the periodic orbits and hence aid their complete enumeration. Then Gutzwiller's trace formula could be studied in greater detail, testing the lower energy levels found from this against those found by the Rayleigh-Ritz method. We have not studied wavefunctions. This is because eigenfunctions of the rotating circle, written in terms of the Bessel basis functions, are computer intensive to plot. Heller [69] has given a method that will find very high

frequency eigenfunctions directly, using a boundary method, without having to find all the lower ones. It is much more efficient, because it uses sine and cosine basis functions. It can also be used to find eigenvalues. We mentioned earlier a better method for finding eigenvalues using the \hbar operator. This is a useful method because one finds all the levels along a line of constant classical energy in the $E\hbar$ -plane (*e.g.* along one of the dashed lines in figure (3.2.1)), and so the levels correspond to one particular Poincaré map rather than a whole range of maps. Suppose the \hbar operator finds the eigenvalues of $1/\hbar^2$, then rearranging Schrödinger's equation for a stationary billiard gives

$$-\nabla^2 \psi_i = \frac{2mE}{\hbar_i^2} \psi_i \quad (5.1)$$

where we have made \hbar the eigenvalue instead of E . So the \hbar operator is defined by:

$$\widehat{\left(\frac{1}{\hbar^2}\right)} \equiv -\frac{\nabla^2}{2mE}, \quad (5.2)$$

giving the eigenvalue equation

$$\widehat{\left(\frac{1}{\hbar^2}\right)} \psi_i = \left(\frac{1}{\hbar_i^2}\right) \psi_i. \quad (5.3)$$

The operator is simple because stationary billiards are scaling systems. But rotating billiards are not scaling, and it is not so easy to find the correct \hbar operator. Rearranging Schrödinger's equation for rotating billiards gives

$$(-i\hbar\nabla - \mathbf{A})^2 = 2m(E - V). \quad (5.4)$$

Here it is not so clear what the operator should be, because the \hbar cannot be isolated from the \mathbf{A} without introducing some direction to $-i\hbar\nabla - \mathbf{A}$ which cannot be determined. It would, however, be worth pursuing this.

It is conceivable that, because we have changed the line in the $E\hbar$ -plane along which to find eigenvalues, for some energies the line may pass between a gap where two levels repel. The eigenvalues of $1/\hbar^2$ would then be complex rather than real, which is plausible because the operator is not Hermitian.

I discussed this with Michael Berry, and upon his suggestion used Feynman's theorem [70] :

$$\frac{\partial E_k}{\partial \alpha} = \langle \psi_k | \frac{\partial \hat{H}}{\partial \alpha} | \psi_k \rangle, \quad (5.5)$$

where E_k , ψ_k are the respective eigenvalues and eigenfunctions of $\hat{H}(\alpha)$, and $\alpha = 1/\hbar$. For stationary billiards, the eigenvalues of $1/\hbar^2$ are never complex, because

$$\frac{\partial E_k}{\partial \alpha} = -\frac{2}{\alpha} (E_k - \langle V \rangle) \quad (5.6)$$

is always negative, and we require $\partial E_k / \partial \alpha$ to be zero for the situation to occur. For rotating billiards I was unable to reach a conclusion, because

$$\frac{\partial E_k}{\partial \alpha} = -\frac{2E_k}{\alpha} + \frac{\omega}{\alpha^2} \langle \psi_k | i\partial_\theta | \psi_k \rangle, \quad (5.7)$$

and I could not find out enough information about $\langle \psi_k | i\partial_\theta | \psi_k \rangle$ to tell whether this ever cancels $2E_k/\alpha\omega$.

It would be interesting to study other rotating systems in more detail. Classically, rotating ellipses [60] and the rotating square [71] have been considered. Perhaps these could now be studied quantum mechanically.

Many questions remain unanswered. We know that quantum mechanics suppresses chaos, but we have not been able to resolve whether the full classical regime is revealed in the limit $\hbar \rightarrow 0$. We have not addressed interpretational questions of quantum mechanics, or discussed methods which regard the motion as a mixture between classical, semiclassical and fully quantum mechanical regions, depending on the detail of the phase space structure in that region.

There are possible avenues of research that may bring answers to these. Joseph Ford [72] believes that quantum mechanics is never algorithmically complex, and hence it can never relate to classical chaos, which is. He has shown that for two simple systems, one classically chaotic and the other not, both have zero complexity in their time evolution. He has shown that the energy spectrums also have zero complexity. What is not clear is whether the complexity magically materialises when \hbar actually vanishes. This is a non-analytic limit (analogous to

limits between geometric and wave optics, or between perfect fluids and viscous fluids), and such a result would not be surprising if it were true. If it is false, then the correspondence principle fails.

A recent example, that I find particularly interesting by Shudo [73] is the algorithmic complexity of the eigenvalue sequence of the following tridiagonal matrix:

$$H_{ii} = \frac{1}{3}(\alpha m^2 + n^2) \quad (5.8)$$

$$H_{i+1,i} = H_{i,i+1} = \begin{cases} C_1 & i \text{ even}, \\ C_2 & i \text{ odd}, \end{cases} \quad (5.9)$$

where C_1, C_2 are constants less than one. This is not a real system, but has the eigenvalues of a rectangle for $C_1 = 0, C_2 = 0$. The matrix shows a Wigner-type distribution for the level spacing, for $C_1 = 0.4, C_2 = 0.9$. Using Gershgorin's theorem and the Strum theorem, Shudo shows that the sequence of levels has zero complexity.

This may appear to show that quantum mechanics is not algorithmically complex, but to analysis quantum mechanics fully, one needs to consider a wavefunction, not just eigenfunctions, and the wavefunction is a superposition of many eigenstates. For this one needs to consider the time dependence of Schrödinger's equation. Peres and Schulman [74] do exactly this. They ask the question, if one has a wavepacket and wishes to simulate the classical motion accurately how large does the Hilbert space (that is the size of the truncated basis functions) need to be? They show that this size must increase exponentially with the planned duration of the simulation, showing that although the eigenvalue sequence may have zero complexity, the total Hilbert space required for the correspondence principle does have complexity.

The study of time dependence in quantum mechanics is important for other reasons. Increase in the disorder of systems, and thus the second law of thermodynamics, is thought to be caused by chaotic motion and is said to give the arrow of time. If there is no chaos in quantum mechanics, then how do we explain this arrow or indeed the second law? There is also the grave difficulty in unravelling the double limit $\hbar \rightarrow 0, t \rightarrow \infty$ required for quantum chaos. We have seen that

taking the $t \rightarrow \infty$ limit first, and then the $\hbar \rightarrow 0$ limit gives zero complexity. But reversing the order of the limits will give a different answer—they do not commute [75]. This is due to the non-analyticity of the double limit. Answers to these questions are not easy; recently Berry has increased the effectiveness of asymptotic expansions to release information from the divergent tails of the series, by a method known as resurgence invented by Écalle [76]. Perhaps this will lead to a complete understanding of quantum chaos.

APPENDIX A

Here we evaluate the tangent map $J_F(\theta, \psi)$ as defined in section (3.3). For simplicity, we write

$$(\Theta, \Psi) = \mathbf{F}(\theta, \psi). \quad (\text{A1})$$

Then

$$J_F = \begin{pmatrix} \frac{\partial \Theta}{\partial \theta} & \frac{\partial \Theta}{\partial \psi} \\ \frac{\partial \Psi}{\partial \theta} & \frac{\partial \Psi}{\partial \psi} \end{pmatrix}. \quad (\text{A2})$$

From the equation of motion (3.12), we have for the time T between (θ, ψ) and (Θ, Ψ) ,

$$z(T) = 1 + e^{i\Theta} = (a + bT)e^{-iT}, \quad (\text{A3})$$

$$\dot{z}(T) = iv(T)e^{i(\Theta-\Psi)} = be^{-iT} - iz(T), \quad (\text{A4})$$

where

$$a = 1 + e^{i\theta} \quad (\text{A5})$$

$$b = ia + iv e^{i(\theta+\psi)} = i[1 + e^{i\theta} + ve^{i(\theta+\psi)}]. \quad (\text{A6})$$

So

$$z(T) = 1 + e^{i\Theta} = \left[(1 + e^{i\theta})(1 + iT) + ivTe^{i(\theta+\psi)} \right] e^{-iT} \quad (\text{A7})$$

$$\dot{z}(T) = iv(T)e^{i(\Theta-\Psi)} = i \left[(1 + e^{i\theta} + ve^{i(\theta+\psi)})e^{-iT} - z \right]. \quad (\text{A8})$$

From equation (A7) we find that

$$\tan \Theta = \frac{\operatorname{Im} z(T)}{\operatorname{Re}[z(T) - 1]} \equiv \frac{V(\theta, \psi, T)}{U(\theta, \psi, T)}. \quad (\text{A9})$$

This gives

$$\frac{\partial \Theta}{\partial \theta} = (UV_\theta - VU_\theta) + T_\theta(UV_T - VU_T) \quad (\text{A10})$$

$$\frac{\partial \Theta}{\partial \psi} = (UV_\psi - VU_\psi) + T_\psi(UV_T - VU_T). \quad (\text{A11})$$

Also

$$\tan\left(\frac{\pi}{2} + \Theta - \Psi\right) = \frac{\text{Im } \dot{z}}{\text{Re } \dot{z}} \equiv \frac{H(\theta, \psi, T)}{G(\theta, \psi, T)}. \quad (\text{A12})$$

This gives

$$\frac{\partial \Theta}{\partial \theta} - \frac{\partial \Psi}{\partial \theta} = \frac{1}{[v(T)]^2} \{(GH_\theta - HG_\theta) + T_\theta(GH_T - HG_T)\}. \quad (\text{A13})$$

$$\frac{\partial \Theta}{\partial \psi} - \frac{\partial \Psi}{\partial \psi} = \frac{1}{[v(T)]^2} \{(GH_\psi - HG_\psi) + T_\psi(GH_T - HG_T)\} \quad (\text{A14})$$

Using equations (A10) and (A11) we can find $\partial\Psi/\partial\theta$, $\partial\Theta/\partial\theta$. Thus using equations (A7) and (A8) we can find U , V , G , and H in terms of θ , ψ , and T . It only remains to note that

$$T_\theta = -\frac{UU_\theta + VV_\theta}{UU_T + VV_T}, \quad (\text{A15})$$

$$T_\psi = -\frac{UU_\psi + VV_\psi}{UU_T + VV_T}, \quad (\text{A16})$$

to see that we can find J_F in terms of θ , ψ , and T . Thus we only need to calculate T numerically in order to calculate J_F .

REFERENCES

- [1] D.B. Fairlie and D.K. Siegwart, *J. Phys. A* **21**, 1157-65 (1988).
- [2] D.K. Siegwart, *J. Phys. A* **22**, 3537-3550 (1989).
- [3] E.J. Squires and D.K. Siegwart, *Phys. Lett. A* **126**, 73-74 (1987).
- [4] H.W. Braden and D.K. Siegwart, *SU(n) Anomaly Generating Functionals: a Toolkit for Model Builders*, accepted for publication in *J. Phys. A* (1988).
- [5] G. Casati, B.V. Chirikov, J. Ford, F.M. Izraelev, in *Stochastic Behaviour in Classical and Quantum Hamiltonian Systems*, eds., G. Casati, J. Ford, *Springer Lecture Notes in Physics*, **93**, 334-352 (1979).
- [6] G.D. Birkhoff, *Acta Math.* **50**, 359-379 (1927).
- [7] H. Poincaré, *Les Methodes Nouvelles de la Mechanique Celeste*, Gauthier-Villars, Paris (1892).
- [8] J.K. Moser, *Mem. Am. Math. Soc.* **81**, 1-60 (1968).
- [9] V.I. Arnol'd, *Russ. Math. Surv.* **18:6**, 85-191 (1963).
- [10] Y.G. Sinai, *Func. Anal. and Appl.* **2**, 61-82 (1968).
- [11] V.I. Arnol'd and A. Avez, *Ergodic Properties of Classical Mechanics*, W. Benjamin (1968).
- [12] J.B. Pesin, *Soviet Math.-Doklady* **17**, 196-199 (1976).
- [13] C.E. Shannon and W. Weaver, *The Mathematical Theory of Information*, University of Ill. Press, Urbana (1949).
- [14] A.N. Kolmogorov, *IEEE Trans. Inf. Theory* **14**, 682 (1966).
- [15] Y.G. Sinai, *Russ. Math. Surv.* **25.2**, 137-189 (1970).
- [16] L.A. Bunimovich, *Commun. Math. Phys.* **65**, 295-312 (1979).
- [17] M. Wojtkowski, *Commun. Math. Phys.* **105**, 391-414 (1986).
- [18] N.L. Balazs and A. Voros, *Phys. Rep.* **143**, 109-240 (1986).
- [19] M.C. Gutzwiller, *J. Maths. Phys.* **8**, 1979-2000 (1967).

- [20] M.C. Gutzwiller, *J. Maths. Phys.* **12**, 343-358 (1971).
- [21] I.C. Percival, *Adv. Chem. Phys.* **36**, 1-61 (1977).
- [22] S.W. McDonald and A.N. Kaufman, *Phys. Rev. Lett.* **42**, 1189 (1979).
- [23] E. Heller, in *Quantum Chaos and Statistical Nuclear Physics*, eds. T.H. Seligman and H. Nishioka (Proceedings, Cuernavaca Mexico 1986), *Lecture Notes in Physics* **263**, Springer, Berlin (1986).
- [24] M.V. Berry, in *Chaotic Behaviour of Deterministic Systems, Les Houches Summer School Lectures XXXVI*, ed. R.H.G. Helleman and G. Joos, Amsterdam: North-Holland (1983).
- [25] O. Bohigas and M.J. Giannoni 1984, in *Mathematical and Computational Methods in Nuclear Physics*, ed. J.S. Dehesa, J.M.G. Gomez and A. Polls, *Lecture Notes in Physics* **209**, New York: Springer, 1-99 (1984).
- [26] C.E. Porter (ed.), *Statistical Theories of Spectra: Fluctuations*, New York: Academic (1965).
- [27] M. Robnik, *J. Phys. A* **17**, 1049-74 (1984).
- [28] M. Robnik and M.V. Berry, *J. Phys. A* **18**, 1361-78 (1985).
- [29] M.V. Berry and M. Robnik, *J. Phys. A* **19**, 649-668 (1986).
M. Robnik and M.V. Berry *J. Phys. A* **19**, 669-682 (1986).
- [30] M.V. Berry and R.J. Mondragon, *Proc. Roy. Soc. Lond.* **A400**, 53-74 (1987).
- [31] T.H. Seligman, J.J.M. Verbaarschot and M.R. Zirnbauer, *J. Phys. A* **18**, 2751-2770 (1985).
- [32] T. Matsushita and T. Terasaka, *Chem. Phys. Lett.* **105**, 511 (1984).
- [33] A.C. Scott: personal communication. (1988).
- [34] H. Goldstein, *Classical Mechanics*, Addison-Wesley (1950).
- [35] L.D. Landau and E.M. Lifshitz, *Mechanics (Third Edition)*, Pergamon (1976).

- [36] M.V. Berry, in *Topics in Nonlinear Dynamics*, ed. S. Jorna, Am. Inst. Phys. Conf. Proc. **46**, 16-120 (1978).
- [37] M.V. Berry, Eur. J. Phys. **2**, 91-102 (1981).
- [38] I.C. Percival, in *Nonlinear Dynamics and the Beam-Beam Interaction*, eds. M. Morith and J.C. Herrera, Am. Inst. Phys. Conf. Proc. **57**, 302 (1979).
- [39] S. Aubry, in *Solitons and Condensed Matter Physics*, eds. A.R Bishop and T. Schneider, Springer-Berlin, 264 (1978).
- [40] M.V. Berry and K.E. Mount, Reps. Prog. Phys. **35**, 315-397 (1972).
- [41] I.C. Percival, in *Quantum Mechanics and Chaos, Les Houches Summer School Lectures LII*, to be published by North-Holland (1990).
- [42] C. Morette, Phys. Rev. **81**, 848 (1951).
- [43] G. Papadopoulos, Phys. Rev. **D11**, 2870 (1975).
- [44] M.C. Gutzwiller, in *Quantum Mechanics and Chaos, Les Houches Summer School Lectures LII*, to be published by North-Holland (1990).
- [45] M. Sieber and F. Steiner, *Generalised Periodic Orbit Sum Rules for Strongly Chaotic Systems*, DESY preprint no. 89-003, (January 1989).
- [46] A. Einstein, Verh. Dtsch. Phys. Ges. **19**, 82-92 (1917).
- [47] M.V. Berry and M. Tabor, Proc. R. Soc. Lond. **A356**, 375-394 (1977).
- [48] M.V. Berry and M. Tabor, Proc. R. Soc. Lond. **A349**, 101-123 (1976).
- [49] M.V. Berry and M. Tabor, J. Phys. A **10**, 371-379 (1977).
- [50] R. Balian and C. Bloch, Ann. Phys. (N.Y.) **60**, 401-447 (1970).
- [51] R. Balian and C. Bloch, Ann. Phys. (N.Y.) **64**, 271-307 (1971).
- [52] R. Balian and C. Bloch, Ann. Phys. (N.Y.) **69**, 76-160 (1972).
- [53] H.P. Baltes and E.R. Hilf, *Spectra of Finite Systems*, Mannheim: B.I. Wissenschaftsverlag (1976).
- [54] M. Abramowitz and I.A. Stegun, *Handbook of Mathematical Functions*, Dover, New York (1965).

- [55] B. Eckhardt, *Phys. Rep.* **163**, 205-297 (1988).
- [56] Y.G. Sinai, *Introduction to Ergodic Theory*, Princeton University Press, (1976).
- [57] J.H. Hannay and A.M. Ozorio de Almeida, *J. Phys. A* **17**, 3429-3440 (1984).
- [58] F.J Dyson and M.L. Mehta, *J. Math. Phys.* **4**, 701-712 (1963).
- [59] M.V. Berry, *Proc. R. Soc. Lond.* **A400**, 229-251 (1985).
- [60] H. Frisk and R. Arvieu, *J. Phys. A* **22**, 1765-1778 (1989).
- [61] G. Bennetin and J.M. Strelcyn, *Phys. Rev. A* **17**, 773 (1978).
- [62] D.R. Inglis, *Phys. Rev.* **96**, 1059-1065 (1954).
- [63] D. Delande, in *Quantum Mechanics and Chaos, Les Houches Summer School Lectures LII*, to be published by North-Holland (1990).
- [64] W.H. Press, B.P. Flannery, S.A. Teukolsky and W.T. Vetterling, *Numerical Recipes*, Cambridge University Press (1986).
- [65] S. Kotz, N.L. Johnson and C.B. Read (eds.), *Encyclopedia of Statistical Sciences Vol. 2*, 451-454, New York: Wiley (1982).
- [66] M.V. Berry and M. Robnik, *J. Phys. A* **17**, 2413-2421 (1984).
- [67] O. Bohigas, S. Tomsovic and D. Ullmo, *Classical Transport Effects on Chaotic Levels*, Institut de Physique Nucléaire preprint (Orsay, France), (July 1989).
- [68] M.V. Berry, *Proc. R. Soc. Lond.* **A413**, 183-198 (1987).
- [69] E. Heller, in *Quantum Mechanics and Chaos, Les Houches Summer School Lectures LII*, to be published by North-Holland (1990).
- [70] R.P. Feynman, *Phys. Rev.* **56**, 340 (1939).
- [71] R.C. Johnson, *personal communication.* (1989).
- [72] J. Ford, in *The New Physics*, ed., P.C.W. Davies, Cambridge University Press, 348-372 (1989).

- [73] A. Shudo, *Phys. Rev. Lett.* **63**, 1897-1901 (1989).
- [74] A. Peres and L.S. Schulman, *J. Phys. A* **21**, 3893-3901 (1988).
- [75] M.V. Berry, in *Quantum Mechanics and Chaos, Les Houches Summer School Lectures LI*, to be published by North-Holland (1990).
- [76] J. Écalle, *Les Fonctions Résurgentes* (Vol. 1 to 3), Publ. Math. Université de Paris-Sud (1981).

